SHRP-ID/UFR-91-518

A Study of Road Damage Due to Dynamic Wheel Loads Using a Load Measuring Mat

David Cebon
Department of Engineering
Cambridge University
Cambridge, United Kingdom

Christopher B. Winkler
Transportation Research Institute
University of Michigan
Ann Arbor, Michigan

Strategic Highway Research Program
National Research Council
Washington, D.C. 1991

SHRP-ID/UFR-91-518
Contract ID-015
Product Number 4002

Program Manager: *K. Thirumalai*
Program Area Secretary: *Willa Owens*

May 1991
Reprinted November 1993

key words:
articulated vehicle
load sensor
road load
weigh-in-motion
wheel load

Strategic Highway Research Program
National Research Council
2101 Constitution Avenue N.W.
Washington, DC 20418

(202) 334-3774

The publication of this report does not necessarily indicate approval or endorsement by the National Academy of Sciences, the United States Government, or the American Association of State Highway and Transportation Officials or its member states of the findings, opinions, conclusions, or recommendations either inferred or specifically expressed herein.

50/NAP/1193

Acknowledgments

The research described herein was supported by the Strategic Highway Research Program (SHRP). SHRP is a unit of the National Research Council that was authorized by section 128 of the Surface Transportation and Uniform Relocation Assistance Act of 1987.

The authors would like to acknowledge the contributions of the following people: Michael Dalgleish and David Fine of Golden River Ltd.; David Cole of the Cambridge University Engineering Department; David Harrold of the Navistar Technical Center; and John Koch, Mike Campbell, and Tom Gillespie of the University of Michigan Transportation Research Institute.

Contents

List of Figures

List of Tables

Abstract

A wheel load measuring mat of total length 38 m, incorporating 96 capacitative strip Weigh-in-Motion (WIM) sensors was installed on a test track in the USA. A total of 612 test runs was performed on seven different articulated heavy vehicles, for a range of speeds between 8 km/h and 85 km/h. The wheel force data was analysed to investigate the performance of the individual sensors and the design and performance of WIM arrays with up to six sensors.

The strip sensors were found to be very reliable and to measure the dynamic wheel loads with an accuracy of better than 4 % RMS.

A theory was developed for the design of multiple-sensor WIM systems and the experimental results were found to agree closely with the theoretical predictions.

It is concluded that a good design for multiple-sensor WIM systems is to use 3 sensors, spaced evenly along the road. The sensors should be spaced according to a simple formula which depends only on the average traffic speed. The expected static axle load estimation errors for such a system are likely to be 30% to 50% of the errors of a single-sensor WIM system.

Executive Summary

Within the highway engineering community, there is considerable interest in the problem of measuring the static axle loads of heavy vehicles as they drive at highway speeds over a measurement system. 'Weigh-in-Motion' (WIM) systems have been developed during the last twenty or so years for this purpose. WIM systems are used widely for traffic data collection and there exists the possibility that they could be used in future for enforcement of static axle load regulations.

A WIM sensor measures the instantaneous dynamic force generated by the measured axle. This force can be considerably different to the static axle load which would be measured on a conventional static weighbridge (typically ± 20% to ± 50%). Thus the accuracy of a single-sensor WIM system is limited fundamentally by the dynamics of the vehicles being measured. The advent of low cost WIM sensors provides the possibility of using 2 or more sensors along the road in order to compensate for the effects of dynamic forces in the determination of static loads. The main objective of the work described in this interim report is to investigate, theoretically and experimentally, the design and performance of multiple-sensor WIM arrays which are intended to measure the static axle loads of vehicles travelling at highway speeds.

The 'load measuring mat' used in this project was developed by the Principal Investigator and his co-workers at Cambridge University in the UK in conjunction with Golden River UK Ltd. It incorporated novel capacitative strip sensors which are inexpensive, reliable and potentially more accurate than other existing low-cost WIM sensors. The load measuring mat was 1.2 m (4') wide, 13 mm (0.5") thick and contained 96 strip WIM transducers, mounted transverse to the wheel path. The total length of the mat was 38.4 m (128').

Seven different articulated heavy vehicles were tested on the mat at a variety of speeds between 8 km/h and 85 km/h and a total of 612 test runs was performed. The sensors performed very reliably and only 2.5% of the 374 400 individual WIM sensor measurements were lost. Of this, 1% was due to a single sensor which failed to function throughout. The individual sensors were found to measure instantaneous dynamic wheel loads with an accuracy of better than 4% RMS.

A theory was developed for the design of evenly-spaced, multiple-sensor WIM arrays. The theory yielded a simple design formula, by which the optimum sensor spacing can be calculated, providing the average traffic speed is known. The theory was found to agree quite closely with the experimental results. Both theory and experiment indicated that a very good WIM array design is to use 3 sensors, evenly spaced along the wheel path. Such a system is accurate for a wide range of vehicle types and speeds. The RMS static load estimation error of a 3-sensor system is likely to be only 30% - 50% of the RMS error of a single sensor WIM system. In the near future it should be possible to measure routinely the static axle loads of vehicles travelling at highway speeds with RMS errors of approximately 5-8%. This is a considerable improvement over 12% to 20% for existing single-sensor WIM systems.

SHRP/IDEA Project 15 was a collaborative project, funded jointly by six organisations: SHRP, Golden River (UK) Ltd, Michigan DOT, University of Michigan, Navistar Technical Center and Cambridge University, UK.

The mat was supplied by Golden River Ltd. and tested on the Navistar test track in Fort Wayne, Indiana during September and October 1989.

1

Introduction

Within the highway engineering community, there is considerable interest in the problem of measuring the static axle loads of heavy vehicles as they drive at highway speeds over a measurement system. 'Weigh-in-Motion' (WIM) systems have been developed during the last twenty or so years for this purpose. WIM systems are used widely for traffic data collection and there exists the possibility that they could be used in future for enforcement of static axle load regulations.

Existing WIM systems use a variety of force sensor technologies such as plates supported by load cells [1,2][1] capacitative pads [3], and piezo-electric cables [4,5]. Until recently, commercial WIM systems have usually incorporated a single wheel force transducer in each traffic lane. The transducer may be portable (stuck to the road surface), or permanent (buried slightly below the surface).

A recent advance in WIM technology is the development of a narrow capacitative strip transducer (known as a 'WIMstrip') by the Principal Investigator and his co-workers at Cambridge University Engineering Department (UK) in conjunction with Golden River Ltd, (UK) [6,7]. Development work began in January 1987. Capacitative strips are relatively inexpensive, reliable and potentially more accurate than other existing low cost WIM sensors.

The load measuring mat used in this project is a thin polymer 'carpet' of 1.2 m (4') width, 38.4 m (128') length, and 13 mm (0.5") thickness, containing a capacitative strip transducer every 0.4 m (16") along the wheel path. The mat is attached to a road surface and it measures the wheel forces of heavy vehicles that are driven over.[2]

---

[1] Numbers in parenthesis [ ] denote references listed in Section 7.

[2] For permanent WIM installations the sensors can be mounted in epoxy resin in slots cut across the road surface.

A prototype mat of length 10 m was installed on the test track of the Transport and Road Research Laboratory (TRRL) during 1988. Preliminary test results for the prototype mat are published in [6-8]. The 96 sensor mat installation for the SHRP/IDEA project was the first use of the load measuring mat technology for a major research project.

SHRP/IDEA Project 15 was a collaborative project, funded jointly by six organisations: SHRP, Golden River (UK) Ltd, Michigan DOT, University of Michigan, Navistar Technical Center and Cambridge University, UK.

The mat was supplied by Golden River and tested on the Navistar test track in Fort Wayne, Indiana during September and October 1989.

The project has three main objectives:

(i) To test the performance and accuracy of the load measuring mat for measuring the dynamic wheel loads generated by heavy commercial vehicles and to assess the suitability and accuracy of the Golden River WIMstrip transducers for Weigh-in-Motion.

(ii) To investigate the design of multiple-sensor Weigh-in-Motion systems for accurate determination of static loads from dynamic loads measured at highway speeds.

(iii) To investigate the road damaging potential of the dynamic wheel loads generated by a number of representative US vehicles.

This interim report describes the experimental programme and most of the work performed under objectives (i) and (ii). This is the work of interest to those concerned with WIM technology. The remaining data analysis for objective (iii) is currently in progress and will be described in the final report.

2

Description of Experimental Programme

Load Measuring Mat

Hardware Description

The load measuring mat utilised capacitative strip 'WIMstrip' wheel force sensors with approximate cross section 9 mm x 30 mm (0.35" x 1.2") and length 1.2 m (4'). The sensors were encapsulated in stiff polyurethane tiles of dimensions 1.2 m x 1.2 m x 13 mm thick (4' x 4' x 0.5"), with three sensors per tile, laid transverse to the wheel path at a spacing of 400 mm (16") between strips. Thirty two tiles, containing a total of 96 sensors were obtained for the project. These were mounted end-to-end on the test track, to provide an instrumented test section of length 38.4 m (128'). (Note that a load measuring mat of practically any length can be constructed simply by adding more tiles and data loggers.)

A schematic cross section of a capacitative strip sensor is shown in Fig. 2.1. Tyre contact pressure applied to the top surface of the strip causes the top 'plate' of the aluminium extrusion to deflect and hence the air gap between the top plate and the inner conductor is reduced. This results in an increase in the capacitance of the device, which, with appropriate processing, can be related directly to the contact pressure change. In order to determine the instantaneous wheel load it is necessary to integrate the transducer output with respect to time for the duration of the tyre contact. Details of the sensor design and some sources of error are discussed in [6]. This paper is also attached to this report as Appendix A.

The mat installation utilised 6 Golden River 'Marksman 600' data loggers. Each sensor was attached to a data logger by a 5 m long, 3-core cable and each data logger processed the outputs of 16 sensors, performed the integration described above and stored the results. The data loggers were connected into a network in a 'daisy-chain' configuration by RS232 serial data cables. An IBM PC/AT micro computer was connected to the network and used to upload the raw axle load information from the data loggers after each vehicle test run.

Data Logging Procedure

The 'Procomm' communications package on the microcomputer was used to issue high-level commands to the data loggers (in a special purpose language designed by Golden River) and to log the incoming data into files on the hard disk of the microcomputer.

For each 'event' detected by a data logger (ie an axle crossing a sensor), four items of information were stored in the data loggers and subsequently transmitted to the PC after each vehicle test:

(i) Sensor number
(ii) Time of the event ('time tag')
(iii) Sensor reference DC output level immediately prior to the event
(iv) Integrated sensor output for the event (proportional to the wheel force.)

A thermocouple was used to measure the surface temperature of the mat at regular intervals throughout the vehicle testing program.

Field Data Processing Software

Several 'user friendly' data handling programs were written to run on the PC:

Raw data sorting and scaling

The raw data files contained the axle load information in chronological (event) order, for each box. It was necessary to sort this information according to the axle and sensor numbers, and to convert the raw sensor outputs into axle loads in units of force. The latter function required scaling by the calibration factor of each sensor and the vehicle speed.

A program was written for the PC in Fortran 77 to perform the sorting and calibration functions on the raw data files. The sensor calibration factors were read from a file, and the vehicle speed was calculated using a linear regression on the sensor 'time-tag' data. The program generated ASCII output files in standard 'ERD' file format developed by UMTRI. This facilitated their processing with a number of standard UMTRI data handling, analysis and plotting programs.

The data sorting program was written to cope with missing and/or spurious data points from one or more sensors. The resulting code was relatively complex, but reliably trapped virtually all data errors (see section 2.1.4), thus producing sorted and scaled output files automatically.

A second program was written to sort and scale a large number of raw data files automatically using a 'directory' file containing a list of the names of the files to be processed.

Data plotting

A straightforward program was written, using an existing UMTRI graph plotting utility, to view processed data from the ERD files on the microcomputer. This enabled viewing of the data in the field almost immediately after each vehicle test run.

Automatic Field Calibration

An automatic field sensor calibration method was devised as a convenient and efficient alternative to the hydraulic calibration procedures described in Section 2.5. The method requires a vehicle with known static loads to be driven over the sensor array a number of times at low speeds, so as to minimise the dynamic loads.

A program was written to read-in any number of processed (ERD) data files associated with these tests and to calculate average calibration factors for each sensor using the static loads from one or more of the axles. The program writes out a calibration factor file.

Many other computer programs were written during the course of the project to perform various elements of the data analysis, however they will not be described here because they were not part of the field testing system.

Sensor and Data Logger Performance

The mat and data logger system was the first large scale installation of its type (apart from a 24 sensor prototype installation in the UK [6-8]) and it functioned largely as designed. Intermittent problems were experienced with a few of the sensors, which occasionally generated spurious outputs, or failed to detect an event. In addition, one sensor (number 11) failed to function correctly for most of the tests. This fault was traced to a problem in a data logger. Overall, approximately 2.5% of all axle load information was lost due to hardware problems (1% of this was due to sensor 11). This level of data loss was considered to be acceptable for the requirements of the project.

Test Site

Navistar Test Track

The field tests were performed on the Navistar test track in Fort Wayne, Indianna. The oval track has 2 lanes and is 1.9 km (1.2 miles) long. Figure 2.2 shows the layout of the track and the location of the mat installation on the 4-lane straight. The 'forward' and 'reverse' arrows on the figure refer to the direction of testing (see later). The location of the mat was chosen to enable vehicle tests at speeds up to 85 km/h (53 mph) in both directions without unduly disrupting normal use of the track by Navistar personnel.

Mat Installation

Previous work [8] had shown the need to attach the mat tiles to the road surface as firmly as possible, so as to minimise movement of the sensors. The polyurethane mat tiles were attached to the test track with by the following procedure:

(i) The asphalt surface was swept of stones, dust and loose debris.

(ii) A roll of 1.5 m wide, 1.6 mm thick (52" x 1/16") double-sided adhesive PVC foam sheet (by Gaska Tape Inc, Elkhart, IN) was attached to the track surface in the outer wheel path.

(iii) The mat tiles were placed end-to-end along the sheet. In addition to the adhesive sheet, each tile was screwed to the asphalt surface using twelve 75 mm long (3") masonry screws. The screws were located by machined washers which fitted into 'counterbored' holes cast in the surface of the tiles.

(iv) A total length of 19.5 m (64') of 1.2 m wide, 13 mm thick (4' x 1/2") timber sheet was screwed to the test track at each end of the mat installation. This ensured that the test vehicles were nominally horizontal when passing over the mat sensors, and that transient vibration due to the 13 mm step was reduced slightly.

It was decided not to use an additional timber sheet in the second wheel path because of the relatively large transverse slope of the test track.

(v) It was thought that there was a possibility that the sensor cables could be sheared-off at the edge of the mat if an axle ran sufficiently off-track. This danger was alleviated by screwing 13 mm thick timber strips to the road surface, either side of every cable.

Test Vehicles

Three 6x4 tractors and three tandem axle semi-trailers were provided by Navistar for testing on the mat. The vehicles were arranged into six different tractor/semi-trailer combinations. The combinations were coded S1 to S6 and are described in Appendix B. Two of the tractors had tandem '4-spring' suspensions and the third had a 'trailing-arm' tandem air suspension with hydraulic dampers. Two of the trailers had 4-spring tandem suspensions, while the third had a pivoted spring 'single-point' tandem suspension. The vehicle combinations were selected to be relatively representative of the US truck fleet.

Each vehicle was weighed on a static whole-vehicle weighbridge of length approximately 15 m immediately prior to, or after the testing. The weighing procedure involved driving the vehicle on and then off the weighbridge, one axle at a time, and recording the weight of each axle combination. This enabled two estimates of the static load of each axle to be obtained as well as the gross weight of the vehicle. The individual static axle loads are provided in Appendix B.

A series of tests was also performed using the UMTRI Mobile Tyre Testing vehicle which has an instrumented axle, capable of measuring the vertical dynamic load between the tyre and road. The data from these tests has not been analysed yet but will be included in the final report.

Matrix of Vehicle Tests

Each articulated vehicle combination was driven over the mat at nominal speeds of 5, 10, 20, 30, 40 and 50 mph (8, 16, 32, 48, 64, 80 km/h) in both the 'forward' and 'reverse' directions over the mat. In a few cases, a speed of 85 km/h (53 mph) was achieved. At least six repetitions were performed at each test condition and the matrix of tests is summarised in Appendix C. A total of 460 test runs was performed on articulated vehicles during four days of testing.

Sensor Calibration

Three methods were used to determine calibration factors for the sensors:

Laboratory calibration of bare sensors

The bare sensors were calibrated by Golden River Personnel in the UK prior to encapsulation in the polyurethane tiles, using a hydraulic calibrator, developed in Cambridge. A calibration was performed at three locations along each sensor and the mean and coefficient of variation (standard deviation/mean) of the three measurements were recorded. The coefficient of variation is a measure of the uniformity of the sensor and should ideally be zero.

Laboratory calibration of encapsulated sensors

A special purpose 'in-situ' static calibrator was manufactured at UMTRI for the project to a design developed in Cambridge. This device consisted of an aluminium alloy plate which supported a flexible polyurethane diaphragm. The plate was placed on the surface of the mat. A hydraulic hand pump was connected to the plate by a flexible hose and was used to pressurise the cavity behind the diaphragm with oil. This pressed a 185 mm x 40 mm (7.3" x 1.6") area of the diaphragm against the surface of a mat tile, above a sensor with a uniform contact pressure. It was necessary to react the resultant upward thrust by adding a dead load (weights or the wheel of a truck) to the top of the plate (see Fig. 2, Appendix A). The aluminium plate bridged the sensor so that the dead load was reacted approximately 40 mm (1.6") either side of the sensor. This ensured that the sensor output was not affected by the size or exact position of the weights, but only by the contact pressure under the diaphragm.

Each of the 96 sensors was calibrated in the laboratory at the University of Michigan prior to the field tests. Calibration factors were determined at three locations along each sensor strip to assess the uniformity.

The steps involved in each calibration measurement were:

(i) lining-up the calibrator plate above a sensor, (ii) placing a load frame with weights on the plate and (iii) pumping-up and releasing the hydraulic pressure. The oil pressure and sensor output were recorded at no-load, half-load and full load (1.5 MPa). This was performed 3 times, and a linear regression used to determine the calibration factor for each of the 3 calibrator positions along the sensor. The mean and coefficient of variation of the 3 measurements was calculated for each sensor.

Field Calibration using vehicle loads

The automatic field calibration procedure described in section 2.1.3 (iii) was used to generate a file of average sensor calibration factors. The *steering axle* measurements on the six articulated vehicles were used. All of the 5 mph (nominal) test results were averaged together. The static wheel loads were assumed to be half of the axle loads listed in Appendix B, irrespective of the vehicle speed or direction of travel.

Histograms of the mean calibration factors for the three calibration methods are plotted in Figs. 2.3a,b,c. It is apparent from the figures that the 'in-situ' calibration method (Fig. 2.3b) produced a significantly wider spread of data than the other two methods. It also produced a completely different mean calibration factor of 435.5 MPa, compared with 418.2 MPa for the laboratory calibration of the bare sensors and 415.0 MPa for the field calibration (Figs. 2.3 a,c).

This inconsistency of the 'in-situ' calibration method is also apparent from Figs. 2.4a,b which shows the distribution of the Coefficient of Variation (COV) of the calibration factors measured at the three locations along each sensor (this should ideally be zero for 'perfectly uniform' sensors). Figure 2.4a shows the result of calibrations on bare sensors and Fig. 2.4b shows the results obtained with the 'in-situ' calibrator on the encapsulated sensors. The average COV of the bare sensors is 3.2% but for the encapsulated sensors the average COV is 4.5%.

The only possible explanation for this behaviour is that the 'in-situ' calibration factors are unreliable. (The polyurethane tiles were cast to close tolerances and the variation in sensitivity cannot be explained by polyurethane thickness or stiffness variations.) It is not completely clear why this occurred, since the 'in-situ' calibration method had proved accurate and reliable in previous tests [8]. However it is known that the polyurethane diaphragm used in the 'in-situ' calibrator was slightly thicker than specified in the design. It is likely that this may have resulted in a small additional load being transferred to the sensor, depending on the exact position of the calibrator, hence causing calibration errors.

Because of these problems, the calibration factors measured in the field (shown in Fig. 2.3c) were used in the remainder of the analysis in this report.

Time constraints prevented measurement of calibration factors with the hydraulic calibrator after the mat sections were installed on the test track.

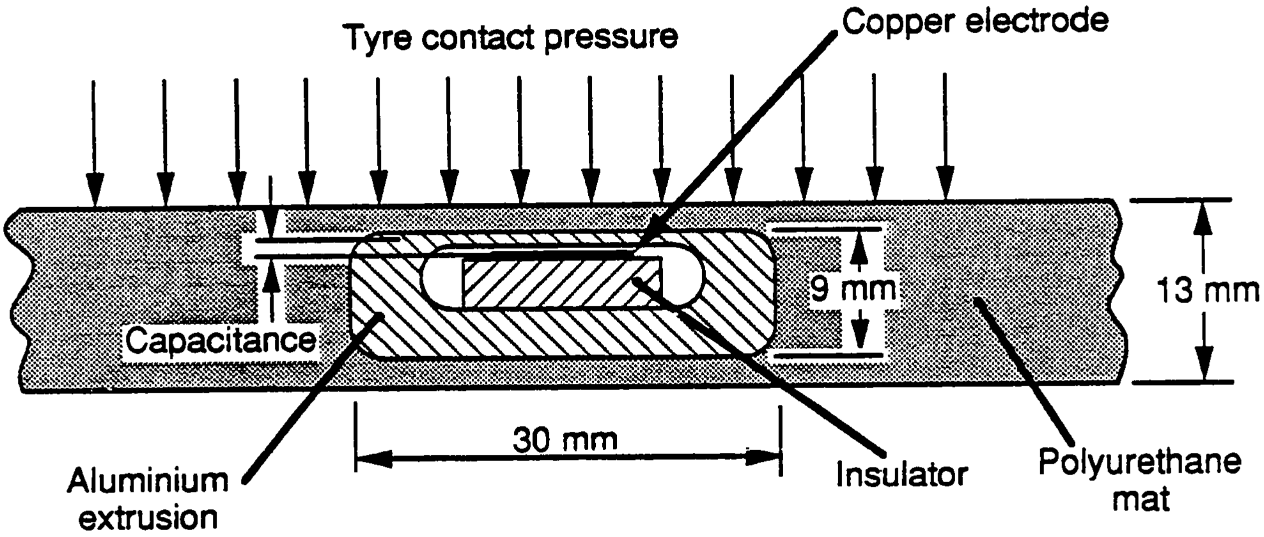

Fig.2.1 Schematic cross-section of a capacitative strip wheel force sensor incapsulated in a polyurethane tile.

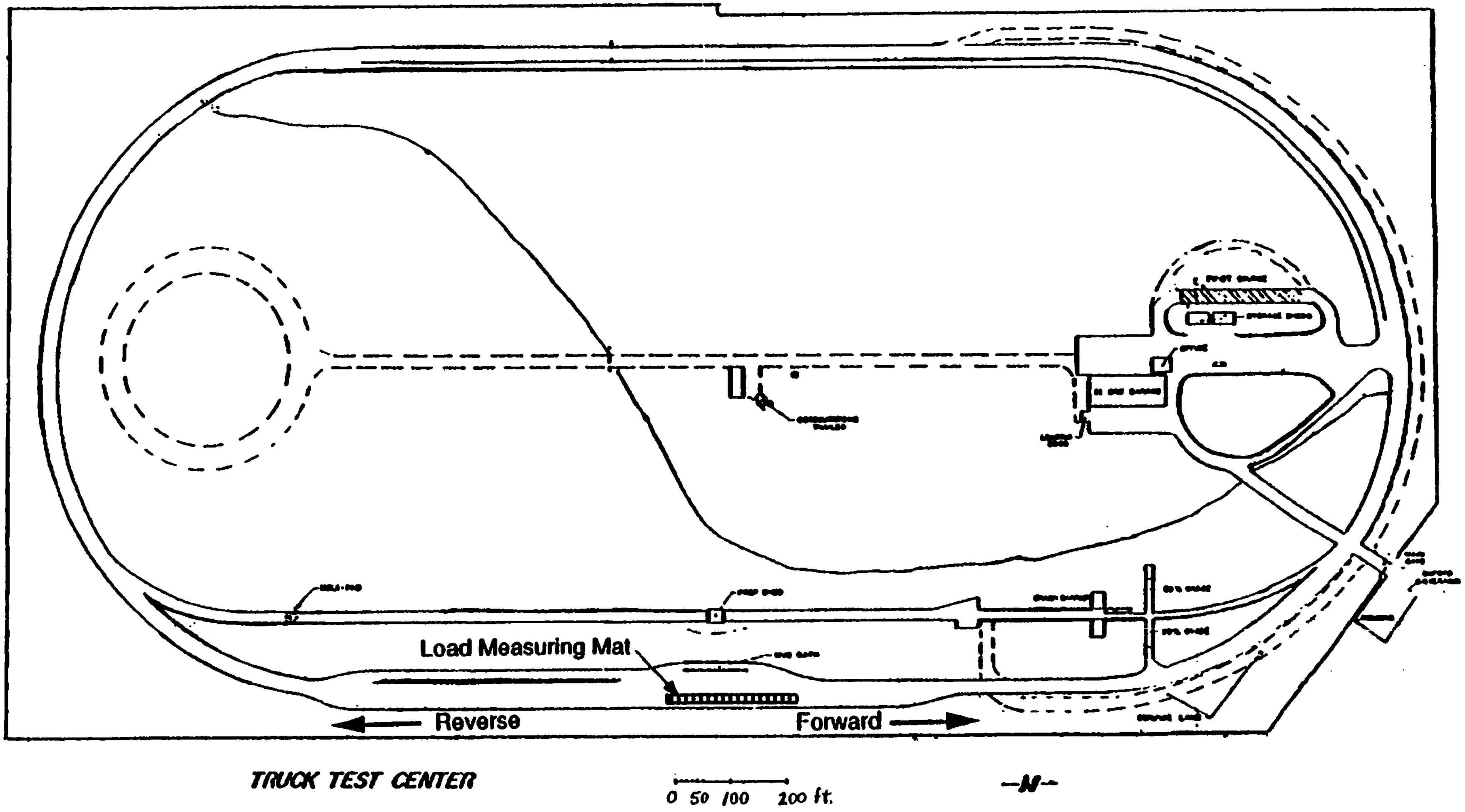

Fig. 2.2 Plan of the Navistar Test Track, showing the site of the mat installation.

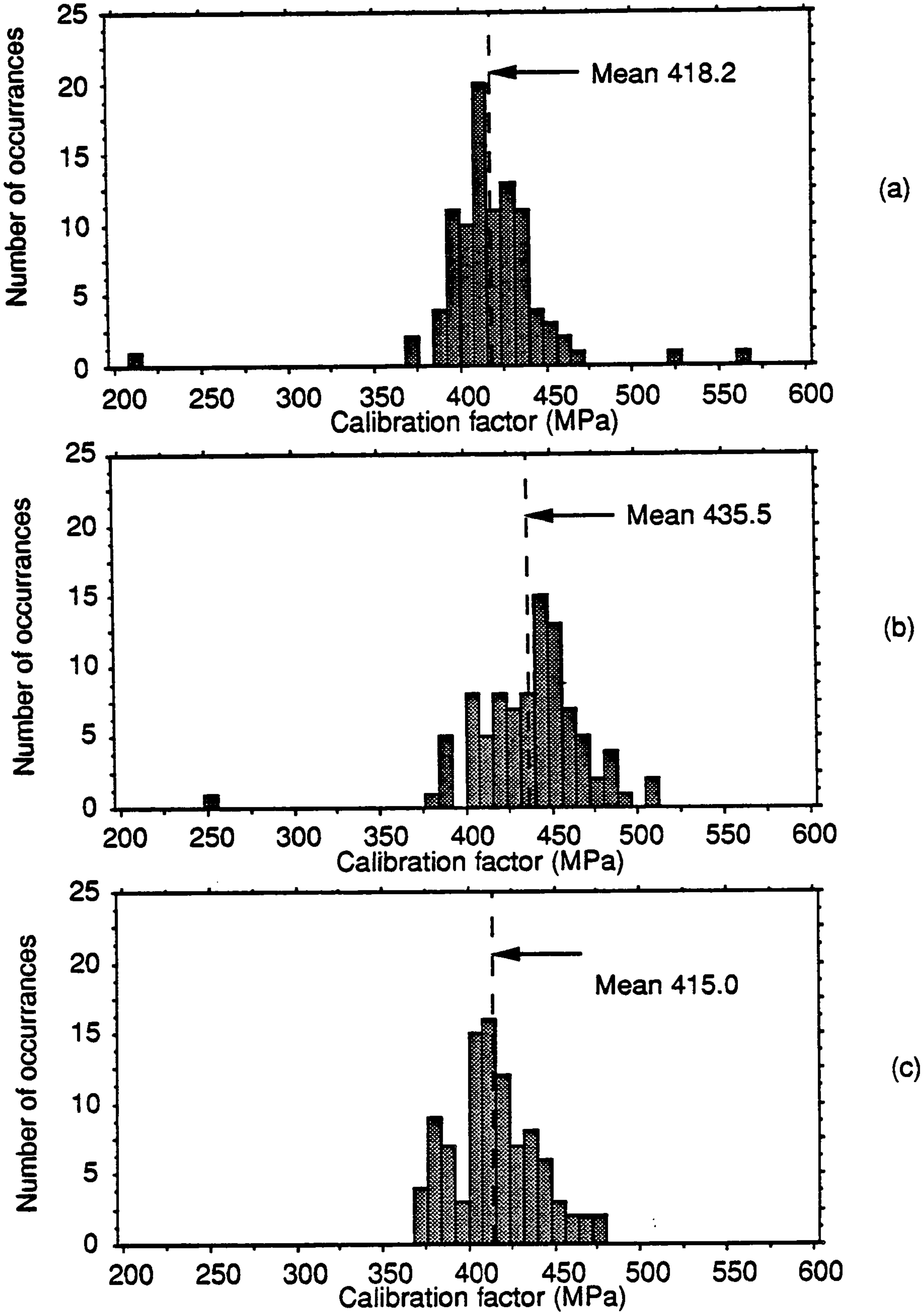

Fig. 2.3 Histograms of sensor calibration factors
(a) Bare sensor calibrator (b) 'In-situ' calibrator
(c) Field calibration with steer axles of 6 vehicles

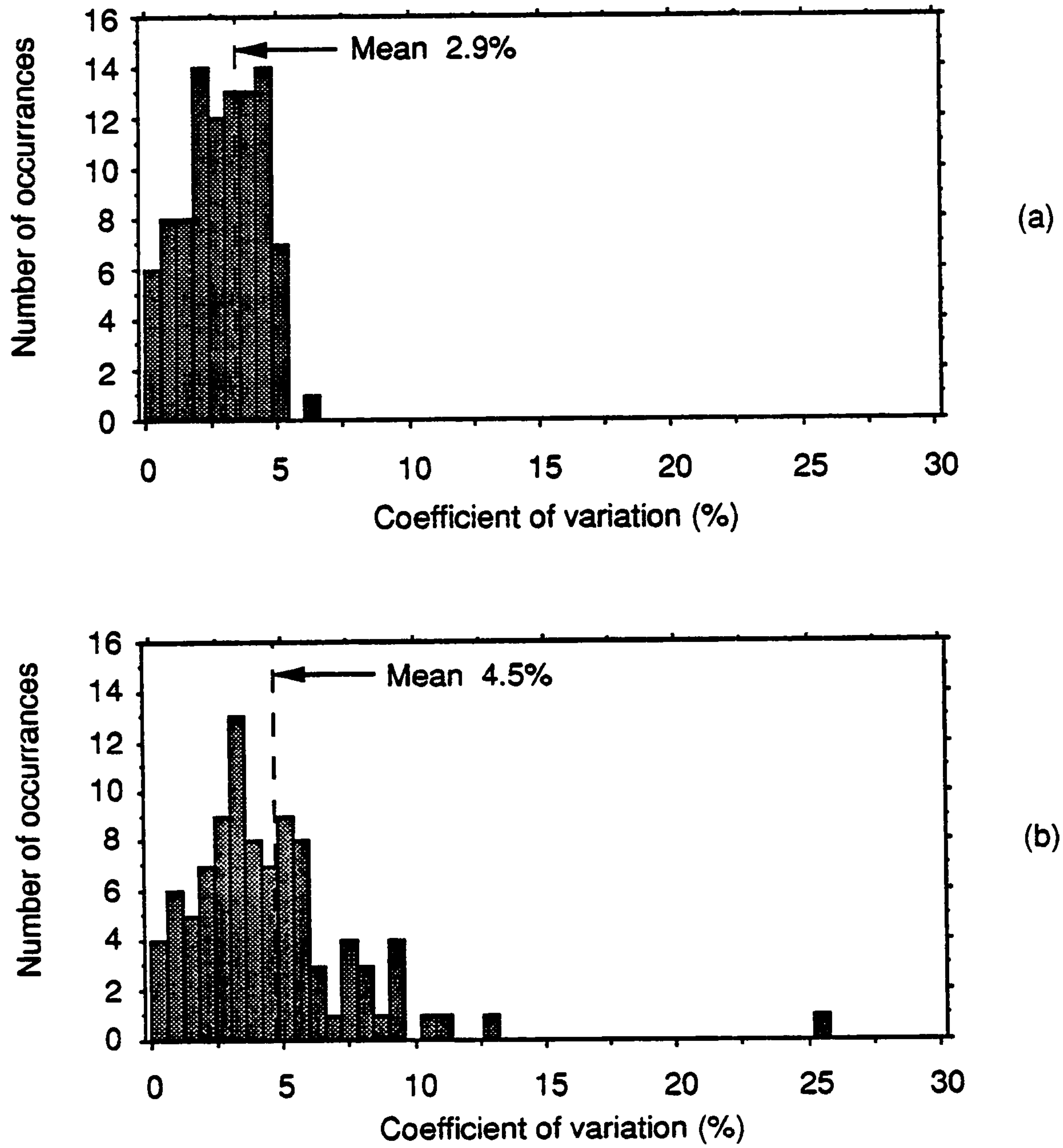

Fig. 2.4 Histograms of sensor calibration factor coefficients of variation
(a) Bare sensor calibrator (b) 'In-situ' calibrator

3

Analysis of Average Wheel Forces

Before examining the accuracy of WIM systems using a limited number of sensors, it will be useful to assess some possible sources of systematic error by calculating the average of the loads measured by all of the sensors in the mat. Under most conditions, it is expected that the average of the 96 sensors should be a reasonable estimate of the true static load, with dynamic components largely averaged out.

It should be noted, however, that the average wheel forces generated by trucks at highway speeds are not necessarily equal to the loads measured on a static weigh bridge. Even at steady speed, fore-aft static weight transfer can occur due to the driving torques and aerodynamic forces. Lateral weight transfer due to uneven load distribution or road surface camber and cross-fall can also cause significant differences in the loads measured on the two ends of a particular axle. It is also possible for static weighbridges to yield inaccurate results, particularly for individual axle measurements [2].

Effect of Temperature

The capacitative strip sensors were designed to be insensitive to ambient temperature variations. Previous unpublished measurements on 'bare' (un-encapsulated) sensors confirmed negligible temperature sensitivity over a reasonable temperature range. However there was still some uncertainty as to whether the thermal properties of the polyurethane encapsulating material would cause a systematic sensitivity variation with temperature.

This question was investigated by analysing the steering axle data from each of the six articulated vehicle combinations for the lowest speed test runs, at nominally 8 km/h (5 mph). (The low speed steering axle data is expected to contain the least variation due to dynamic axle loads). The test runs in the 'Forward' (anticlockwise) and 'Reverse' (clockwise) directions around the test track were analysed separately: in most cases, these two sets of tests were performed several hours apart, with widely different mat surface temperatures.

The mean and standard deviation of all of the sensor outputs were calculated for the steering axle for each of the twelve groups of low speed tests (6 vehicles, forward and reverse directions: i.e. runs S1R0501-S1R0520, S1F0501-06, S2R0501-06, ...S6F0501-07 in Appendix C). These results are all plotted in Fig. 3.1 as percentage errors from the static loads that were measured on the weighbridge (listed in Appendix B). The error bars show one coefficient of variation (standard deviation/mean) either side of the mean load. The standard deviation is generally approximately 4-6% of the static load, and can be attributed to dynamic wheel loads and to random noise in the sensor measurements (see later).

Ten of the twelve data points have mean loads within 4% of the static load and there appears to be little, if any systematic temperature dependence. The two outlying points correspond to vehicles S1 and S4 in the 'Reverse' direction. It will be seen in section 3.4 that these larger errors were mainly caused by inaccuracies in the static loads measured on the weighbridge.

Effect of Speed

There are three likely causes of systematic speed dependence in static load measurements using conventional WIM systems.

(i) *Dynamic loads:* The approach to the WIM site (or the site itself) may be abnormally rough and induce dynamic loads which are dependent on the speed of the vehicle. This is particularly likely if the WIM sensor is mounted on top of the road surface and causes a step change in road surface height.

(ii) *Weight transfer:* The average wheel loads of a fast moving vehicle may differ from the static loads measured on a static weigh scale, because of fore-aft weight transfer due to driving torques and aerodynamic forces.

(iii) *Sensor errors:* The dynamic response of the sensor and instrumentation may not be sufficiently good to maintain accuracy as the vehicle speed increases and the duration of the measured load pulse decreases.

In the following analysis, the effects of dynamic loads (i) are eliminated by examining the *average* forces measured for each axle by many sensors. The dynamic load contribution is expected to average out. Thus any speed dependence in the following must be due to (ii) or (iii).

Similar data processing to that described in the previous section was performed for each of the six nominal vehicle speeds and six vehicle combinations (S1 to S6) in the 'Forward' and 'Reverse' directions. This involved processing 460 data files in the 72 groups, listed in Appendix C. The mean and standard deviation of each axle load was averaged over each group of files, and is shown as a marker symbol with error bars on one of Figures 3.2-3.7. In these figures, the static load errors for each axle are plotted as a function of vehicle speed. The error bars indicate ± one coefficient of variation (standard deviation/mean).

If the sensors were perfectly accurate and noise free, the error bars would correspond to 1 Dynamic Load Coefficient (as a percentage) either side of the mean wheel force, since

$$\text{Dynamic Load Coefficient} = \frac{\text{RMS Dynamic load}}{\text{Static load}}.$$

Several useful observations can be made from the trends in the mean values shown in Figures 3.2 to 3.7. The lengths of the error bars will not be discussed further in this section as they relate to the dynamic loads which are the subject of Chapter 5.

(i) Overall, there seems to be little or no systematic dependence of the static load errors on vehicle speed. In some cases the average loads appear to increase slightly with speed (eg Figs. 3.2d,e), in other cases they are relatively constant (eg. Fig. 3.5b), in some cases, they appear to decrease slightly (Fig. 3.7b). and in others, they fluctuate (Fig. 3.2a).

In most cases the variation in mean level is only a few percent and significantly less than the coefficient of variation of the measurements (size of error bars). There are no particular differences in the trends observed for the steer axle or the tractor or trailer groups.

(ii) There is no evidence of fore-aft weight transfer affecting the static loads for higher speeds. This effect would be expected to cause an apparent lightening of the steer axle, and a corresponding increase in average load of the tractor drive axles. If such weight transfer did occur the effect on the trailer axles would be expected to be negligible.

(iii) As a result of (i) and (ii) it seems reasonable to conclude that the calibration of the capacitative strip transducers is not affected significantly by vehicle speed.

Effect of Direction of Travel

The single largest influence on the static load errors is direction of travel of the vehicle. Figures 3.2 d,e indicate 15-20% difference in the average loads measured on the nearside and offside ends of the trailer axles (axles 4 and 5). This is almost certainly because the trailer on vehicle S1 was loaded unevenly. This fact is confirmed by Figs. 3.3 d,e for vehicle S2, which had the same trailer as S1, but a different tractor. S2 displays a similar discrepancy between the average loads of the nearside and offside trailer wheels.

A similar effect is observed for the tractor axles (2 and 3) on vehicles S4, S5 and S6 (Figs. 3.5 b,c to 3.7 b,c). These three vehicles all had the same trailer but different tractors. It appears that uneven loading at the front of the trailer was transmitted as a moment through the fifth wheel coupling to the tractor drive axles. The difference between nearside and offside static loads is somewhat less in this case: approximately 10%.

The load distribution explanation does not seem to apply to the peculiar behaviour of the trailer axles (4 and 5) on vehicles S4, S5 and S6 (Figs. 3.5 d,e to 3.7 d,e). In these cases, axle 4 is always heavier in the 'Forward' direction than the 'Reverse' direction, and axle 5 is heavier in the

'Reverse' direction than in the 'Forward' direction. This is thought to be caused by some sort of misalignment in the trailer suspension which caused the nearside wheel on axle 4 and the offside wheel of axle 5 to carry more of the static load than the other ends of the axles. (This is analogous to a table with short legs in opposite corners). The error is approximately 5-7% of the static loads.

Effect of Weighbridge Errors

The procedure used to measure the static axle loads is described in section 2.3. The static wheel loads were assumed to be half of the corresponding static axle loads. This procedure is inherently inaccurate for weighing individual axles, particularly tandem pairs, because the weighbridge is so long (15 m), and the accuracy is critically dependent on the road surface profile at the ends of the weighbridge [2]. However, the gross vehicle weight can be determined accurately. This inaccuracy in individual axle loads explains why the average errors on the nearside and offside wheels of some axles are not equal in magnitude and opposite in sign. For example, the average loads on axle 4, vehicle S1 are approximately equal and opposite (Fig. 3.2d) indicating that the weighbridge measurement of the static axle load is approximately correct (but the loads on the nearside and offside wheels are different due to uneven loading). Conversely, on axle 5, vehicle S1, the weighbridge measurement of the static load is approximately 7-9% low. Hence the offside wheel appears to have the correct load, but the static load of the nearside wheel appears to be 18-20% high. (Recall that the *difference* between nearside and offside axles is due to the uneven load distribution - previous section).

The weighbridge errors appear to depend on the suspension system. The 4-spring trailer suspensions (all vehicles except S3) give a substantial error although not always with the same sign. This behaviour is expected from such suspensions because of the large friction forces between suspension elements which can cause substantial 'hysteresis' in the static load measurements.

Conclusions

(i) Temperature has no systematic effect on mat sensor accuracy in the range of 15 to 40 °C.

(ii) The calibration of the capacitative strip transducers in the mat is not affected by speed in the range 8 to 85 km/h.

(iii) No evidence was observed of fore-aft load transfer in the articulated vehicles due to speed.

(iv) Two of the trailers were loaded unevenly causing differences between the static loads measured on nearside and offside axles.

(v) The static weighbridge measurements were inaccurate, particularly for weighing individual axles from the tandem groups with 4-spring suspensions.

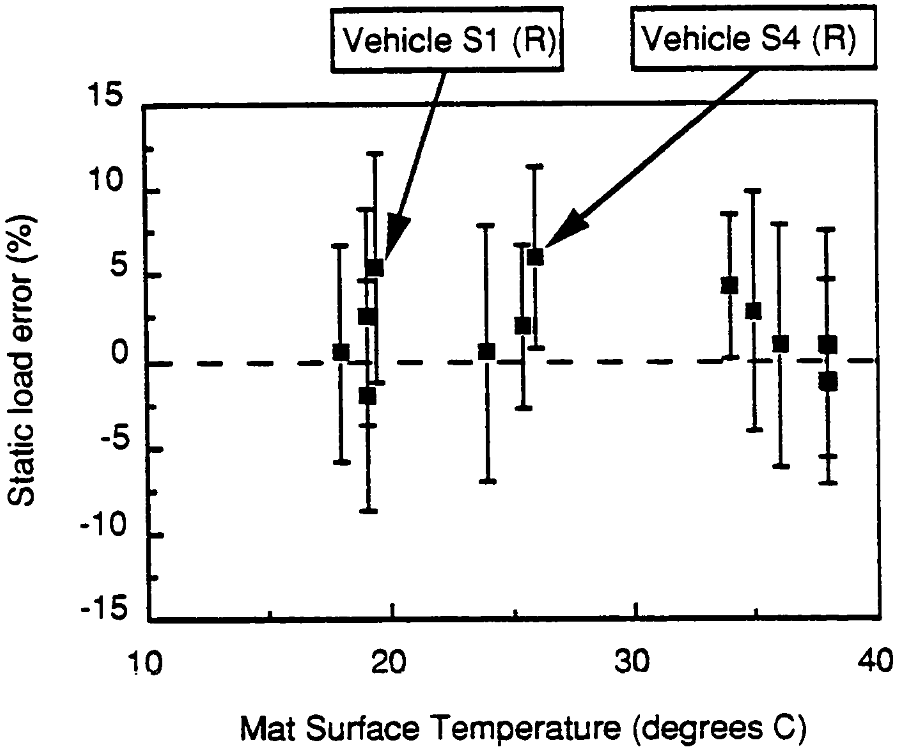

Fig 3.1 Static load errors, steering axles, Vehicles S1-S6.
The error bars indicate one standard deviation either side of the mean

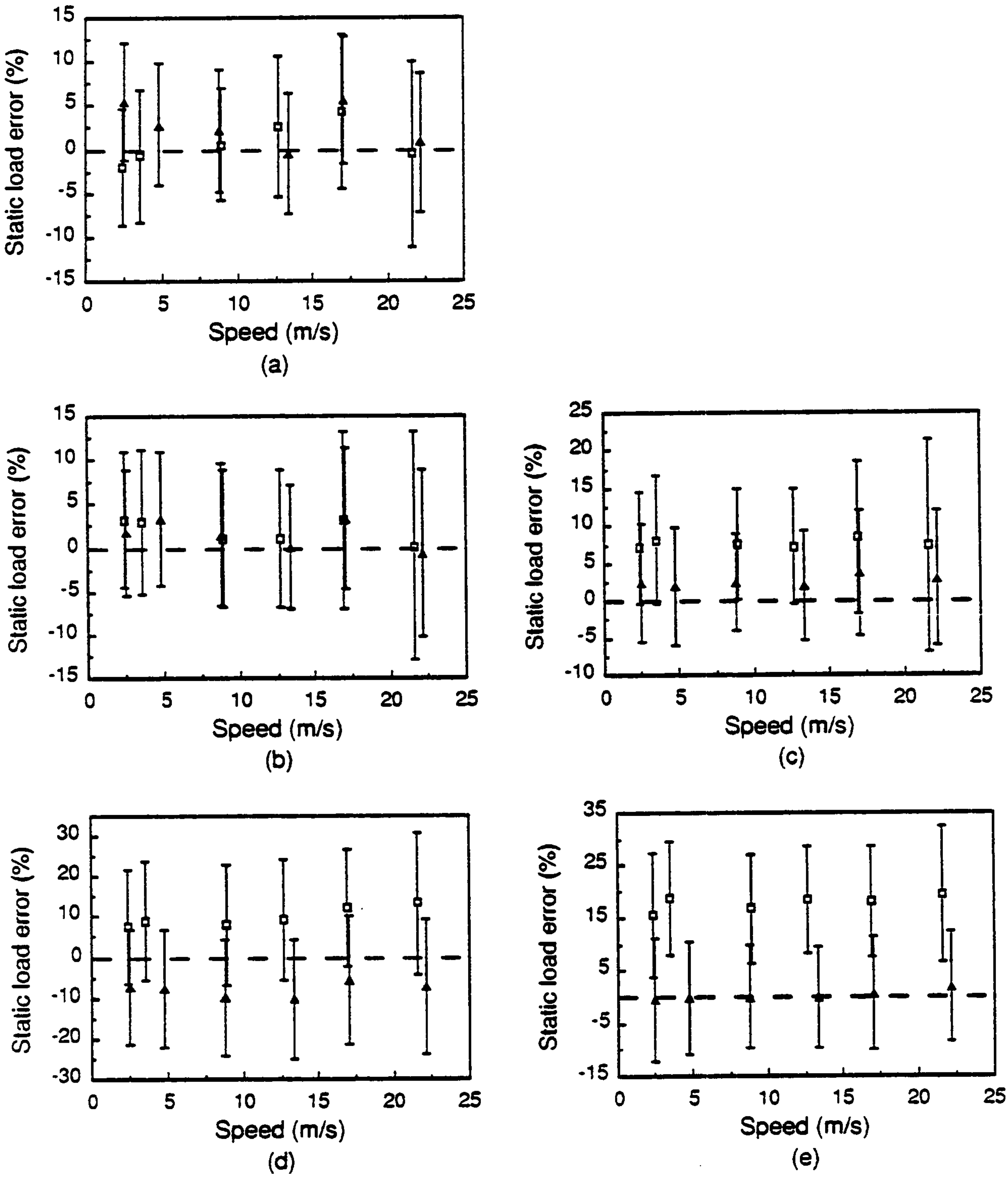

Fig. 3.2 Static load error vs speed, Vehicle S1
(a) Axle 1 (b) Axle 2 (c) Axle 3 (d) Axle 4 (e) Axle 5
Error bars indicate ± 1 standard deviation

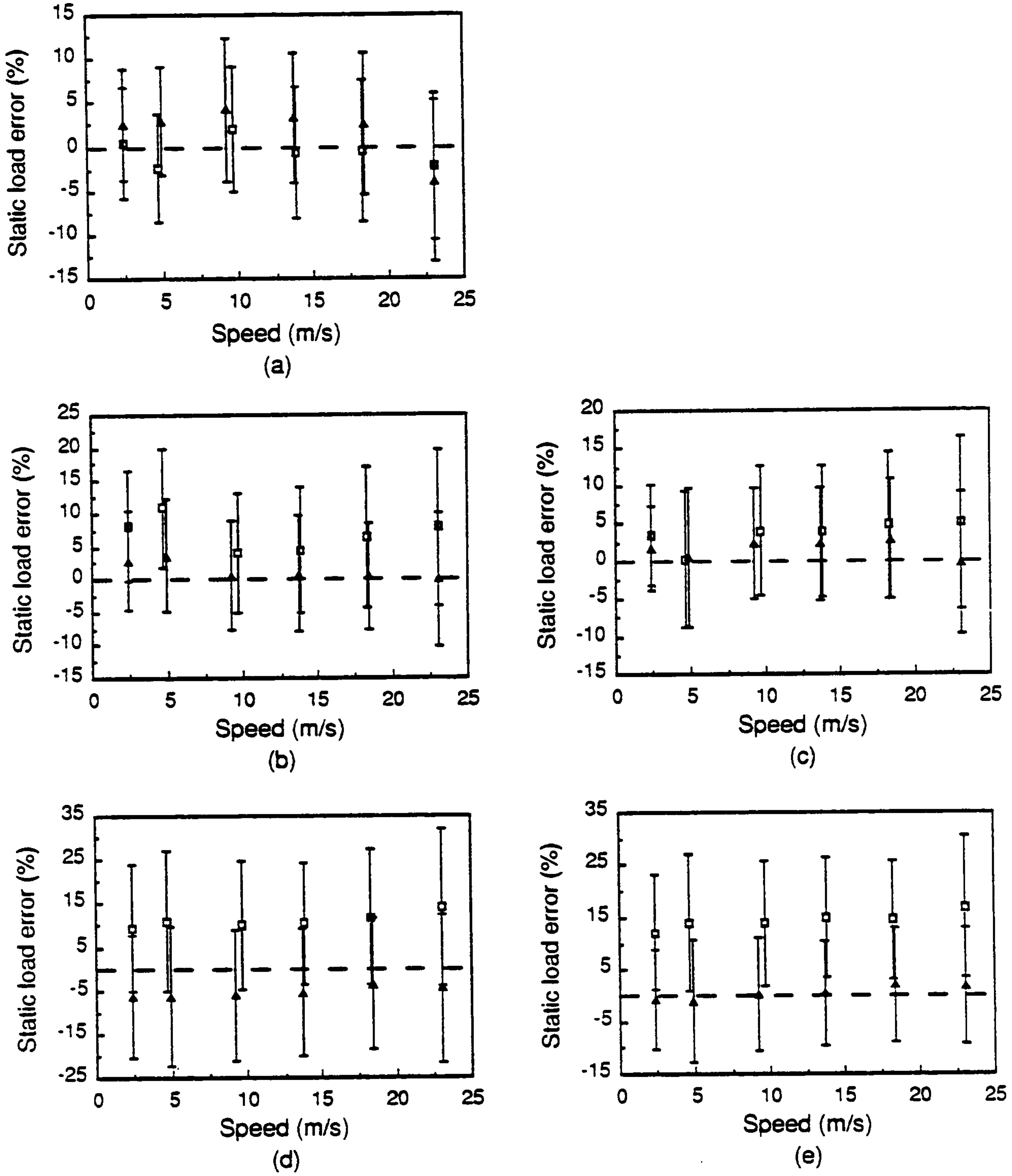

(a)

(b)

(c)

(d)

(e)

Fig. 3.3 Static load error vs speed, Vehicle S2
(a) Axle 1 (b) Axle 2 (c) Axle 3 (d) Axle 4 (e) Axle 5
Error bars indicate ± 1 standard deviation

▫ FORWARD
▲ REVERSE

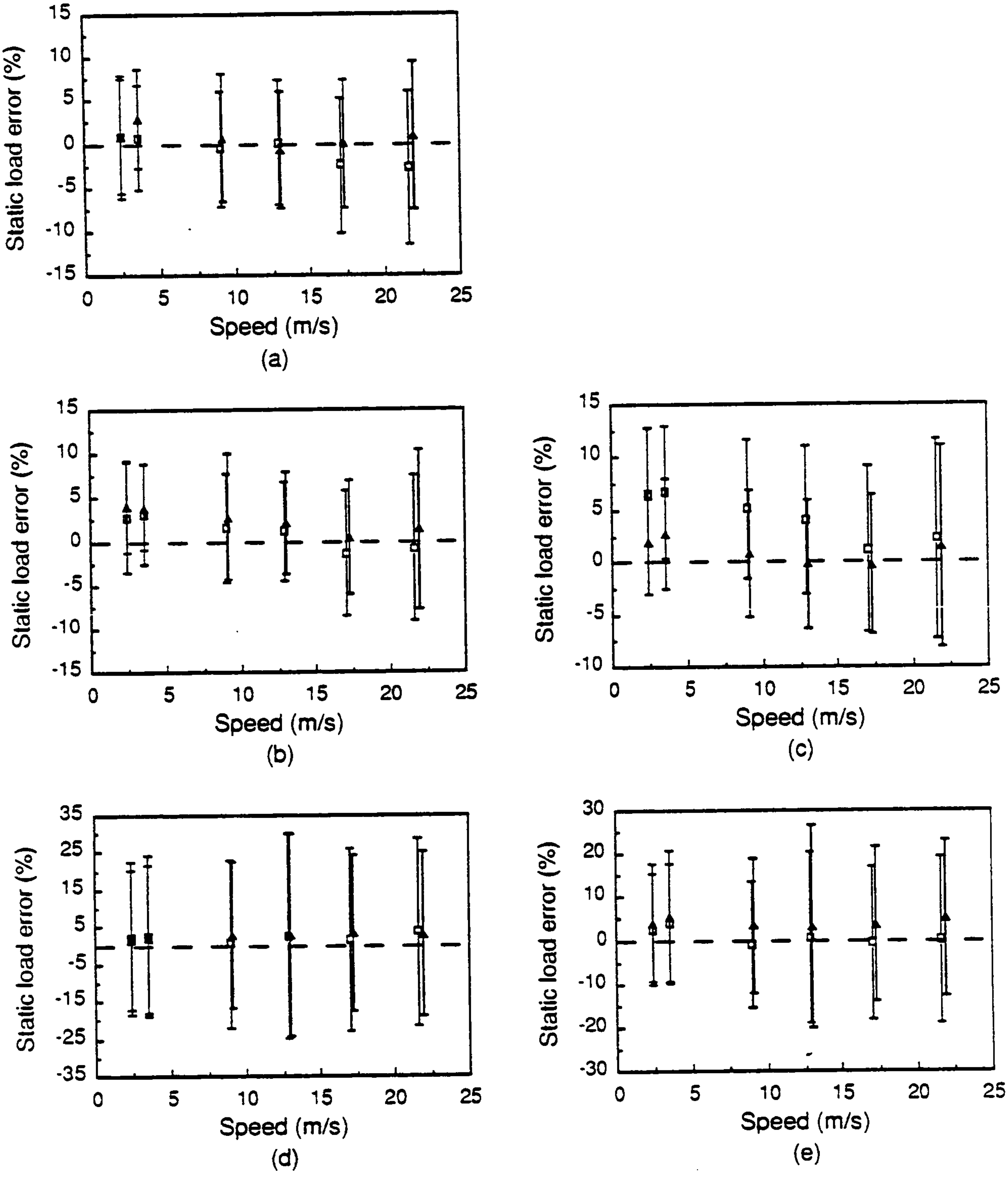

Fig. 3.4 Static load error vs speed, Vehicle S3
(a) Axle 1 (b) Axle 2 (c) Axle 3 (d) Axle 4 (e) Axle 5
Error bars indicate ± 1 standard deviation

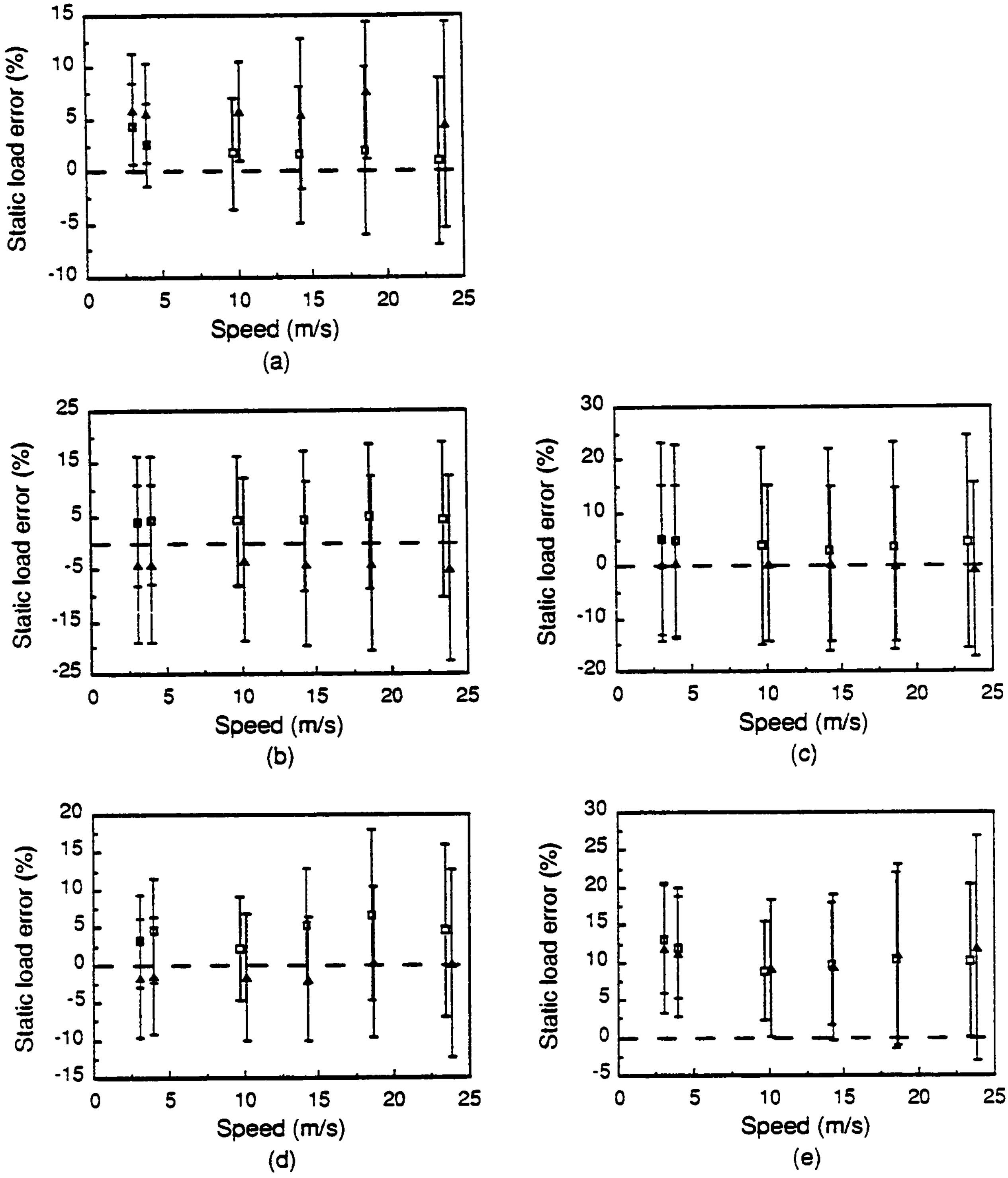

Fig. 3.5 Static load error vs speed, Vehicle S4
(a) Axle 1 (b) Axle 2 (c) Axle 3 (d) Axle 4 (e) Axle 5
Error bars indicate ± 1 standard deviation

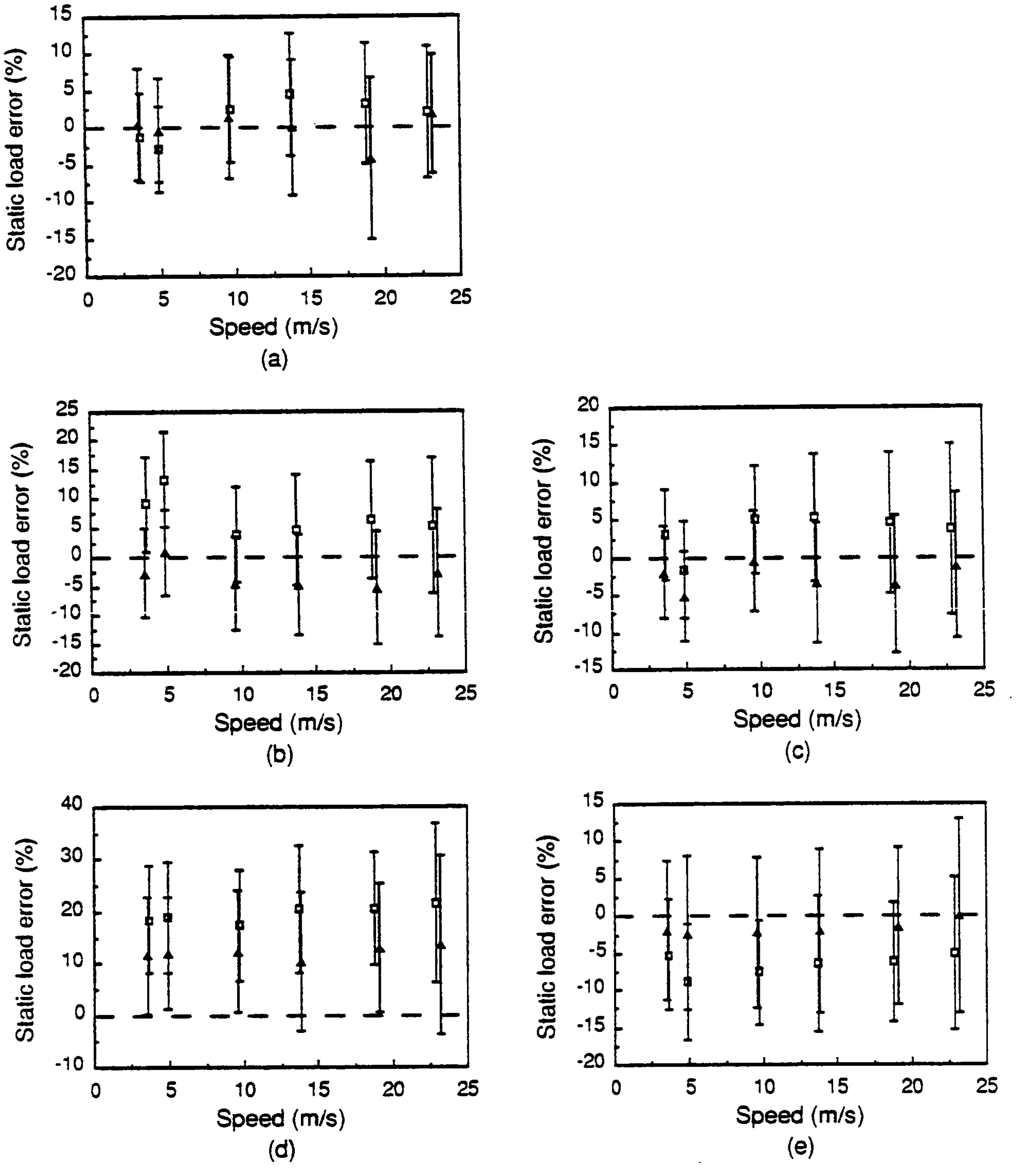

Fig. 3.6 Static load error vs speed, Vehicle S5
(a) Axle 1 (b) Axle 2 (c) Axle 3 (d) Axle 4 (e) Axle 5
Error bars indicate ± 1 standard deviation

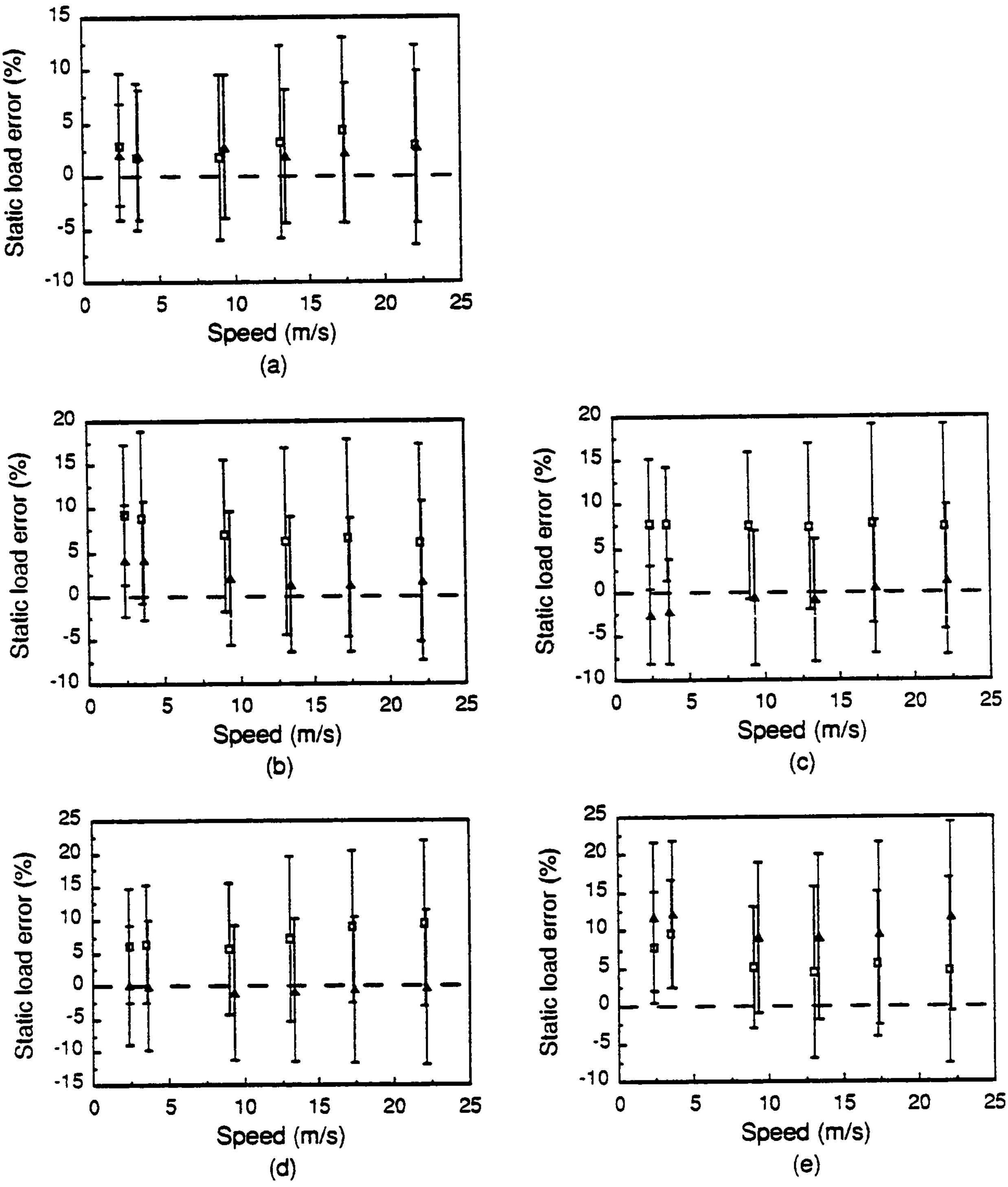

Fig. 3.7 Static load error vs speed, Vehicle S6
(a) Axle 1 (b) Axle 2 (c) Axle 3 (d) Axle 4 (e) Axle 5
Error bars indicate ± 1 standard deviation

4

Theory of Multiple-Sensor Weigh-in-Motion

Introduction

Road surface roughness excites vibration of heavy vehicles which results in dynamic tyre force fluctuations. These have typical Root Mean Square (RMS) amplitudes of 10-30% of the static wheel loads [9-12]. The dynamic tyre forces result from vehicle motion in two distinct frequency ranges:

1.5 to 4.5 Hz:	Sprung mass bounce and pitch vibration modes;
8 to 15 Hz:	Unsprung mass bounce and roll, 'load-sharing' suspension pitch modes.

At 100 km/h, these modes of vibration are excited by roughness irregularities with wavelengths of 6.2 m to 18.5 m and 1.9 m to 3.5 m respectively. Various experimental and theoretical studies [10-14] have shown that the lower frequency sprung mass modes usually dominate the dynamic tyre forces generated by heavy vehicles on highways, except for vehicles which have axle group suspensions (particularly of the walking-beam type) with poorly damped bogie pitching modes.

It is difficult to obtain accurate information on the popularity of the various suspension types, however, based on a survey of manufacturers, Morris [15] estimated the following distribution of suspensions on new heavy vehicles in the USA:

Estimated proportions of suspensions on new US heavy vehicles, from [15]

Suspension	*Tractors (%)*	*Trailers (%)*
Walking-beam	15-25	< 2
Air spring	15-20	10-15
Leaf spring	55-77	> 80
Other	2-4	Nil

From this data it may be estimated that approximately 10% of the suspensions on new articulated heavy vehicles in the USA are of the walking-beam type. This is consistent with the proportions of such suspensions observed by the Principal Investigator in Britain and several European Countries. Hence it can be stated with reasonable confidence that the majority of suspensions in current use on trucks are of the type which generate largely low frequency dynamic tyre forces. This is an important consideration in the design of multiple-sensor weigh-in-motion systems.

A WIM system with one force sensor uses a single sample of a wheel force time history as an estimate of the static wheel load. For such a system, assuming 'perfectly accurate' sensors, it can be shown that the expected standard deviation of the error in static load estimation for a particular wheel is the RMS dynamic tyre force (see later). Thus the accuracy of a single sensor WIM system is limited fundamentally by vehicle dynamics. One solution to this problem is to ensure that the dynamic loads are small by building a very smooth lead-up to the WIM site of up to 120 m in length [16]. However, the advent of low cost WIM sensors provides the possibility of using two or more sensors along each wheel path in order to compensate for the effects of the dynamic forces in determination of the static axle loads.

There are a variety of ways in which the outputs of an array of sensors might be processed to yield an estimate of the static loads. Some possibilities are described by Glover [17] who performed numerical simulations of the outputs of WIM arrays with 1, 2, 9, 19 and 81 sensors with a variety of spacing arrangements, including uniform, linear, geometric and logarithmic. Glover achieved good results for a 9-sensor, evenly spaced array, using a least squares procedure to correct the simulated forces for the dominant Fourier component.

In this chapter, evenly spaced WIM arrays are examined. It is assumed that the outputs of the individual sensors are averaged to yield an estimate of the static loads. A general theory is developed which provides a straightforward design procedure for WIM arrays, providing the average speed of the heavy vehicle traffic is known. The simple averaging method requires very few sensors and little computation to give comparable accuracy to more sophisticated 'curve fitting' methods [17]. However, it has the disadvantage that the accuracy can be dependent on the speed of the traffic. As shown later in this chapter, this is not an important limitation, providing 3 or more sensors are used.

In Chapter 5, measurements from the load measuring mat will be used to examine the validity of the theory described here for six tractor/semi-trailer vehicle combinations.

Theory

Sinusoidal Input

It is useful to begin the analysis by calculating the output of a multiple-sensor WIM array to a sinusoidal force p(t) defined by

$$p(t) = P_0 + P\sin(\omega t + \phi) \tag{4.1}$$

where P_0 = static tyre force

P = dynamic tyre force amplitude

ω = angular frequency

ϕ = arbitrary phase angle

t = time.

The force is considered to move at constant speed V over an array of n sensors which are evenly spaced, distance Δ apart as shown in Figure 4.1. The sensors are assumed to be noiseless and perfectly accurate so that the output of each sensor is the instantaneous dynamic load applied to the sensor by p(t). The output of the array is taken to be the arithmetic mean of the individual sensor outputs, and is denoted $\overline{P}$. Assuming that t = 0 when p(t) passes over the first sensor, the array output (average) is

$$\overline{P} = P_0 + \frac{P}{n}\sum_{j=0}^{n-1} \sin\left(\frac{j\omega\Delta}{V} + \phi\right). \tag{4.2}$$

It is convenient to define the non-dimensional WIM error ε by

$$\varepsilon = (\overline{P}-P_0)/P \tag{4.3}$$

and the non-dimensional sensor spacing δ by

$$\delta = \omega\Delta/2\pi V = \Delta/(V/f), \tag{4.4}$$

where f = cyclic frequency corresponding to ω. Then (4.2) becomes

$$\varepsilon(n,\delta,\phi) = \frac{1}{n}\sum_{j=0}^{n-1} \sin(j2\pi\delta + \phi). \tag{4.5}$$

Assuming that ϕ is a random variable with a uniform probability density function $g(\phi)$, defined by

$$g(\phi) = \begin{cases} \frac{1}{2\pi} & -\pi < \phi \le \pi \\ 0 & \text{elsewhere,} \end{cases} \tag{4.6}$$

the expected mean square error can be found from (4.5) and (4.6) using standard expectation equations (see, for example, [18]) as follows :

$$E[\varepsilon(n,\delta,\phi)^2] = \int_{-\infty}^{\infty} \varepsilon(n,\delta,\phi)^2 g(\phi)\, d\phi$$

$$= \int_{-\pi}^{\pi} \left[\frac{1}{n}\sum_{j=0}^{n-1} \sin(j2\pi\delta + \phi)\right]^2 \frac{1}{2\pi}\, d\phi,$$

where E[ ] is the expectation operator.

With a little manipulation this can be shown to have the solution

$$E[\varepsilon(n,\delta,\phi)^2] = \frac{1}{2n} + \frac{1}{n^2}\sum_{k=1}^{n} (n-k)\cos(k2\pi\delta).$$

The Root Mean Square (RMS) error is then given by

$$\varepsilon_{RMS} = \sqrt{E[\varepsilon(n,\delta,\phi)^2]}.$$

It is useful to define the peak or 'envelope' error $\hat{\varepsilon}$ from the RMS error as follows:

$$\hat{\varepsilon}(n,\delta) = \pm\sqrt{2}\,\varepsilon_{RMS} = \pm\left[\frac{1}{n} + \frac{2}{n^2}\sum_{k=1}^{n} (n-k)\cos(k2\pi\delta)\right]^{1/2}. \tag{4.7}$$

Figure 4.2 shows a plot of eq. 4.5 for $n = 7$ with 5 different phase angles $\phi = 2\pi/5, 4\pi/5. \ldots 2\pi$, plotted as dashed lines. Superimposed on the plot is the envelope error $\hat{\varepsilon}$ as per eq. 4.7, plotted as the solid lines. It can be seen that the solid lines surround all of the dashed lines, and that $\hat{\varepsilon}$ is the largest error that can occur for any given value of δ. Thus an alternative interpretation of $\hat{\varepsilon}$ is the error corresponding to the 'worst-case' phase angle ϕ for an array with n sensors and non-dimensional spacing δ.

Figures 4.3 a-d show the characteristics of $\hat{\varepsilon}(n,\delta)$ for $n = 2$ to 5. Three observations are made:

(i) The error is unity for integer values of δ. These points correspond to the sample points (sensors) being spaced an integer number of dynamic force cycles apart.

(ii) The 'unit cell' pattern for $0 \le \delta < 1$ repeats for each integer value of δ and is symmetric about $\delta = 0.5, 1.5, 2.5$, etc. This is shown in Fig. 4.4 for $n = 6$. The repetition is a form of aliasing with a Nyquist spacing of $\delta = 0.5$. There is no apparent advantage in using $\delta > 1$ in a WIM array.

(iii) Within each 'unit cell', there are (n-1) zeros at values of $\delta = \delta_k$ corresponding to

$$\delta_k = k/n, \qquad k = 1, 2, 3...(n-1), (n+1), (n+2)... \qquad k \neq n, 2n, 3n... \tag{4.8}$$

Thus the range of δ between the first and last zeros in a unit cell ($\delta_1 = 1/n$ to $\delta_{n-1} = (n-1)/n$) increases with n. This is the region in which $\hat{\varepsilon}$ is consistently small.

Stochastic Input

For particular values of n, V and Δ, equation 4.7 can be considered to be a 'filter' transfer function which yields the worst-case error for dynamic force components of frequency ω. Using the standard input/output relationship for a linear system subject to ergodic random excitation [18], the mean square direct spectral density of the measurement error $S_{ee}(\omega)$ due to the 'two-sided' input tyre force spectral density $S_{pp}(\omega)$ is given by

$$S_{ee}(\omega) = \hat{\varepsilon}(n, \omega\Delta/2\pi V)^2 \; S_{pp}(\omega), \qquad -\infty < \omega < \infty. \tag{4.9}$$

The expected mean square value of a stationary random process is the area under the graph of mean square spectral density versus frequency, hence the worst case RMS array error σ for an n-sensor system is given by

$$\sigma(n) = \left[2\int_0^\infty \hat{\varepsilon}(n, \omega\Delta/2\pi V)^2 \; S_{pp}(\omega)\, d\omega \right]^{1/2}. \tag{4.10}$$

Equation 4.10 can be evaluated numerically if the input force spectral density $S_{pp}(\omega)$ is known. Determination of $S_{pp}(\omega)$ is discussed in section 4.3.

It should be noted that equation 4.10 yields the RMS error for one stationary random tyre force passing over an 'ensemble' of n-sensor WIM arrays. It can also be considered to be the expected standard deviation of the static load estimation error for many different axles passing over a single WIM site. This assumes that the wheel forces are sampled from an ergodic random process, which is reasonable under most circumstances [19]. It also assumes that the surface of the WIM array is not abnormally rough and that the individual suspensions all generate similar tyre force spectral densities.

Measures of WIM System Performance

It is useful to define some non-dimensional measures of WIM system performance. We define the 'Error Coefficient of Variation' (ECOV) ρ, for an n-sensor system by

$$\rho(n) = \sigma(n)/P_0, \tag{4.11}$$

where P_0 is the static axle load.

A parameter which is used frequently to characterise dynamic tyre forces is the Dynamic Load Coefficient (DLC) [9]:

$$\mathrm{DLC} = \frac{\text{RMS dynamic tyre force}}{\text{static tyre force}}. \tag{4.12}$$

For a single sensor WIM system (n = 1), equation 4.7 yields $\hat{\varepsilon}(1,\delta) = 1.0$ and equation 4.10 then gives

$$\sigma(1) = \left[2\int_0^\infty S_{pp}(\omega)\, d\omega \right]^{1/2},$$

which is simply the RMS dynamic tyre force, (the numerator of eq.4.12). Thus the DLC can alternatively be interpreted as

$$\mathrm{DLC} = \sigma(1)/P_0 = \rho(1). \tag{4.13}$$

Hence the expected error coefficient of variation of a single sensor WIM system $\rho(1)$ is simply the DLC of the dynamic axle loads. For highway conditions of road roughness and speed, DLC's in the range 0.1 - 0.3 are typical (ie. 10% to 30% RMS single-sensor WIM error), but DLC's up to 0.4 have been measured for particularly poorly damped tandem suspensions [9,12].

The proportional improvement in static load measurement accuracy relative to a single sensor WIM system is denoted here as the 'Static Accuracy Coefficient' (SAC), η which is defined by

$$\eta(n) = \frac{\rho(1)-\rho(n)}{\rho(1)} = \frac{\mathrm{DLC}-\rho(n)}{\mathrm{DLC}}. \tag{4.14}$$

η is a measure of multiple-sensor WIM performance.

If $\rho(n) = \rho(1)$, that is no improvement over a single sensor system, then $\eta(n) = 0$. Conversely, If $\rho(n) = 0$ (ie zero error), then $\eta(n) = 1.0$ which corresponds to 'perfect' WIM system performance.

Simulation

Calculation of Dynamic Tyre Force Spectral Densities

For a linearised vehicle model, the wheel force spectral matrix $[S_p(\omega)]$ can be found from the road profile input displacement spectral matrix $[S_u(\omega)]$ and a vehicle transfer function matrix $[H(\omega)]$, according to [19,20]:

$$[S_p(\omega)] = [H(\omega)]^* \, [S_u(\omega)][H(\omega)]^T \tag{4.15}$$

where '*' denotes the complex conjugate and '^{T}' denotes the matrix transpose. $[H(\omega)]$ is determined by standard methods from the equations of motion of the vehicle (see, for example, [21]).

The leading diagonal terms of $[S_u(\omega)]$ are the direct spectral density of the road profile displacement, given by [19,20]:

$$S_{jj}(\omega) = \frac{1}{V} S_u(\gamma = \omega/V), \tag{4.16}$$

where $S_u(\gamma)$ is the road profile displacement spectral density at wavenumber γ.

For a 2-dimensional (pitch plane) vehicle model, the off-diagonal (cross-spectral) elements of $[S_u(\omega)]$ are simply [19,20]:

$$S_{jk}(\omega) = S_{jj}(\omega)\, e^{-l_{jk}/V} \quad \text{and} \quad S_{kj}(\omega) = S_{jk}{}^*(\omega) \tag{4.17}$$

where l_{jk} is the distance between axles j and k.

Vehicle Models

It is important that the sensor averaging procedure is effective for a wide range of vehicles. The two simple generic vehicle models shown in Figs. 4.5a,b were chosen for this study because they represent the two main classes of truck suspensions. The '1/4-car' model in Fig. 4.5a represents those suspensions which generate a large low frequency wheel force spectral peak due to sprung mass motion. It has a 'sprung mass' natural frequency of approximately 1.9 Hz. The vast majority of current suspensions display this characteristic, as explained in Section 4.1. The 'walking-beam' model in Fig. 4.5b represents those suspensions (in the minority), which generate large dynamic wheel loads due to unsprung mass motion (lightly damped pitching of the walking-beam in this case).

The generic vehicle models do not contain the detailed suspension nonlinearities and complexities of sprung mass motion that are typical of heavy vehicles [7,13], however the wheel force spectral densities are sufficiently realistic for the purpose of this study of WIM systems.

Derivation of the equations of motion and formation of the transfer function matrix $[H(\omega)]$ are straightforward and will not be discussed here (see, for example, [13,21]).

Road Surface Profile Spectral Density

The road profile displacement spectral density $S_u(\gamma)$ used in the simulation study is the two-index function recommended in [22]:

$$S_u(\gamma) = \begin{cases} S(\gamma_0)\,|\gamma/\gamma_0|^{-n_1} & |\gamma| \le \gamma_0 \\ S(\gamma_0)\,|\gamma/\gamma_0|^{-n_2} & |\gamma| > \gamma_0. \end{cases} \tag{4.18}$$

The values used for the various constants are $n_1 = 2.0$, $n_2 = 1.5$, $\gamma_0 = 1.0$ rad/m and $S(\gamma_0) = 1.275 \times 10^{-6}$ m^3/rad, which correspond to the 'good' road surface classification in [22]. This profile may be likened to a UK 'A-class' road or fair motorway surface.

Simulation Results and array Design Considerations

Simulation Results for Vehicle Model 1

Figure 4.6 shows the wheel force spectral density $S_{pp}(\omega)$ and the error spectral density $See(\omega)$ (as calculated by eq. 4.9) for vehicle model 1 travelling at 100 km/h over a 3-sensor WIM array with a sensor spacing of $\Delta = 4$ m. The same data is plotted on both linear and logarithmic scales. On the linear graph, the area under the solid line is proportional to the DLC^2 and the area under the dashed lines is proportional to $\rho(3)^2$. The logarithmic graph is provided to show more clearly the attenuation of $S_{pp}(\omega)$ caused by $\hat{\varepsilon}(n, \omega\Delta/2\pi V)^2$. Because the maximum value of $\hat{\varepsilon}(n,\delta)$ is unity, (Fig. 4.3), $S_{ee}(\omega)$ can never exceed $S_{pp}(\omega)$, hence the dashed line can never cross the solid line. This means that for 'perfectly accurate' sensors, $\rho(n)$ can never exceed the Dynamic Load Coefficient (DLC).

Performance data corresponding to this simulation were: DLC = 0.142, $\rho = 0.051$ and $\eta = 0.645$. Thus in this case, the 3-sensor array reduces the error coefficient of variation from 14.2% to 5.1%, which corresponds to a 64.5% improvement in performance over a single sensor WIM system. This averaging scheme clearly improves substantially the accuracy of static wheel load prediction.

Figures 4.7a,b illustrate the influence of the sensor spacing Δ on the Error Coefficient of Variation ρ, and the Static Accuracy Coefficient η, for n=3 and vehicle model 1 travelling at speeds of 60 km/h and 100 km/h. It is apparent that for each speed, there is a range of spacings for which the WIM error (ECOV) is low, ie the system performs relatively accurately.

The shape of the ECOV curves is closely related to the magnitude of the error envelope curve $|\hat{\varepsilon}\ (n=3,\delta)|$ (shown in Fig. 4.3b), however because the system is subjected to an approximately narrow band random input (centred on the sprung mass natural frequency of the vehicle) instead of a single sine wave, the ECOV curve is a 'smoothed' version of $|\hat{\varepsilon}\,|$.

The properties of the $\hat{\varepsilon}$ curves, described in section 4.2.1 can be used to understand the features of the ECOV curves. From eq. 4.8, the first two zeros in $\hat{\varepsilon}(3,\delta)$ occur when $\delta_k = \delta_1 = 1/3$ and $\delta_2 = 2/3$. We expect these points to correspond approximately to minima in the ECOV curves. Using the definition of δ from eq. 4.4, with V = 16.7 m/s (60 km/h) and f=1.9 Hz (the dominant resonant frequency in $S_{pp}(\omega)$), we expect the minima to occur approximately at $\Delta = V/3f = 2.9$ m and $\Delta = 2V/3f = 5.9$ m. These points are labelled A and B on Figs. 4.7. The corresponding points for V = 27.8 m/s (100 km/h) are labelled A' and B'.

The worst errors are expected to occur when $|\hat{\varepsilon}(3,\delta)| = 1$. This happens when the dominant (resonant) frequency component in $S_{pp}(\omega)$ is sampled once every cycle (or once every two cycles), ie for integer values of δ. The points labelled C and C' on Figs. 4.7 correspond to $\delta_3 = 1$.

The labelled points on Fig. 4.7 are all slightly to the right of the maxima and minima of the ECOV curves at which they might be expected to occur. This is because $S_{pp}(\omega)$ is not symmetric about the main spectral peak, (see Fig. 4.6).

It is important that the WIM array is designed to be accurate for the widest possible range of vehicles (frequencies) and speeds. For given values of Δ and f, it is possible to estimate the range of vehicle speeds V over which the system will operate in the 'plateau region' of the ECOV curve where the accuracy is consistently high ($\eta \geq 0.5$).

From eq. 4.8, the zeros in $\hat{\varepsilon}(n,\delta)$ occur when

$$\delta_k = k/n, \qquad k = 1, 2, 3, \ldots\ldots (n-1). \tag{4.8}$$

We will ignore values of k > n, since these represent large (often impractical) sensor spacings at which the wheel forces are sampled at frequencies well below the Nyquist frequency: ie less than 2 sample points per cycle. Using eqs. 4.4 and 4.8, and assuming fixed Δ and f, the zeros occur at speeds V_k given by

$$V_k = \frac{\bar{f}n\Delta}{k}, \qquad k = 1, 2, 3 \ldots (n-1), \tag{4.19}$$

where $\bar{f}$ is the frequency of the dominant spectral component in $S_{pp}(\omega)$.

The 'plateau region' of the ECOV curve will be governed by the first and last zeros in $\hat{\varepsilon}$: k=1 and k = n-1. Thus the maximum and minimum speeds for which the WIM system will be reasonably accurate (operate in the 'plateau region') are given by

$$V_{max} = V_1 = \bar{f}n\Delta \tag{4.20}$$

and

$$V_{min} = V_{n-1} = \bar{f}n\Delta/(n-1). \tag{4.21}$$

A good design procedure would be to select Δ such that the average speed of vehicles using the road corresponds to the average of V_{min} and V_{max}. Thus combining (4.20) and (4.21),

$$\Delta_{design} = \frac{2\,(n-1)\bar{V}}{\bar{f}n^2}, \tag{4.22}$$

where $\bar{V}$ = estimated average traffic speed (m/s).

There is considerable variation in the dominant frequencies $\bar{f}$ in the dynamic wheel force spectra of common heavy vehicles. They are usually in the range 1.5 to 4.5 Hz and a suitable average value is $\bar{f}$ =2.5 Hz. It is possible that a slightly higher average frequency (say $\bar{f}$ = 3.0 Hz) may be more suitable for WIM systems in countries where heavy vehicle suspensions are relatively stiffer.

Figure 4.8 is design chart for multiple-sensor WIM arrays using eq. 4.22 with $\bar{f}$ = 2.5 Hz and n = 2-10. It yields values of Δ_{design} for speeds of 20, 40, 60, 80, 100 km/h.

Sensitivity to Frequency and Speed

Substituting the design spacing Δ_{design} (from eq. 4.22) back into eqs. 4.20 and 4.21 gives

$$V_{max} = 2(n-1)\overline{V}/n \tag{4.23}$$

and

$$V_{min} = 2\overline{V}/n. \tag{4.24}$$

If n=2, $V_{min} = V_{max} = \overline{V}$. Thus a 2-sensor WIM system can only be designed to be accurate at one speed. If n=3, however, $V_{min} = \frac{2}{3}\overline{V}$ and $V_{max} = \frac{4}{3}\overline{V}$ and a system with sensor spacing chosen according to (22) will be accurate for speeds of $\frac{2}{3}\overline{V} \leq V \leq \frac{4}{3}\overline{V}$. For example if $\overline{V}$ = 80 km/h, this, would yield $53 \leq V \leq 107$ km/h. Similarly if n=4, the range of accurate performance is given by $\frac{1}{2}\overline{V} \leq V \leq \frac{3}{2}\overline{V}$.

Figures 4.9a,b show the ECOV and SAC for 2-, 3- and 4-sensor WIM systems designed for an average speed of 80 km/h ($\overline{V}$ = 22.2 m/s) according to eq. 4.22 with $\overline{f}$ = 1.9 Hz. The systems are traversed by vehicle model 1. Also shown in Fig. 4.9a is $\rho(1)$ (the DLC) for comparison.

Three observations are made:

(i) In the vicinity of 80 km/h, an increase in the number of sensors yields a modest increase in accuracy (η = 0.6 for n = 2, η = 0.67 for n = 4.)

(ii) The 2-sensor system loses accuracy quite quickly for speeds away from 80 km/h, whereas the 3-sensor system has an accurate 'plateau region' for $53 \leq V \leq 107$ km/h as expected. The 4-sensor system is accurate over an even wider speed range.

(iii) For speeds less than about 30 km/h, the ECOV (ρ) and SAC (η) curves fluctuate rapidly due to aliasing.

From Figure 4.9 it appears that 3 sensors is a good choice, because the system is reasonably accurate and has a relatively wide operating speed range. The 4-sensor system yields a larger speed range with only a small accuracy improvement over the 3-sensor system. The additional cost of the 4th sensor may not be worthwhile in practice.

The range of frequencies over which the WIM array will be accurate for a given vehicle speed $\overline{V}$ can be found by rearranging eq. 4.19:

$$f_{min} = \overline{V}/n\Delta \tag{4.25}$$

and

$$f_{max} = (n-1)\overline{V}/n\Delta . \tag{4.26}$$

If Δ is replaced by Δ_{design} from (4.22), then (4.25) and 4.26) give

$$f_{min} = n\bar{f}/2(n-1) \tag{4.27}$$

and

$$f_{max} = n\bar{f}/2\ . \tag{4.28}$$

Thus if n=2, $f_{min} = f_{max} = \bar{f}$, that is the system can only be tuned to perform well at one input frequency. If n=3, the operating frequency range (for a fixed speed) is approximately $\frac{3}{4}\bar{f} \leq f \leq \frac{3}{2}\bar{f}$. For $\bar{f} = 2.5$ Hz this gives $1.9 \leq f \leq 3.8$ Hz. Similarly if n=4, the operating frequency range is $\frac{2}{3}\bar{f} \leq f \leq 2\bar{f}$ which, for $\bar{f} = 2.5$ Hz, yields $1.7 \leq f \leq 5$ Hz. Thus n=3 is a reasonable choice, although errors may occur when the frequency and speed take extreme values simultaneously. The worst error is likely to occur when $V \approx V_{max}$ and $f \approx f_{min}$ although the other extreme condition ($V \approx V_{min}$ and $f \approx f_{max}$), may also yield significant errors.

Figures 4.10a,b show the variation of ECOV (ρ) and SAC (η) with the number of 'optimally spaced' sensors, ie sensors spaced according to eq. 4.22. The vehicle (model 1) is travelling at the array design speed of 80 km/h. The design frequency is $\bar{f} = 2.5$ Hz which is above the first natural frequency of the vehicle model (1.9 Hz). Figures 4.10a,b show that good performance can be achieved with a 2- or 3-sensor system (providing the 2-sensor system is operated close to its design conditions.) Figures 4.10 also show that diminishing benefits are achieved for larger numbers of sensors. In this case, ρ is reduced from 12.3% for a single sensor WIM system to 3.9% for a 3-sensor array, but only to 3.0% for a 10 sensor system. Similar curves to Figs. 4.10 can be obtained by running the simulation at other speeds.

Simulation Results for Vehicle Model 2

Vehicle model 2 has a walking-beam suspension which generates large dynamic tyre forces due to beam pitching at approximately 9 Hz as well as a lower frequency component, of smaller amplitude, due to sprung mass bounce at approximately 2.8 Hz. If the WIM array is designed for the lower frequency component, then significant errors may be expected due to the higher frequency loads. Conversely, an array designed to be accurate for the higher frequency tyre force component of this particular vehicle may be inaccurate for (the majority of) vehicles which generate predominantly low frequency dynamic loads. This trade-off is examined in the remainder of this section.

Figure 4.11 shows the leading axle tyre force and error spectral densities, $S_{pp}(\omega)$ and $S_{ee}(\omega)$, for vehicle model 2 operating at 100 km/h on a 3-sensor WIM array designed for $\bar{f} = 2.5$ Hz, according to eq. 4.22, with $\Delta = 5$ m (see design chart, Fig. 4.8). Again the spectra are plotted on both linear and logarithmic scales. The peak in $S_{pp}(\omega)$ at $\omega = 57$ rad/s (9 Hz) is substantially larger than the peak at 18 rad/s (2.8 Hz). This is typical of the characteristics of walking-beam suspensions (see, for example, Ervin et al [10]).

The WIM array is surprisingly effective at reducing the error throughout the frequency range, even though it is tuned to the lower frequency peak. In this case, DLC ≈ 0.36, $\rho = 0.13$ and $\eta = 0.64$. It should be noted, however that the higher frequency performance is very sensitive to V/f, where f is the frequency of the beam pitching mode.

Figure 4.12 displays similar information to Figure 4.9, (the ECOV and SAC plotted against speed for various arrays) but for vehicle model 2. In this case the array is designed according to eq. 4.22 with $\bar{V} = 80$ km/h and $\bar{f} = 2.5$ Hz. Unlike Fig. 4.9, the system is not well tuned for 80 km/h vehicles and the optimum speed depends on the number of sensors in the array (for 2 sensors, the optimum speed is approximately 100 km/h). This is the result of under-sampling (aliasing) the higher frequency loads. The various peaks and troughs in Fig. 4.12 can be predicted relatively well by considering $\hat{\varepsilon}(n,\delta)$ for loads at 9 Hz.

Figure 4.13 shows the variation of WIM accuracy with the number of sensors, for arrays which are spaced according to eq. 4.22 with $\bar{V} = 80$ km/h and $\bar{f} = 2.5$ Hz. In this particular case, the 3- and 4-sensor systems perform well but the 6-sensor system is quite inaccurate. This is because the spacing for 6 sensors with $\bar{f} = 2.5$ Hz (according to eq. 4.22) is 2.47 m which coincides exactly with $\delta=1$ for the 9 Hz peak (ie the worst possible spacing for the 9 Hz wheel forces).

In Figures 4.11 to 4.13, the WIM arrays were designed to account for the low frequency dynamic wheel forces. An alternative strategy might be to tune the system performance to the high frequency forces by using arrays with smaller spacings (around 1-2 m). This turns out to be unsatisfactory as illustrated in Fig. 4.14, which shows the performance of WIM arrays designed with $\bar{f} = 9$ Hz at $\bar{V} = 80$ km/h according to eq. 4.22. It can be seen clearly that the accuracy is good for the walking-beam suspension (model 2) as expected, but poor for 1/4-car vehicle (model 1). The heavy highway vehicle fleet consists largely of vehicles like model 1 and it is not worthwhile to compromise the performance of the WIM system for these vehicles in order to account for the small number of suspensions like model 2.

Effect of Transducer Errors

Real WIM transducers are not perfectly accurate or noise-free and may introduce small random errors into the dynamic axle load measurements. For well-designed sensors, these errors should be considerably less than the DLC and may be just a few percent [8]. They will be reduced further by the force averaging process. Assuming that the noise on each sensor in the array is not correlated with the noise on any other sensor, it is expected from the central limit theorem that the error standard deviation due to noise will fall approximately as $1/\sqrt{n}$. Hence there may be some benefit in using more sensors than indicated by the 'ideal sensor' theory outlined here, depending on the noise level (and cost of the sensors). The sensors should still be spaced according to equation 4.22. This issue is discussed in more detail in the next chapter.

Conclusions

(i) A general theory has been developed for the analysis of multiple-sensor WIM arrays with ideal, error-free force transducers, spaced evenly along the road. The theory yields a simple formula (equation 4.22) by which the sensor spacing can be chosen if the average traffic speed is known.

(ii) A two-sensor WIM array can be designed to be relatively accurate for vehicles which generate dynamic loads at a known resonant frequency and travel at a known speed. Such a system becomes less accurate for speeds or frequencies away from the design conditions.

(iii) The accuracy of a WIM array improves gradually as the number of 'optimally' spaced sensors is increased above 2, with diminishing improvements for large arrays. However, the robustness (insensitivity) to speed and frequency variations improves markedly with more sensors.

(iv) An array designed for low frequency dynamic loads (1.5 Hz to 4.5 Hz) *may* be inaccurate for (a minority of) vehicles with poorly-damped tandem suspensions such as walking-beams, which generate large dynamic loads at high frequencies (8 to 15 Hz). For these vehicles the array accuracy will be quite sensitive to the speed and frequency of the dynamic loads. Conversely, an array which is tuned to be accurate for high frequency loads *will consistently* be inaccurate for the majority of vehicles which generate their dynamic tyre forces at low frequencies. Thus it is preferable to design the spacing of WIM arrays to account for low frequency dynamic loads.

(v) A good compromise for WIM array design is to use 3 sensors tuned to a mean vehicle resonant frequency of approximately $\bar{f} = 2.5$ Hz. This yields reasonable accuracy for a wide range of speeds and dynamic loading frequencies. With such an arrangement, the theoretical coefficient of variation of the measurement error can be reduced to 30-50% of the error for a single sensor WIM system.

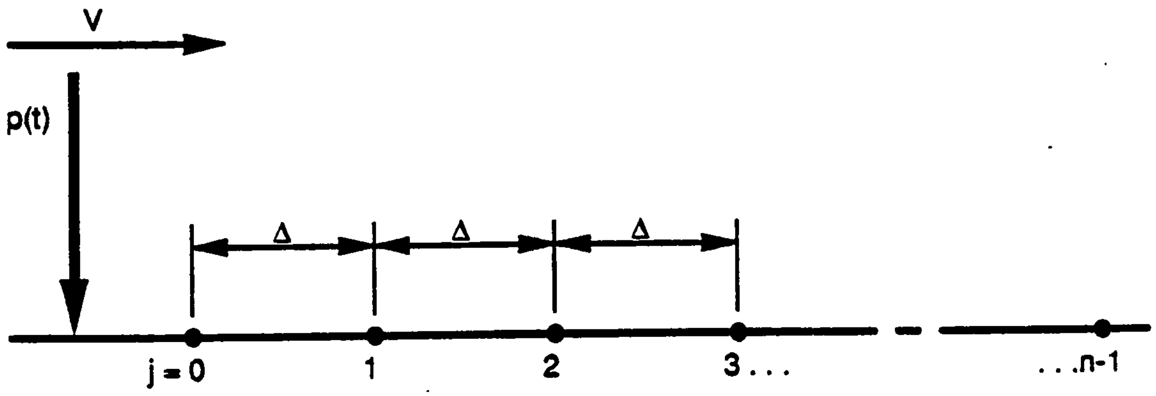

Fig 4.1. Cross-section of n-sensor WIM array, traversed by force p(t) at speed V.

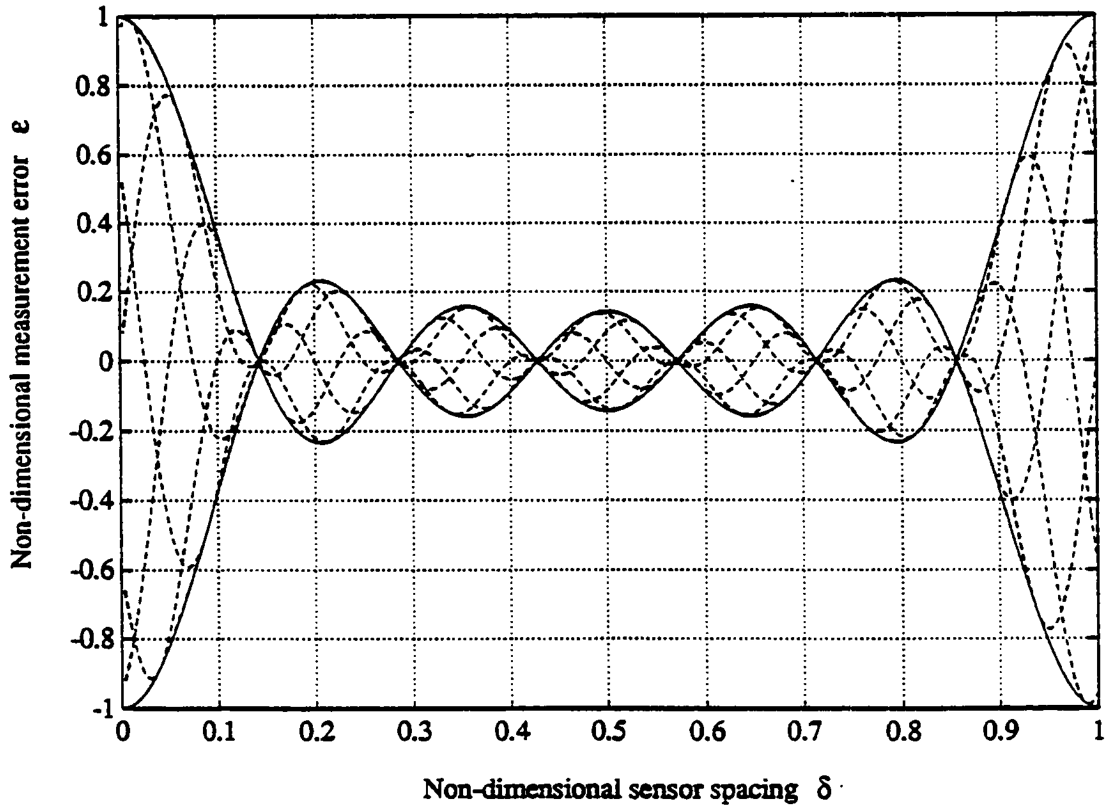

Fig. 4.2 Plot of equation 4.5 for n=7 with 5 different phase angles, $\phi = 2\pi/5, 4\pi/5. \ldots 2\pi$, (dashed lines) as well as the envelope error $\hat{\varepsilon}$ from eq. 4.7, (solid lines).

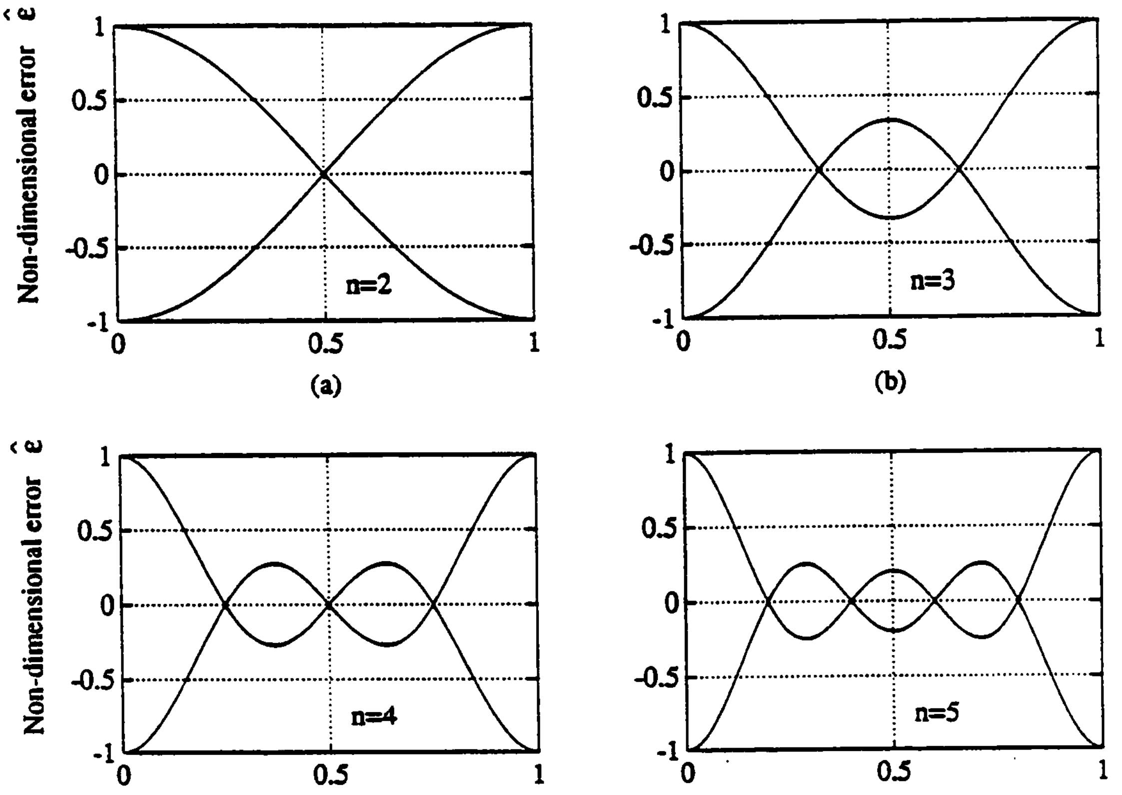

(a) (b) (c) (d)

Fig 4.3. Plots of the envelope error $\hat{\varepsilon}$ from equation 4.7 (a) n=2, (b) n=3, (c) n=4, (d) n=5.

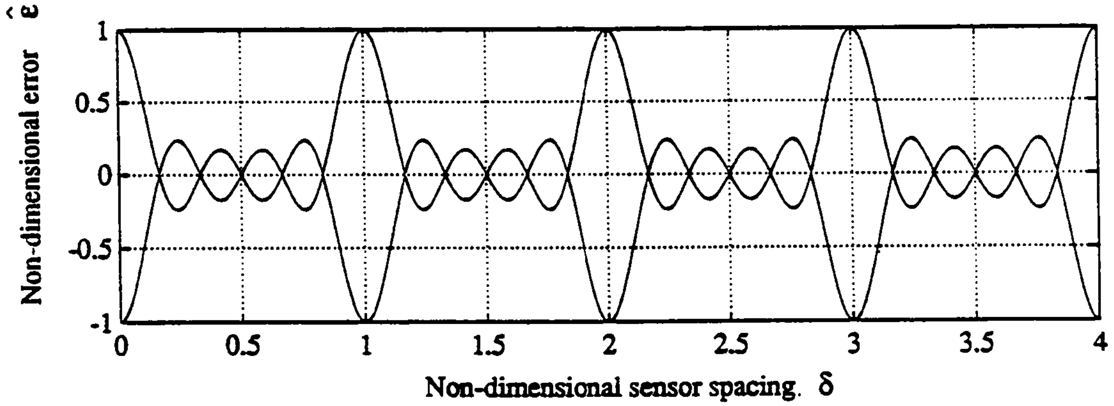

Fig. 4.4 Plot of the envelope error $\hat{\varepsilon}$ from equation 4.7 with n=6, showing the repetition of the 'unit cell' pattern $(0 \le \delta < 1)$ due to aliasing.

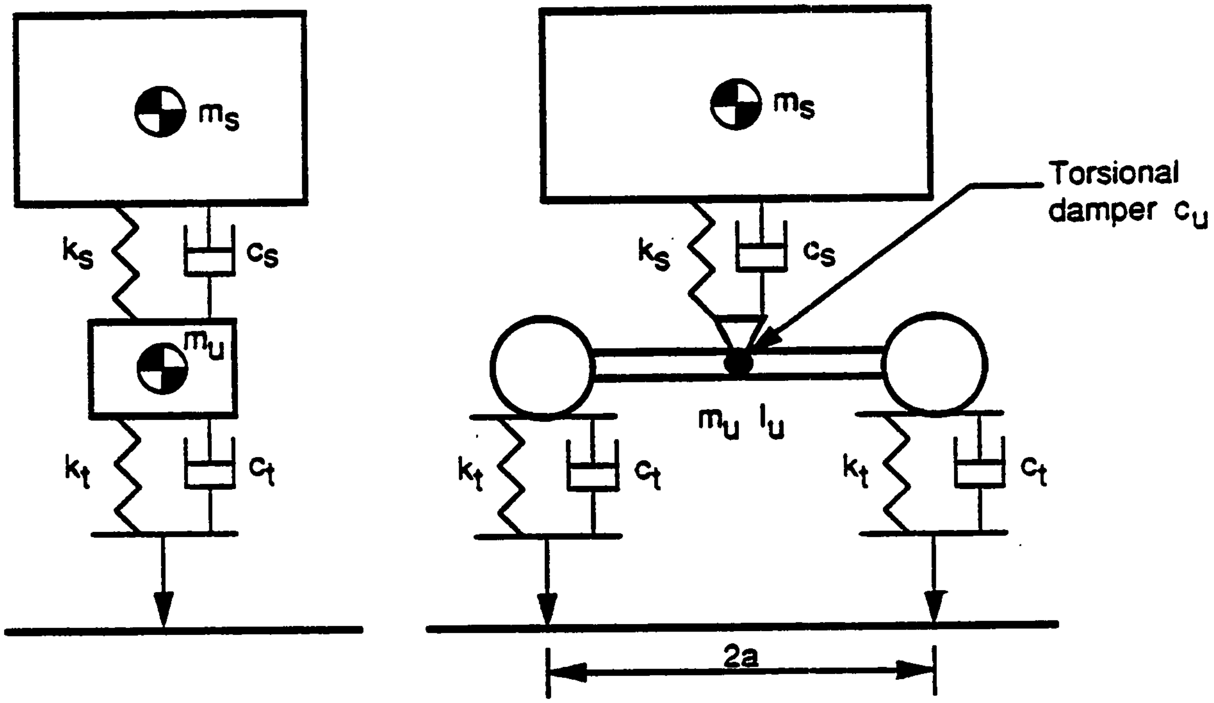

m_s = 8900 kg
m_u = 1100 kg
c_s = 30 kNs/m
c_t = 4 kNs/m
k_s = 2000 kN/m
k_t = 3500 kN/m

m_s = 7800 kg
m_u = 2200 kg
I_u = 930 kgm^2
c_s = 60 kNs/m
c_t = 4 kNs/m
c_u = 3 kNms/rad
k_s = 4000 kN/m
k_t = 3500 kN/m
a = 0.65 m

(a) (b)

Fig. 4.5 Schematic diagrams of the two vehicle models
(a) Model 1: 2 degrees of freedom, '1/4-car'
(b) Model 2: 3 degrees of freedom, 'walking-beam.'

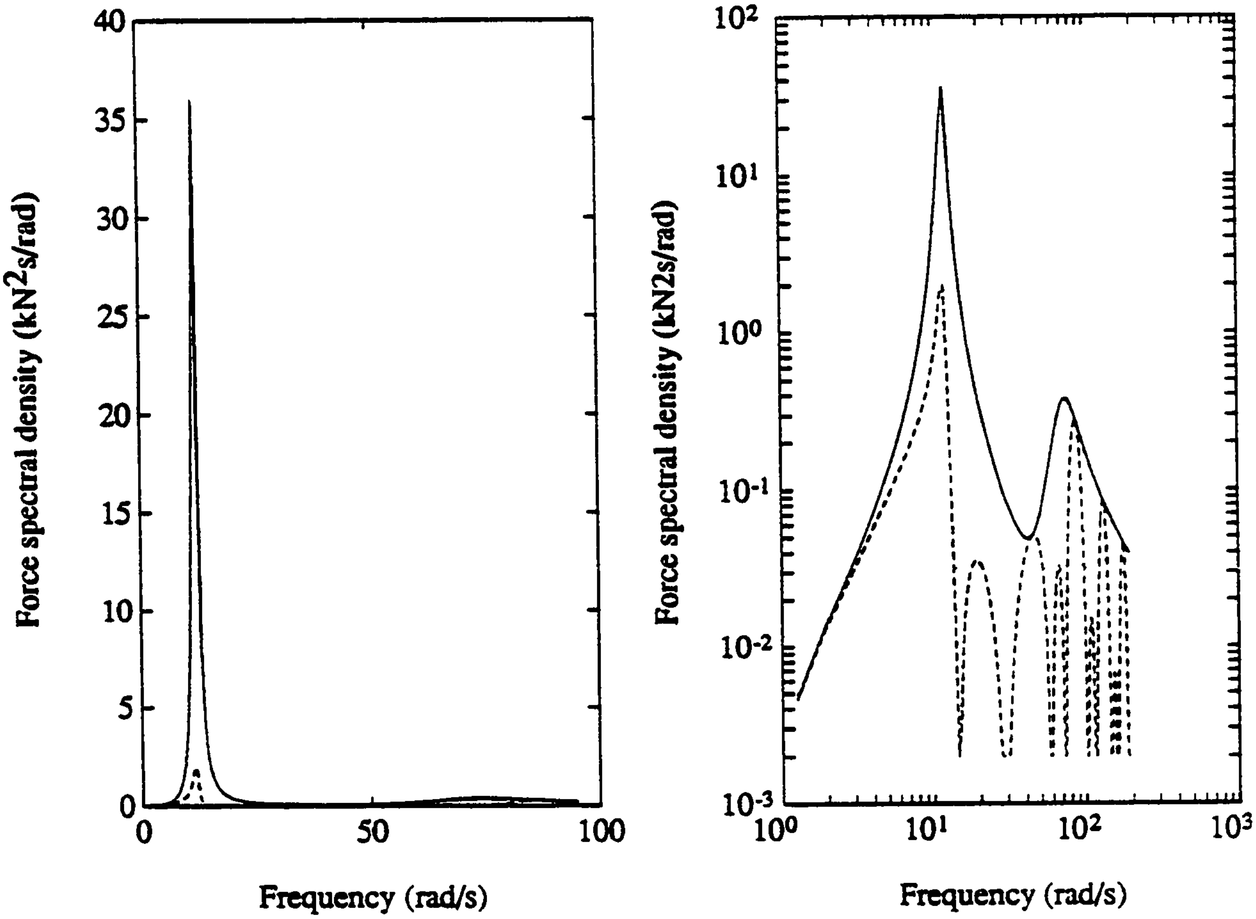

Fig. 4.6 Tyre force spectral density $S_{pp}(\omega)$ and the WIM array error spectral density $S_{ee}(\omega)$ for vehicle model 1 travelling at 100 km/h over a WIM array with n=3 and $\Delta = 4$ m.

———— = $S_{pp}(\omega)$, - - - - - = $S_{ee}(\omega)$.

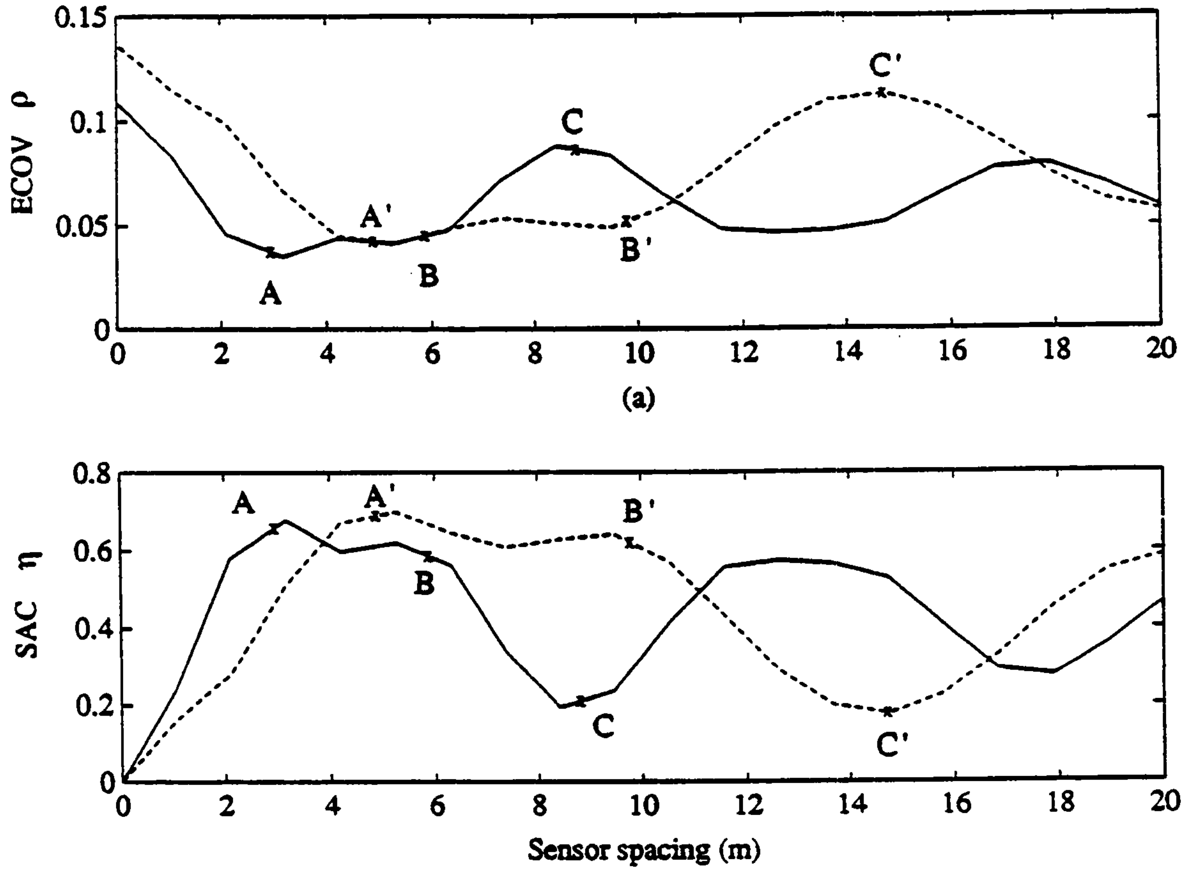

(a) (b)

Fig. 4.7 WIM system performance versus sensor spacing Δ for vehicle model 1. Points A, B, C etc. were calculated according to the theory for sinusoidal inputs. (a) Error Coefficient of Variation ρ. (b) Static Accuracy Coefficient η. ——— = 60 km/h, - - - - = 100 km/h

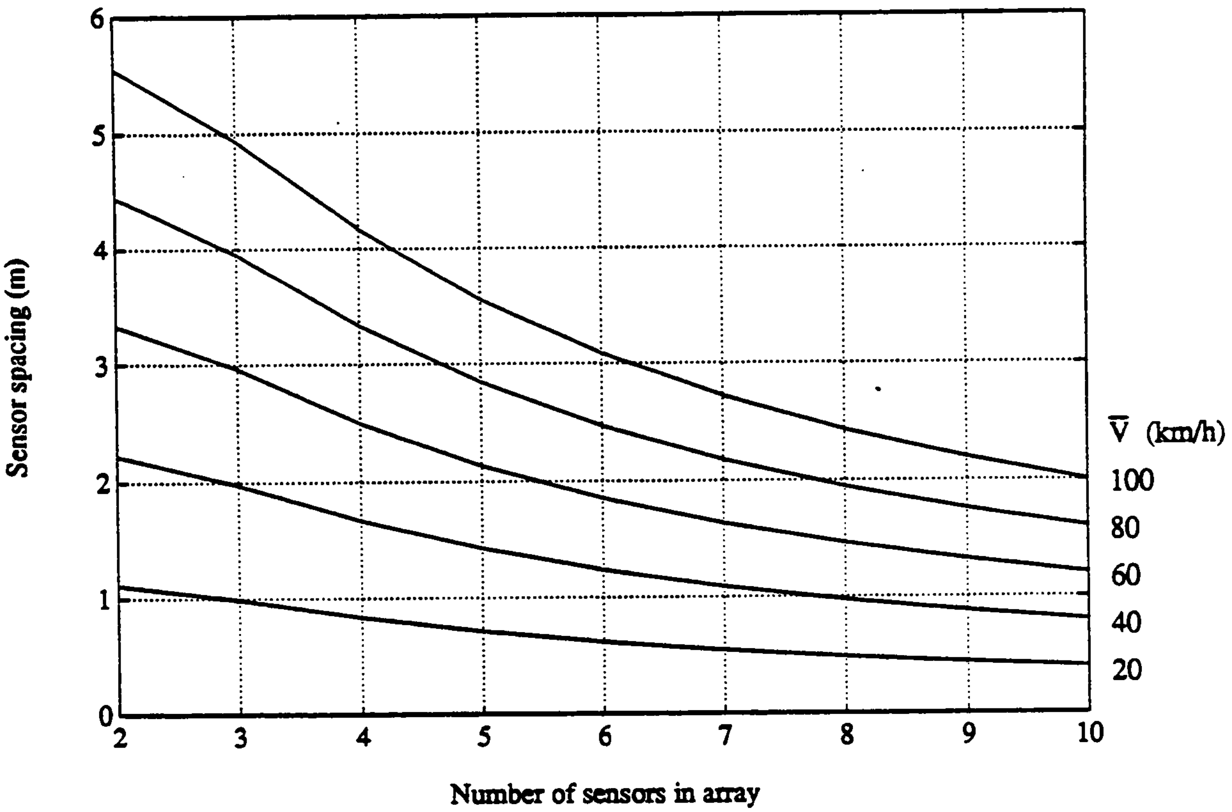

Fig. 4.8 Design chart for multiple sensor WIM systems using eq. 4.22 with $\bar{f}$ = 2.5 Hz.

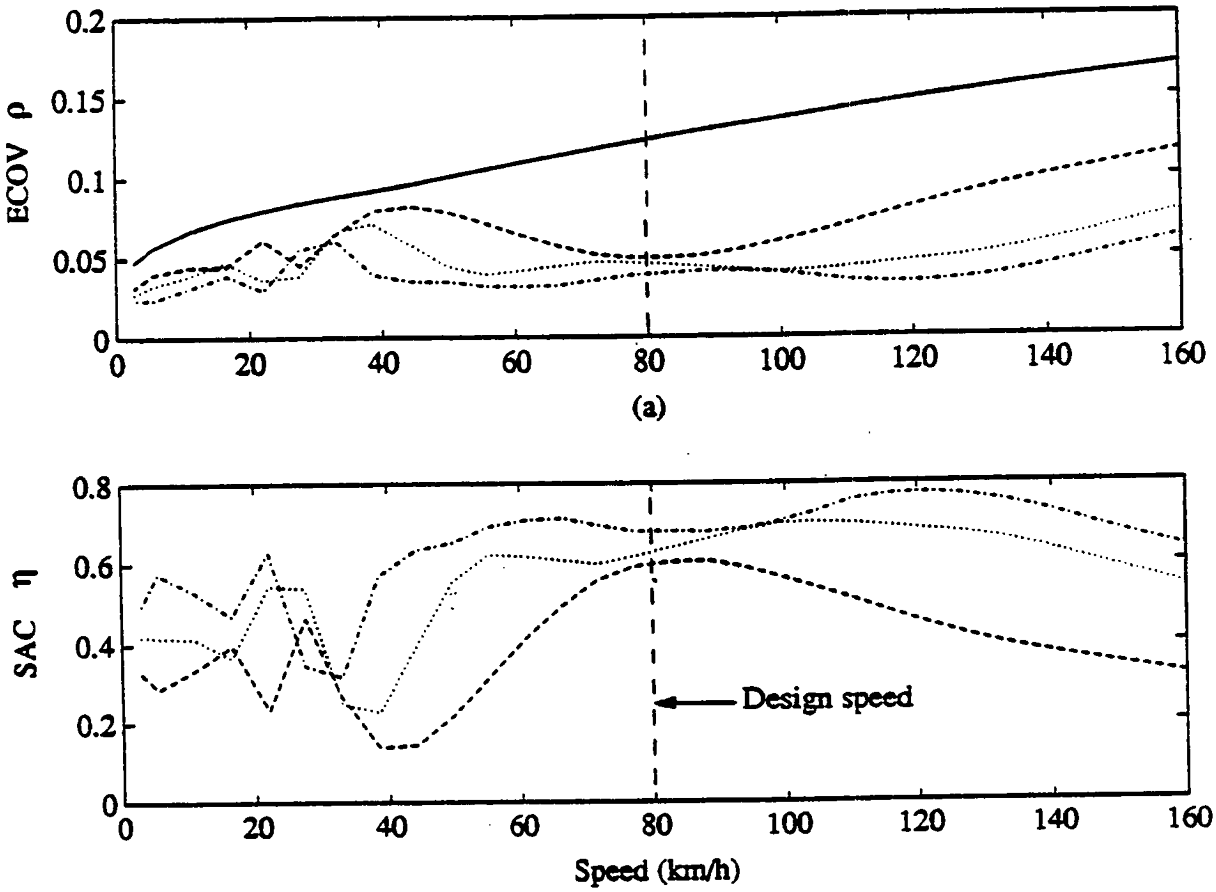

(b)

Fig. 4.9 Influence of speed on the performance of 2-, 3- and 4-sensor WIM systems, designed for an average traffic speed of 80 km/h, traversed by vehicle model 1. (a) Error Coefficient of Variation ρ. (b) Static Accuracy Coefficient η.
———— n=1 (DLC), - - - - - n=2, ·········· n=3, -·-·-·-· n=4.

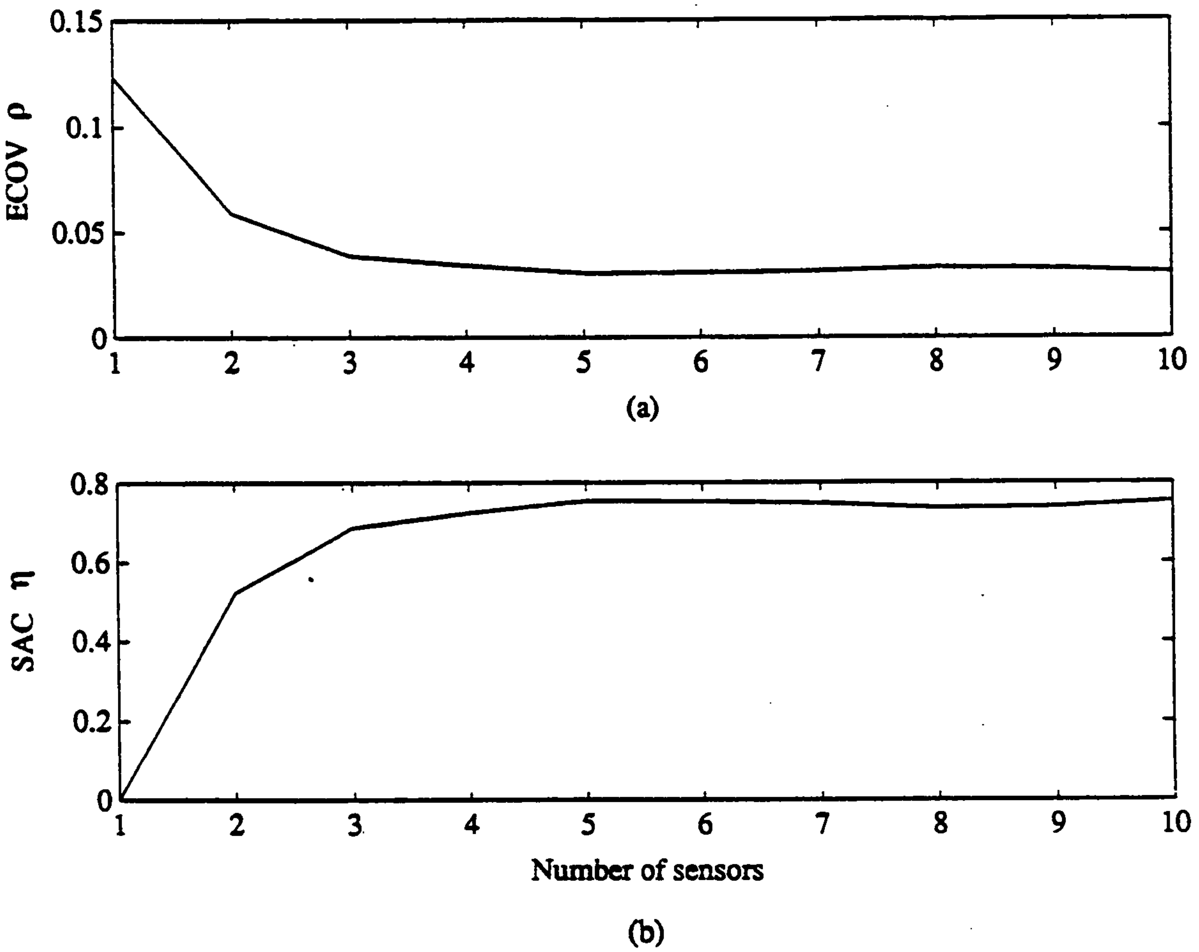

Fig 4.10 Variation of WIM system performance for vehicle model 1 with the number of sensors in the array. The sensors are spaced according to eq. 4.22 with $\bar{f} = 2.5$ Hz and the vehicle is travelling at the array design speed of 80 km/h.
(a) Error Coefficient of Variation ρ, (b) Static Accuracy Coefficient η.

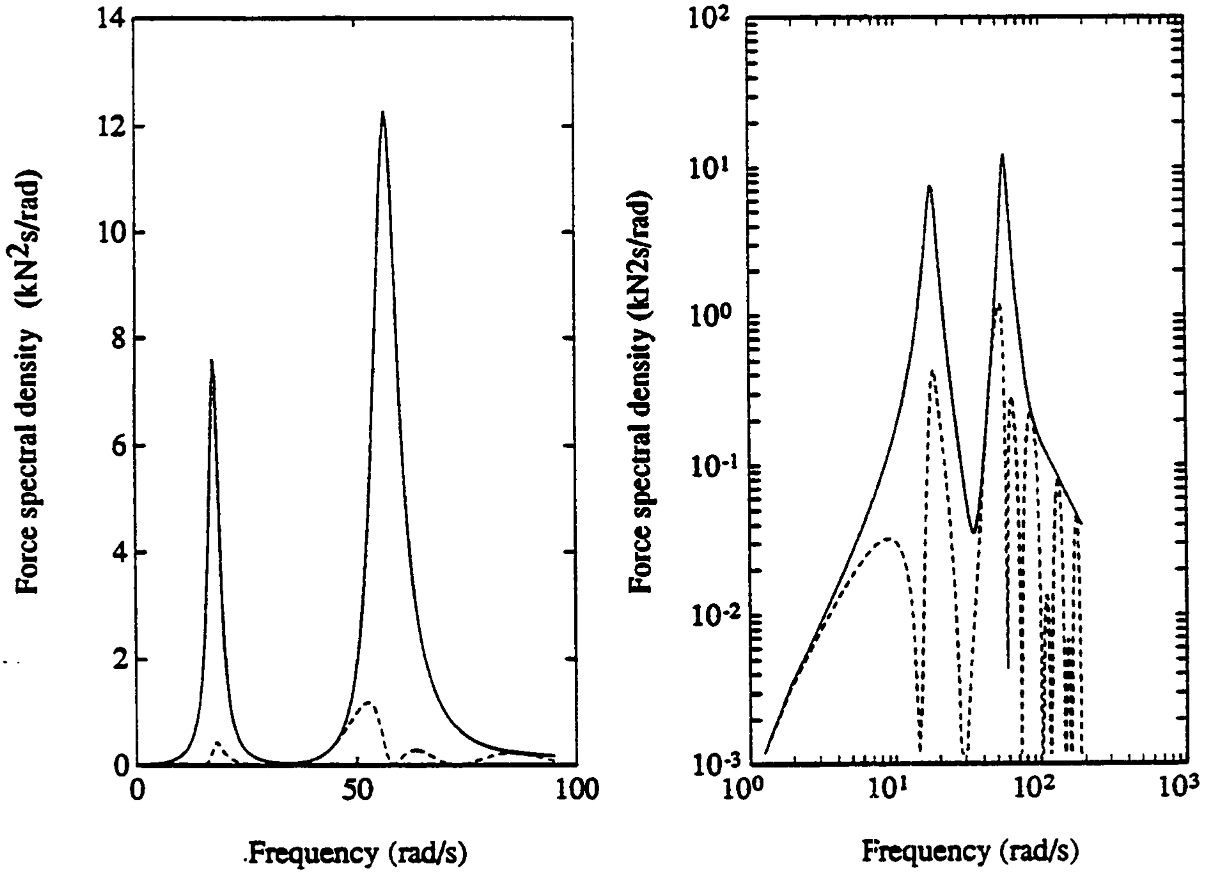

Fig 4.11 Leading tyre force and error spectral densities $S_{pp}(\omega)$ and $S_{ee}(\omega)$ for vehicle model 2 travelling at 100 km/h over a WIM array with n=3 and $\Delta = 5$ m.
———— = $S_{pp}(\omega)$, - - - - - - = $S_{ee}(\omega)$.

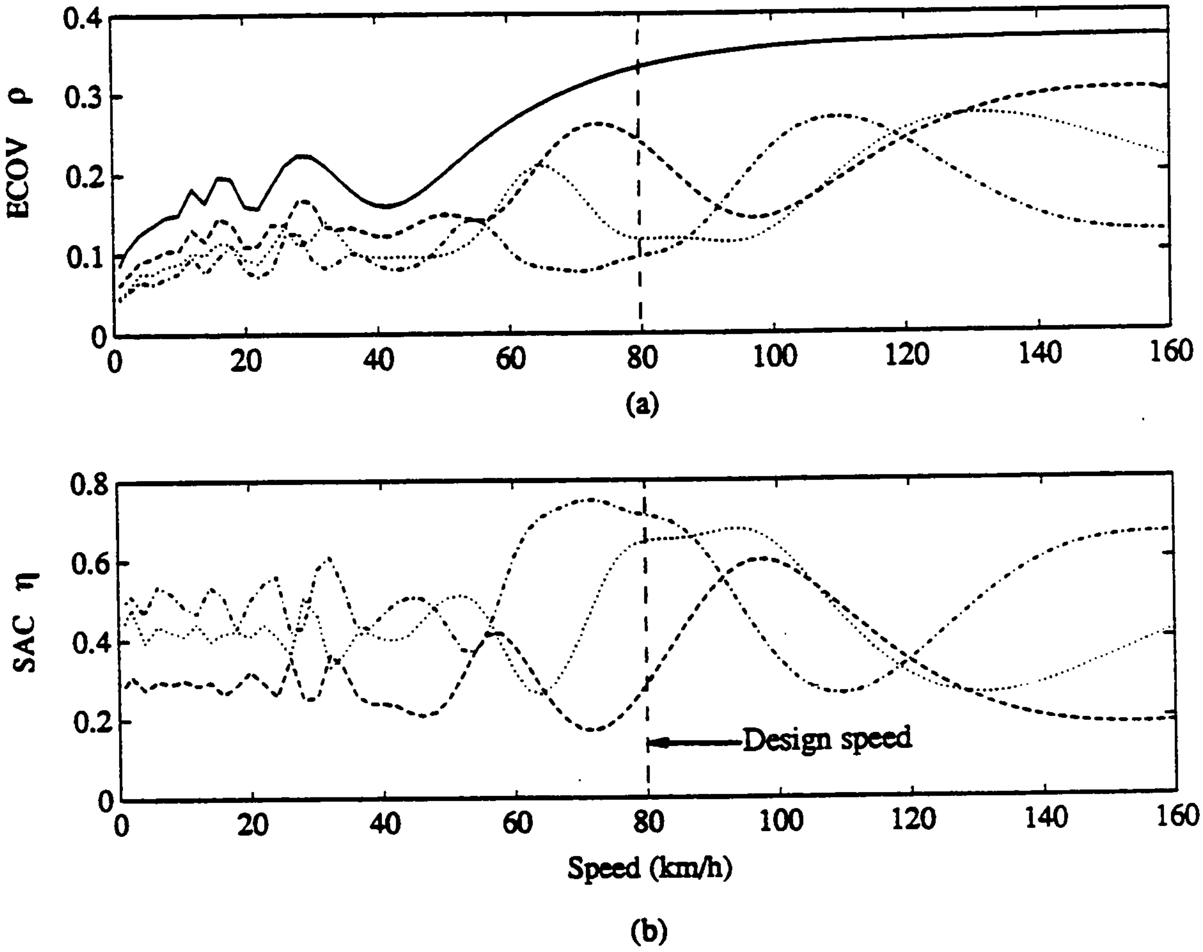

Fig 4.12 Influence of speed on the performance of 2-, 3- and 4-sensor WIM systems, designed for $\bar{f} = 2.5$ Hz and $\bar{V} = 80$ km/h, and trafficked by vehicle model 2. (a) Error Coefficient of Variation ρ, (b) Static Accuracy Coefficient η. ———— n=1(DLC), – – – – n=2, ········ n=3, -·-·-·- n=4.

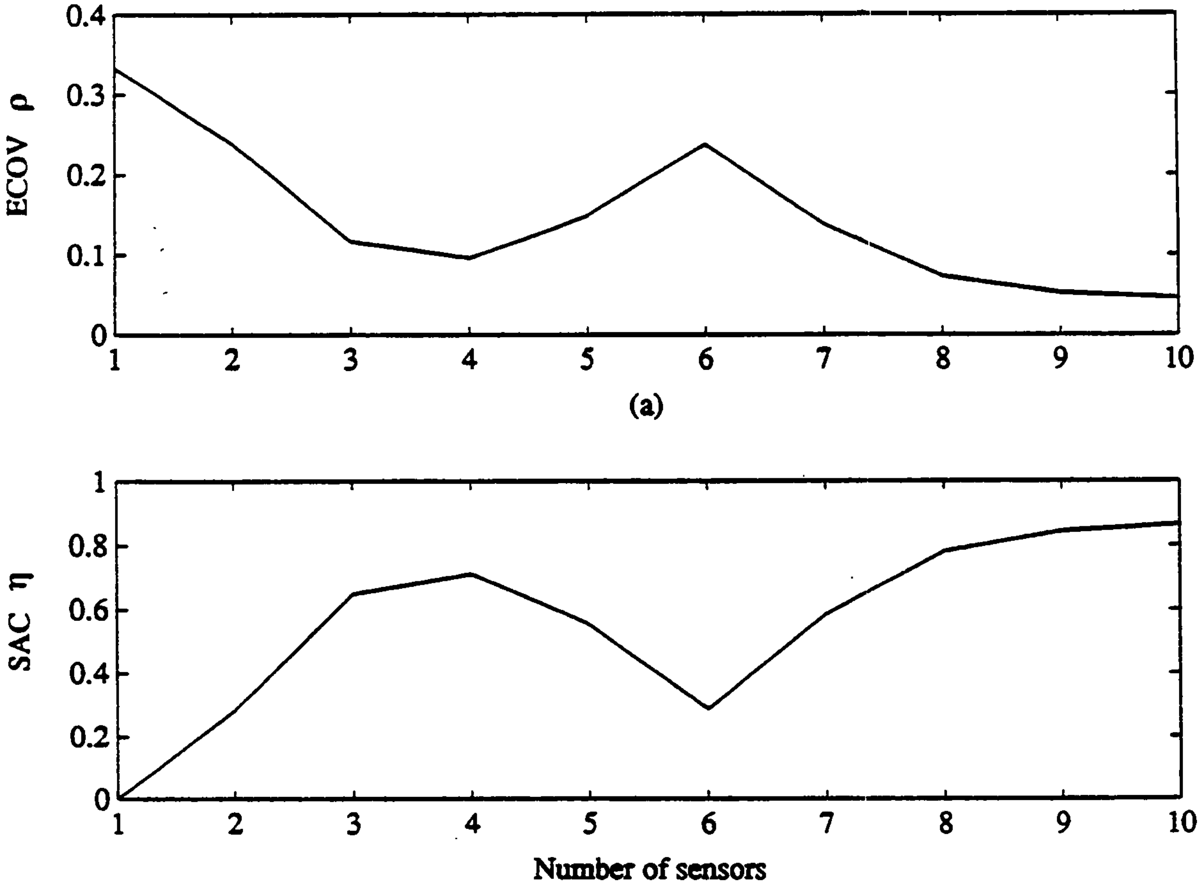

(b)

Fig 4.13 Variation of WIM system performance for vehicle model 2 with the number of sensors in the array. The sensors are spaced according to eq. 4.22 with $\bar{f}$=2.5 Hz and the vehicle is travelling at the array design speed of 80 km/h. (a) Error Coefficient of Variation ρ, (b) Static Accuracy Coefficient η.

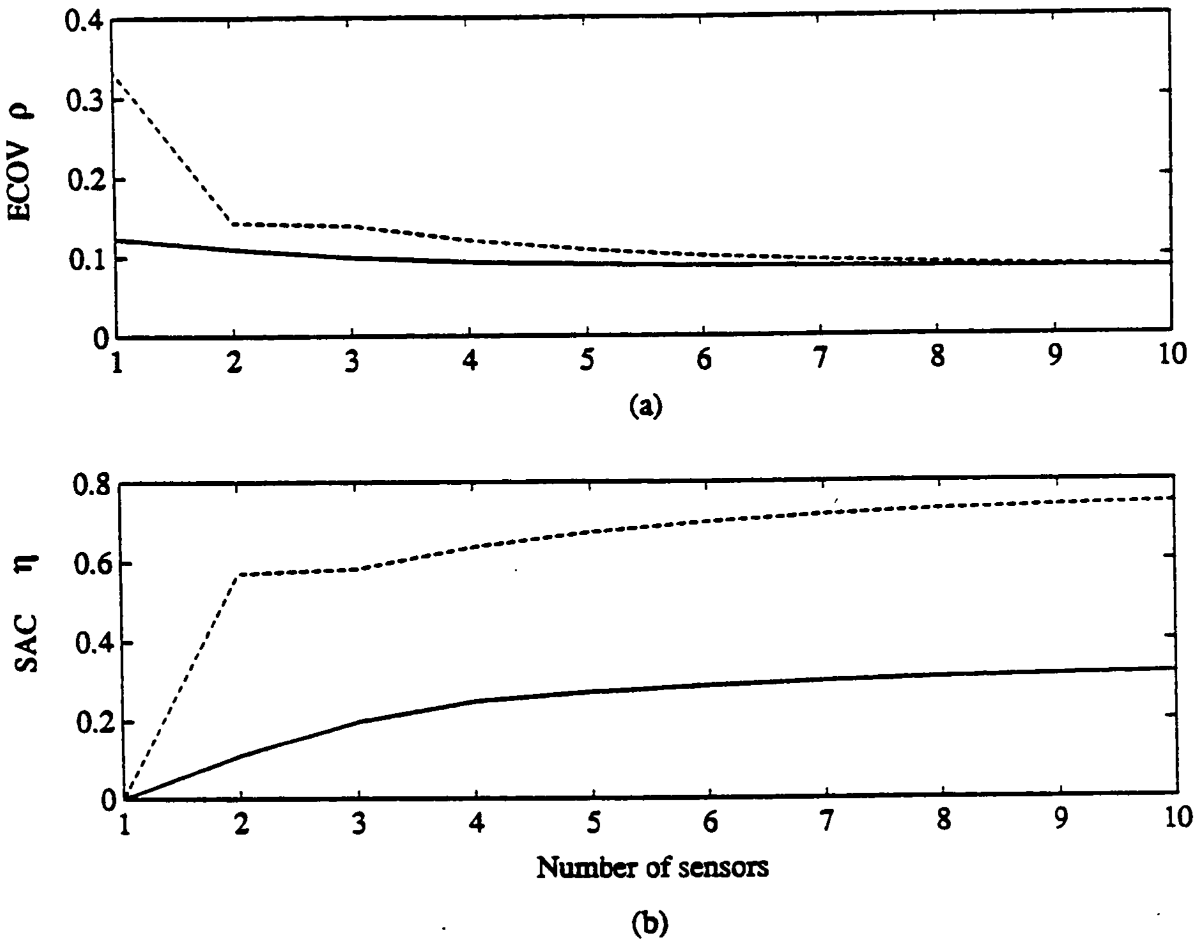

Fig 4.14 Variation of WIM system performance for vehicle models 1 and 2 with the number of sensors in the array. The sensors are spaced according to eq. 4.22 with $\bar{f}$=9 Hz and the vehicles are travelling at the array design speed of 80 km/h.
(a) Error Coefficient of Variation ρ (b) Static Accuracy Coefficient η.
———— Vehicle model 1, ------ Vehicle model 2.

5

WIM Performance for Six Test Vehicles

In this section, wheel force data collected with the load measuring mat is used to examine the design and accuracy of WIM systems with up to six evenly-spaced sensors.

Data Analysis Procedure

The calibrated and sorted 'ERD' data files for the six articulated test vehicles (section 2.1.3) were processed to determine the Error Coefficient of Variation (ECOV = ρ) as a function of WIM array design parameters (n and Δ), for each axle at the six nominal testing speeds (5, 10, 20, 30, 40, 50 mph). Figure 5.1 shows an example of the procedure, in which many 3-sensor WIM arrays ($n = 3$) with $\Delta = 1.6$ m can be obtained by averaging the outputs of appropriately spaced groups of sensors. (Eighty eight such averages ($n = 3$, $\Delta = 1.6$ m) can be calculated for each axle from an ERD file with 96 sensors: 88 = 96 - 8, since each WIM array spans 8 sensors as shown in Fig. 5.1). Averages of this type were calculated for sensor spacings, $\Delta = 0, 0.4, 0.8....12$ m and n = 2 to 6 sensors, i.e. 155 different WIM array configurations in all.

For each vehicle, the steps in the automated data analysis procedure were as follows:

(i) Read all ERD files for each nominal testing speed in both 'forward' and 'reverse' directions around test track.

(ii) For each axle, calculate 155 different ensembles of WIM force averages (n = 2 to 6 and $\Delta = 0, 0.4, 0.8....12$ m).

(iii) Convert each ensemble into a frequency (probability) distribution of WIM force against number of occurrences. (Total of 155 frequency distributions for each axle.)

(iv) Combine the frequency distributions for all ERD files at the same nominal testing speed.

(v) Calculate the mean, standard deviation and error coefficient of variation from each of the frequency distributions.

(vi) Plot the error coefficient of variation ρ against sensor spacing Δ for n = 2 to 6, for each axle.

Histograms of WIM force averages, step (iv) are provided for vehicle S1 travelling at a speed of 32 km/h (9 m/s) in Fig. 5.2a,b,c. Figure 5.2a shows the force distribution for the steering axle calculated by considering each transducer to be a separate WIM system (i.e. by setting $\Delta = 0$). Figure 5.2b shows the result of analysing the same data as Fig. 5.2a, but with 3-sensor averages ($n = 3$) and $\Delta = 1.6$ m. Similarly, Fig. 5.2c shows the result of analysing the data with 6-sensor averages ($n = 6$) and $\Delta = 0.8$ m. It is apparent from the figures that the spread of the probability distribution (Error Coefficient of Variation) is reduced considerably by performing the 3-sensor averages. The ECOV ρ is reduced from 6.5% for the single-sensor system to 3.9% for the 3-sensor system and to 3.2% for the 6-sensor system.

Similar results can be seen in Figs. 5.2 d,e,f which show the results for axle 5 on the trailer of vehicle S4 travelling at 85 km/h. The single sensor WIM force distribution in Fig 5.2 d has an ECOV ρ of 11.5%. This is reduced to 5.8 % for the 3-sensor average in Fig. 5.2 e and 4.2% for the 6-sensor average in Fig. 5.2 f.

In each of these cases, the sensor spacing was was calculated from the design equation (4.22) with $\overline{V}$ set to the testing speed and $\overline{f} = 2.5$ Hz. The two cases presented here (S1 at 32 km/h and S4 at 85 km/h) will be examined further in the following sections.

Preliminary Comparison of Experiment and Theory

A graph of ρ vs Δ for the steering axle of vehicle S1 at 32 km/h (9 m/s) is provided in Fig. 5.3. (This Fig is repeated later as Fig. 5.14 a). The vertical lines on the figure labelled n = 2 - 6 correspond to the design spacing Δ_{design} as calculated from equation 4.22 with $\overline{V} = 9$ m/s and $\overline{f} = 2.5$ Hz. The value of ρ corresponding to Fig. 5.2 a is the y-intercept and the values of ρ corresponding to Fig. 5.2 b,c are the solid circles on the vertical lines for n = 3 and n = 6.

Figure 5.4 shows theoretical curves which were calculated by equation 4.10 for the '1/4-car' vehicle model from Chapter 4, travelling at 32 km/h for comparison. The vertical lines on the figure again show the design spacings, calculated using eq. 4.22 with $\overline{V} = 9$ m/s and $\overline{f} = 2.5$ Hz.

Several comments can be made about Figures 5.3 and 5.4.

(i) The general shapes and magnitudes of the experimental and theoretical curves are similar. This appears to verify that the 1/4-car model used in the theoretical analysis is a reasonable representation of the dynamics of the steering axle of vehicle S1.

(ii) The main differences between the theoretical and experimental curves are the spacings at which the peaks and troughs occur. This is because the natural frequencies of the test vehicle and the theoretical model are different. The theoretical model had a sprung mass natural frequency of 1.9 Hz (section 4.3.2). The natural frequency of the experimental vehicle can be deduced from Fig 5.3 by considering the location of the first peak, which occurs approximately at $\Delta = 3.2$ m. From eq. 4.8 (and point C on Fig 4.7a), this corresponds to $\delta = 1$.

Using eq. 4.4, the natural frequency of the vehicle is given by

$$f = V/\Delta_1 \tag{5.1}$$

where Δ_1 = sensor spacing corresponding to the first peak in the curve of ρ vs Δ.

In the case of Fig 5.3, $V = 9$ m/s and $\Delta_1 = 3.2$ m, so $f = 9/3.2 = 2.8$ Hz. The second peak in the curves is expected to occur when $\delta = 2$, i.e. $\Delta = 2V/f = 6.4$ m. This agrees with Fig 5.3.

(iii) The spacings given by eq. 4.22 and shown by the vertical lines in Figs 5.3 and 5.4, would be reasonable choices for the array design spacings. The vertical line corresponding to $n = 2$ falls slightly to the right of the first trough in the ρ - Δ curve in Fig 5.3, because the natural frequency of the vehicle is 2.8 Hz, which is slightly greater than the design frequency $\bar{f} = 2.5$ Hz. Conversely in Fig 5.4, the vertical line for $n = 2$ falls to the left of the first trough, since $f = 1.9$ Hz and $\bar{f} = 2.5$ Hz.

(iv) As explained in Chapter 4, arrays with 3 or more sensors are more 'robust' to frequency and speed variations because they have relatively wide, flat-bottomed 'plateau regions' (troughs). This can be seen in both the experimental and theoretical curves (Figs 5.3 and 5.4). As a result, the vertical lines for $n = 3$ to 6 in Figs 5.3 and 5.4 lie at spacings which are appropriate choices to minimise the ECOV $\bar{\rho}$, despite the fact that the operating frequencies are different to the design frequency $\bar{f}$. It can also be seen that a small error in spacing of the 2-sensor system due to, say, a different vehicle speed, would cause a more rapid decrease in accuracy than for the systems with 3 or more sensors.

A graph of ρ vs Δ for the steering axle of S1 at low speed, 9 km/h = 2.5 m/s is provided in Fig. 5.5. (This figure is repeated later as Fig 5.12a.) Theoretical curves for the 1/4-car model travelling at the same speed are provided in Fig 5.6a. There are qualitative similarities between Figs. 5.5 and 5.6a, however the theoretical curves do not display the rapid fluctuation of the experimental curves. Again this is mainly because of the different natural frequencies of the experimental vehicle and the theoretical model (2.8 Hz and 1.9 Hz respectively.) This results in a different wavelength 'over the ground' $\Delta_1 = V/f$. Fig 5.6b shows the result of running the simulation at 1.7 m/s (6.1 km/h) so that

$$\Delta_1 = \frac{V}{f} = \frac{1.7 \text{ m/s}}{1.9 \text{ m/s}} = 0.89 \text{ m.}$$

This is approximately equal to V/f in Fig 5.5:

$$\Delta_1 = \frac{V}{f} = \frac{2.5 \text{ m/s}}{2.8 \text{ m/s}} = 0.89 \text{ m.}$$

Fig 5.6b shows closer similarity to the rapid fluctuation of the experimental curves in Fig 5.5.

It is worth noting that if the sensors were more closely spaced than 0.4 m, (say at 0.2 m or less), then the curves in Figs 5.5 and 5.6b would be considerably smoother, and would resemble Fig. 5.4 but with the crests and troughs packed together with $\Delta_1 = 0.89$ m.

A third comparison between experiment and simulation is provided in Figures 5.7 and 5.8. Figure 5.7 shows a graph of ρ vs Δ for axle 5 (on the trailer) of vehicle S4 travelling at 85 km/h (23.6 m/s). (This figure is repeated later as Fig 5.35c). Fig 5.8 shows theoretical predictions using the 1/4-car model of Chapter 4, with a speed of 85 km/h. From the y-intercept, it can be seen that the DLC is approximately 11.5%.

Notes:

(i) The sprung mass natural frequency of the experimental vehicle can be estimated from the first peak of Fig 5.7 (corresponding to $\delta = 1$) using eq 5.1:

$$f \approx \frac{23.6 \text{ m/s}}{6.0 \text{ m}} = 3.9 \text{ Hz.}$$

This is significantly higher than the array design frequency $\bar{f} = 2.5$ Hz, but is within the expected range of 1.5 to 4.5 Hz discussed in section 4.1.

(ii) As a consequence of (i), the design spacing for n = 2, at approximately 4.7 m in Fig 5.7, is far away from the optimum at approximately 3.0 m. (The latter is the spacing that would have been chosen for n = 2, if it was known beforehand that all vehicles had natural frequencies of 3.9 Hz). The RMS error for n = 2 at the design spacing is approximately 8.8%.

The design spacing for n = 3 (at approximately 4.2 m) is just within the 'plateau region' of the ρ - Δ curve for n = 3. Consequently the RMS error for n = 3 at the design spacing is approximately 5.7%, a substantial improvement over 8.8%, for n = 2. This illustrates the significant benefit, in terms of operating speed and frequency ranges, which is obtained by using a WIM array with 3 or more sensors.

(iii) In Fig 5.8 as in Fig 5.4, the vertical line for n = 2 falls to the left of the trough in the ECOV curve for n = 2. This is because the natural frequency (1.9 Hz) is less than $\bar{f} = 2.5$ Hz.

On first examination of Figs 5.3-5.8, the best sensor spacing for all values of Δ appears to be $\Delta = \bar{V}/2\bar{f}$, which corresponds to the trough in the ρ - Δ curve for n = 2. This spacing is approximately at the centre of the 'plateau region' for all other values of n.

It is important to recall, however, that the design spacing was calculated (in section 4.4.1) so that the array would be accurate over the widest possible speed range. The spacing calculated in this way turns out not to be at the centre of the plateau region of a ρ - Δ graph, but at the centre of the plateau region on a ρ - V graph, as in Fig 4.9a.

The reason for this can be seen by reference to Figs 5.9 and 5.10 which show theoretical ρ - Δ curves for n = 3 and n = 6 respectively. In these graphs, the design spacing was calculated with

$\overline{V}$ = 22.2 m/s (80 km/h) and $\bar{f}$ = 1.9 Hz, the sprung mass natural frequency of the vehicle model. (1.9 Hz was chosen instead of 2.5 Hz to simplify the following explanation).

In Fig 5.9, ρ - Δ curves are shown for V = 60, 80 and 100 km/h, whereas in Fig 5.10, ρ - Δ curves are shown for V = 40, 80, 120 km/h[1].

The 'solid' circles on Figs 5.9 and 5.10 correspond to the theoretical edges of the 'plateau' regions of the curves as defined by $\delta = 1/3, 2/3$ in Fig 5.9 and $\delta = 1/6, 5/6$ in Fig 5.10 (see eq 4.8 and Fig 4.7a).

It can be seen from Fig 5.9 that for n = 3, the design spacing Δ_{design} = 5.2 m falls near to the middle of the plateau in the ρ - Δ curve for V = 80 km/h. This spacing is close to the left hand edge of the plateau ($\delta = 1/3$) of the curve for V = 100 km/h and is close to the right hand edge of the plateau ($\delta = 2/3$) of the curve for V = 60 km/h. Thus Δ_{design} = 5.2 m is a suitable spacing for $60 \leq V \leq 100$ km/h.

A similar argument applies to the curves for n = 6 and V = 40, 80, 120 km/h in Fig 5.10. In this case, however, the design spacing Δ_{design} = 3.3 m falls between $\delta = 1/6$ for V = 120 km/h and $\delta = 5/6$ for V = 40 km/h. Thus Δ_{design} is suitable for speeds of 40 to 120 km/h (in fact, V_{min} = 27 km/h and V_{max} = 133 km/h, using equations 4.20 and 4.21). Had the design spacing been calculated from $\Delta = \overline{V}/2\bar{f}$ = 5.9 m as suggested above (and shown dashed on Fig 5.10), then the array would be inaccurate for speeds less than approximately 50 km/h instead of 40 km/h.

Magnitude of Baseline Sensor Errors

There are two ways to determine the accuracy of individual sensors to measure the applied tyre forces:

(i) Instrument the test axle(s) to measure dynamic tyre forces and relate the tyre force measurements to the sensor outputs (see for example [6-8]);

(ii) Roll a tyre with a known static load slowly over the sensors, so as to minimise dynamic effects.

In this section we will investigate the use of the indirect method (ii) with data collected for an articulated vehicle.

---

[1] Note that with these particular values of $\Delta = \Delta_{design}$, equations 4.20 and 4.21 give expected operating speed ranges of:

V_{min} = 53 km/h and V_{max} = 107 km/h for Fig. 5.9
V_{min} = 27 km/h and V_{max} = 133 km/h for Fig. 5.10.

Assume that the random errors on the output of sensor x have zero mean and standard deviation σ_x. If these errors are statistically independent of (uncorrelated with) the errors σ_y of sensor y, then the variance of the *average* of sensors x and y will be (from the rules governing variances)

$$E\left[\left(\frac{x+y}{2}\right)^2\right] = \sigma_{x/2}^2 + \sigma_{y/2}^2 = \frac{\sigma_x^2}{2^2} + \frac{\sigma_y^2}{2^2}. \tag{5.2}$$

The errors on 2 sensors would be uncorrelated if they were caused by noise or random inaccuracies in signal processing which were not related to the vehicle loading. (Clearly dynamic axle loads do *not* fit into this category).

Assume further that a WIM array consisted of n sensors, each having the same 'baseline' error standard deviation σ_o due to noise and random calibration errors. Then (5.2) would become

$$\sigma(n)^2 = n\frac{\sigma_o^2}{n^2} = \frac{\sigma_o^2}{n}.$$

Hence the array error standard deviation would be

$$\sigma(n) = \sigma_o/\sqrt{n} \tag{5.3}$$

and normalising by the static load P_o, the Error Coefficient of Variation would be

$$\rho(n) = \rho_o/\sqrt{n}, \tag{5.4}$$

where $\rho_o = \sigma_o/P_o$ and $\rho(n) = \sigma(n)/P_o$.

This result was referred to in section 4.4.4 and is a particular case of the central limit theorem.

The ρ - Δ curves shown in Figs 5.12 - 5.47 have error components from four main sources:

(i) Baseline sensor errors σ_o (or ρ_o) due to noise *and* sensor calibration errors.

(ii) Dynamic loads.

(iii) Mean load errors due to uneven load distribution as described in Section 3.3. (This is because the runs in both directions over the mat were averaged together).

(iv) Errors due to tyre tread effects.

In order to use (5.3) or (5.4) to estimate the baseline sensor accuracy σ_o, it is necessary to minimise error sources (ii)-(iv) where possible:

(i) Some dynamic loads are present even for low speeds. They are caused by road roughness and also by drive torque fluctuations due to small speed variations. The smallest dynamic loads usually occur on the steering axle of articulated vehicles, since this has a small static load and (usually) a relatively soft and well damped suspension. Furthermore, it is likely that the air suspended tractor on vehicle S4 would have the least sprung mass motion, and hence least dynamic steering axle loads at low speeds.

(ii) In order to remove the mean load errors described in (iii) above it is necessary to plot a ρ - Δ curve for the vehicle travelling in one direction only.

(iii) Sensor errors due to tyre tread effects cannot be eliminated, however they are expected to be small for 'highway' tread tyres, as per the steering axle of S4. (Tyre tread effects are discussed in section 5.4.3).

Figure 5.11 is a ρ - Δ graph for the steering axle of vehicle S4 at a speed of 11 km/h. If the errors shown on this graph were due to baseline sensor errors only (ρ_o), then the ECOV lines would be horizontal (i.e. independent of sensor spacing) with values given by eq. 5.4 Furthermore, the y-axis intercept, which corresponds to the ECOV of the individual sensors $\rho(1)$, would be equal to ρ_o.

Plotted over the top of the ρ - Δ curves are dashed lines at levels $\rho(1)$, $\rho(1)/\sqrt{2}$, $\rho(1)/\sqrt{3}$, ... $\rho(1)/\sqrt{6}$. It can be seen that these horizontal lines are quite good fits to the appropriate ρ - Δ curves, thus verifying that in this case the dynamic loads are relatively small and that the errors largely support the theory behind eq. 5.4. Note that this exercise does not work for any of the other low speed steering axle ρ - Δ curves because they all contain a significant error component due to dynamic loads. It is concluded, therefore, that the average baseline error of all of the sensors in the mat is approximately

$$\rho_o \approx \rho(1) = 4\ \%.$$

This is the coefficient of variation of the error which is expected, on average, for any individual dynamic wheel force measurement by a capacitative strip sensor in the mat. This is an important result because it provides an estimate of the baseline sensor accuracy, which was one of the main objectives of the project. The value of 4% is comparable with the 3% to 5% established in previous experiments on a few sensors in the prototype load measuring mat in the UK [8].

The baseline sensor error is expected to increase slightly at higher speeds due to rounding errors in the signal processing system (see Appendix A, section 3.3.1). Conversely, ρ_o will decrease as the static axle loads are increased, for the same reason. (Note that the steering axle of vehicle S4 is relatively lightly loaded, at 25.6 kN per tyre, compared with 35-40 kN per tyre on most 'load carrying' axles in the USA.)

Discussions of Results for Six Articulated Vehicles

The ρ - Δ curves for all of the test runs on the six articulated vehicles (460 runs total) are provided in Figs 5.12 - 5.47. For each vehicle, the data for six nominal testing speeds (5, 10, 20, 30, 40, 50 mph) are presented, one speed per page.

For each speed, ρ - Δ curves are presented for axles 1, 3 and 5: the tractor steer axle, second tractor drive axle and second trailer axle respectively. Each graph also shows the design sensor spacings calculated from equation 4.22 with $\bar{f} = 2.5$ Hz and with $\bar{V}$ equal to the average testing speed in each case.

These figures contain a large amount of information: each graph summarises the results of approximately 70 000 separate WIM array averages! A number of deductions can be made about the static and dynamic loads generated by the vehicles and the design of WIM arrays.

The first and most important observation is that not all of the graphs have the same characteristic form as the theoretical predictions in Figs 5.4, 5.6b and 5.8, presented previously.

There are four reasons for this:

(i) The baseline sensor errors (ρ_o).

(ii) Uneven loading of the test vehicle (section 3.3)

(iii) Tyre tread effects

(iv) Inaccuracies in the theoretical vehicle model.

These issues are discussed in detail in the following paragraphs.

Influence of Sensor Errors

The baseline sensor errors ρ_o, will cause a constant offset in the ρ - Δ curves independent of the vehicle speed or sensor spacing. At low speeds it is possible for the small dynamic loading effects to be swamped by the baseline sensor errors ρ_o.

If the error coefficient of variation for n-sensors due to dynamic loading alone is $\rho_d(n)$ then using similar reasoning to eq. 5.2, the overall ECOV due to ρ_o and $\rho_d(n)$ combined will be

$$\rho = \sqrt{\frac{\rho_o^2}{n} + \rho_d^2(n)} \qquad (5.5)$$

where

$\rho_o \approx 0.04 \qquad (4\%)$.

If $\rho_d(n) << \rho_o/\sqrt{n}$, then ρ will be dominated by the baseline sensor errors ρ_o. Conversely, if $\rho_d(n) >> \rho_o/\sqrt{n}$, then ρ will be dominated by the dynamic loading effects, ρ_d.

In the cases where ρ_o dominates, the ρ - Δ curves will show a sudden reduction in ρ between $\Delta = 0$ and $\Delta = 0.4$ m [2]. This effect can be seen in Fig 5.11 and in most of the other low speed ρ - Δ curves for the steering axles, e.g. Figs 5.18a, 5.24a etc. It can also be seen in some of the low speed ρ - Δ curves for axle 3, e.g. Figs 5.12b and 5.18b.

Uneven Static Loading of the Test Vehicles

The procedure used in this study to calculate the ρ - Δ curves (described in section 5.1) incorporated the data for both directions of vehicle motion over the mat. This means that the results for both the nearside and offside tyres were included in the averages. This was considered to be the most practical way to combine all of the test data, without generating twice as many figures.

The procedure has the drawback that static load differences, between the two tyres on an axle, appear as WIM system errors. An example of this effect can be seen in Fig 5.12c which shows quite large errors of approximately 8-10%, for a 6-sensor system at low speed. However, examination of Fig 3.2e (which corresponds to the same axle), shows that the difference between the static loads on the tyres at either end of the axle is approximately 17%. This difference will cause substantial spreading of the probability distribution, and hence an apparently large ECOV. The same problem causes large ECOV values in all of the cases where the vehicle is unevenly loaded: axles 3 and 5 of vehicles S1 and S2; axle 3 of S3 and S4, axles 3 and 5 of S5 and S6 (these were deduced from Figs 3.2-3.7).

This problem would *not* occur in practice, providing the WIM sensors extended across the road and measured the loads generated by both sides of the vehicle. With such an arrangement the uneven loading errors would cancel out.

It is possible that an alternative data analysis procedure could be developed in order to remove the problem. This possibility is being considered at present and may be adopted in the final project report.

Tyre Tread Effects

All of the tyres on the test vehicles had 'highway' tread patterns, except for the drive axles of the air suspended tractor (Vehicle S4), which had off-road tyres.

The contact pressure distribution under a rolling tyre depends on the tread pattern. Off-road tyres can have quite large local contact pressure variations in the vicinity of the individual tread elements. When such a tyre rolls over the mat, some of the strip transducers will come into contact with high-

---

[2] $\Delta = 0$ corresponds to a 'single-sensor' WIM average and $\Delta = 0.4$ m corresponds to the spacing between adjacent sensors in the mat and hence is the smallest Δ for which experimental WIM averages can be calculated for the mat.

pressure regions of the tyre contact area and others will come into contact with low-pressure regions.

The wheel force measurement involves integrating the output of each strip sensor (which is proportional to the local contact pressure) throughout the period of contact between tyre and sensor. Thus if some sensors experience a high contact pressure, they will register an abnormally high load. Conversely some sensors will register an abnormally low load.

This problem is dependent on the construction of the tyre and the tread pattern. It is expected to occur for *any* type of narrow strip WIM transducers, not just capacitative strips. Thus it can be considered to be a fundamental limit on the accuracy of strip sensors. Fortunately the majority of highway vehicles use 'highway' tread (rib) tyres and these do not display a significant variation of local contact pressure due to the tread elements. Thus for most vehicles, tyre tread effects are not likely to cause serious errors with strip WIM sensors.

A graphic example of the tyre tread effect can be seen for axle 3 on vehicle S4 (see Figs 5.30b to 5.35b). Because of the air suspension, this vehicle is expected to produce relatively small dynamic loads. Figure 5.30b, however, shows a large Error Coefficient of Variation $\rho(1)$ of approximately 16% at $\Delta = 0$, for a speed of 11 km/h ($\rho(1)$ = y-intercept of the ρ - Δ curves = the Dynamic Load Coefficient, from section 4.2.3). This was one of the largest ECOVs measured in all of the tests! It is interesting to note that the $\rho(1)$ value for axle 3 of S4 remains approximately constant with speed, indicating that it is not influenced by the dynamics of the vehicle. For every other axle, there is a significant increase in $\rho(1)$ with speed.

The first peak in Fig 5.30b occurs at $\Delta_1 = 2.0$ m. If this peak was caused by dynamic loads, it would shift with speed. For example, if the speed increased from 11 km/h to 85 km/h as in Fig 5.35b, Δ_1 would be expected to increase to

$$\Delta_1 = 2.0 \times \frac{85 \text{ km/h}}{11 \text{ km/h}} = 15.5 \text{ m.}$$

This clearly does not occur. In fact the position of the first peak stays relatively constant for speeds up to 51 km/h (Fig 5.33b). It then decreases slightly with higher speeds, to $\Delta_1 = 1.8$ m in Fig 5.35b.

The explanation of this behaviour is related to the tyre tread pattern as follows:

Suppose the variation in normal contact pressure in the contact area has a sinusoidal component with amplitude P and wavelength λ along the direction of motion as shown conceptually in Fig. 5.48a. For typical off-road tyres, λ is likely to be approximately 75-100 mm. If distance measured along the direction of motion is x, then as the tyre rolls along the road, the *peak* pressure p(x) experienced at a point x will be approximately

$$p(x) = P_o + P\cos\left(\frac{2\pi x}{\lambda} + \phi\right). \tag{5.6}$$

Following the notation of chapter 4 we can define the pressure error $\varepsilon(x)$ by

$$\varepsilon(x) = \frac{p(x) - P_o}{P} \qquad (5.7)$$

hence

$$\varepsilon(x) = \cos(\frac{2\pi x}{\lambda} + \phi). \qquad (5.8)$$

The phase ϕ is unknown and for the purpose of this discussion it can be set to zero without loss of generality. (Alternatively, the procedure used in section 4.2.1 could be used to obtain the envelope error etc.)

Suppose that there are exactly k cycles of wavelength λ in $\Delta_1 = 2.0$m (2 m = 5 sensor spaces, each of distance L = 0.4 m). Then

$$k\lambda = 2.0 \text{ m}. \qquad (5.9)$$

If k is a prime number, then the maximum contact pressure can only coincide with the location of a sensor every k cycles, which will correspond to 2.0 m (or 5 sensors). For example, assume k = 19 so that $\lambda = 0.105$ m. Then $\varepsilon(x)$ will take the form shown in Fig 5.48b. This is an example of under-sampling or aliasing. The sensor array cannot distinguish between a pressure component with wavelength 0.105 mm and a pressure component with wavelength 2.0 m.

The wavelength λ is dependent only on the tread pattern and so the aliased wavelength of 2.0 m is largely independent of speed. Note, however, that for high vehicle speeds the driving torque and hence longitudinal 'creep' or 'slip' of the driven wheels becomes significant. This causes an effective reduction in λ and the aliased wavelength decreases from 2.0 m to 1.8 m in Fig. 5.35 b.

A second example of the effects of tyres can be observed on measurements of the trailer axles of vehicles S1 and S2. The tyres on this trailer had bad flat spots (due to previous braking tests) as noted in Appendix B. The result was a periodic component of wheel force with a wavelength of approximately 3 m, which corresponds to the circumference of the tyres. This causes peaks in the ρ - Δ curves at $\Delta \approx 3,6,9$ m in Figs. 5.12c - 5.23c. The positions of these peaks do not change with speed (as expected), however at some speeds, additional peaks occur, in between, due to dynamic loads.

An interesting effect can be observed in Figs 5.19, where it appears that a 3 Hz pitching vibration mode, involving both the tractor and trailer was excited by the radial run-out of the trailer tyres. All axles on the vehicle displayed the same resonant frequency, which, at 17 km/h, corresponds to exactly twice the trailer wheel rotation frequency. This same resonant mode is also excited at 34 km/h (Fig 5.20), when the wheel rotation frequency coincides with the natural frequency at 3 Hz.

Inaccuracies in the Theoretical Model

One of the sources of inaccuracy in the theoretical WIM predictions in chapter 4 is the over simplicity of the vehicle models used in the analysis. As noted in section 4.3.2, these models were not intended to contain the detailed suspension nonlinearities and complexities of sprung mass motion that are typical of heavy vehicles. They were intended to be broadly representative of the two main classes of heavy vehicle suspensions.

There are three main differences between the theoretical models and the experimental results:

(i) Not all of Figs. 5.12-5.47 display the distinct peaks and troughs predicted by the theoretical calculations. Apart from the sensor baseline errors and tyre effects, discussed previously, the main factor associated with vehicle dynamics is thought to be the presence of dry friction in the leaf spring suspensions. This modifies the dynamic behaviour of the vehicle significantly, particularly near resonance, for low levels of excitation (low speeds on a relatively smooth road surface). One likely consequence is 'smearing-out' of the main sprung mass spectral peak (see, for example, [23]).

(ii) The 'natural frequencies' of the test vehicles have been estimated from the ρ - Δ curves, using measured values of Δ_1 and eq. 5.1. They are listed in Table 5.1 for all of the cases in which a distinct natural frequency can be deduced from the graphs. The two cases excluded from the analysis were the tractor axles of vehicle S4, which had the off-road tyres (see section 5.4.3); and the trailer axles of vehicle 53, which had the pivoted spring ('single-point') suspension. The latter case is discussed separately in the next section.

The frequencies in Table 5.1 range from 2.4 Hz to 4.4 Hz. They are all greater than the 'sprung mass' natural frequency of the 1/4-car model (1.9 Hz)[3]. It appears from Table 5.1 that for the North American vehicles tested in this study, a better value of $\bar{f}$ for WIM array design purposes would be approximately 3 Hz.

Most articulated vehicles have more than one resonant sprung mass mode of vibration in the 1.5-4.5 Hz range. The relative levels of vibration in these modes are dependent on the speed, because of the input road roughness, and 'wheelbase filtering' effects [14,24]. Thus the apparent 'natural frequency' of the vehicle (as measured from the ρ - Δ curves) can change with speed.

One example of this can be seen in Figures 5.33c to 5.35c, where the dominant frequency of axle 5, vehicle S4 appears to change from 4.4 Hz in Fig 5.33c to 3.9 Hz in Figs 5.34c and 5.35c. Several other examples of this effect can be seen in the frequency data in Table 5.1.

---

[3] The theoretical calculations in Chapter 4 were performed three months *before* the experiments, when the characteristics of the test vehicles were not known.

(iii) An unusual effect can be seen in the ρ - Δ curves for the trailer axles of vehicles S4, S5 and S6 (see Figs 5.30c-5.33c, 5.36c-5.40c, 5.42c-5.46c). In these curves, the WIM errors appear to improve (almost monotonically) with increasing sensor spacing. This behaviour is not predicted by the theory. It is important to realise that the same trailer was used on vehicles S4, S5 and S6 and is responsible for the unusual behaviour in each of these figures. This trailer was identified in Section 3.3 as showing strange load sharing between the axles in the tandem suspension, due to some sort of suspension misalignment.

It can only be speculated that very low frequency weight re-distribution occurs as this vehicle travels over the mat. This weight transfer is a quasi-static effect which does not change with vehicle speed and appears to be related to the suspension misalignment. It seems likely that it is caused by the transverse road roughness (camber) in the mat test section.

Pivoted Spring Suspension

It is clear from Figs 5.24c to 5.29c that large dynamic loads are generated by the pivoted spring ('single point') suspension on the trailer of vehicle S3, with $\rho(1)$ (DLC) values of 13% to 18%.

Previous work [9,13] has shown that such suspensions can display lightly damped bogie pitching motion at 8-15 Hz. However the motion is not usually as lightly damped as walking-beam suspensions, because of dry friction at the spring 'slipper' ends which dissipates some energy [13].

Figures 5.24c to 5.29c are difficult to interpret for two main reasons:

(i) Aliasing

At low speeds the bogie pitching motion is undersampled (aliased) by the mat. (This is analogous to the tyre tread aliasing discussed in section 5.4.3).

The frequency at which the dynamic loads are sampled by the sensors is

$$f_{samp} = V/L$$

where

V = speed (m/s)
L = spacing between adjacent sensors in the mat = 0.4 m.

The highest frequency dynamic force component which can be resolved from the sampled data is known as the Nyquist frequency f_c and is half of the sampling frequency:

$$f_c = V/2L \qquad (5.10)$$

At low speeds, this can be quite a low frequency, for example at 2.4 m/s (8.5 km/h) as in Fig. 5.24, it corresponds to 2.9 Hz. Any force component with a frequency higher than f_c will *appear* to have a frequency lower than f_c (much as shown in Fig 5.48b).

It turns out that if a force component appears at measured frequency f_m then it could be due to a force component aliased from any one of the frequencies [25]:

$$f_{aliased} = 2f_c \pm f_m,\quad 4f_c \pm f_m,\quad 6f_c \pm f_m \ldots\ldots \tag{5.11}$$

Table 5.2 provides a summary of the speeds and estimated natural frequencies for the trailer axles of vehicle S3 (Figs 5.24c-5.29c). Where possible, equation 5.1 was used to estimate the predominant frequency component using values of Δ_1 from the ρ - Δ curves.

From the first two rows of the table, it can be seen that for the lower speeds, the Nyquist frequency is considerably less than the expected natural frequency in the 8-15 Hz range. The column of 'possible aliased frequencies' indicates that the bogie pitch frequency is likely to be 13.2 or 13.5 Hz (as shown in **bold** in the table). These are approximately in agreement with the 13.6 Hz measured from Fig 5.29c and listed in the last row of the table.

(ii) Mat-crossing frequency

As explained in the Introduction (Chapter 1), the mat was made from 'tiles' of size 1.2 m x 1.2 m (4' x 4'). The tiles were fitted end-to-end with 'lap joints' between tiles which were not perfectly smooth and caused *small* periodic inputs to the vehicles at a frequency of

$$f_{mat\text{-}crossing} = V/3L = V/1.2. \tag{5.12}$$

The last column of Table 5.2 lists the mat-crossing frequency and it can be seen that this is exactly the frequency that was measured from the ρ - Δ curves for vehicle speeds of 13.0 m/s and 17.1 m/s.

For most vehicles and highway speeds, the mat-crossing frequency is considerably higher than the predominant resonances in the dynamic tyre forces. Hence the small roughness caused by the joints between tiles is unimportant. For the pivoted-spring suspension at 13 m/s and 17 m/s, the additional excitation at the mat-crossing frequency is amplified by the suspension transfer function and causes measurable dynamic loads.

This fact may be important in establishing a standard vehicle testing procedure using a load measuring mat. Care should be taken in the mat mounting procedure to ensure that the roughness caused by the joints is minimised. Alternatively, vehicles should be tested at speeds where the mat-crossing frequency is substantially higher or lower than the tandem bogie pitch frequency.

It is worth noting that the design sensor spacings shown in Figs 5.24c-5.29c would generally be acceptable choices for this vehicle, as anticipated in section 4.4.3. It would not be worthwhile designing the WIM array specifically for the pivoted-spring or walking-beam suspensions because this would spoil the performance for the majority of vehicles which generate low frequency dynamic loads (see section 4.4.3).

Design Sensor Spacings - Summary

In this Chapter we have examined the main differences between the theoretical predictions of multiple-sensor WIM system performance and the experimental results from the mat.

Overall, it can be seen that the theoretical predictions are reasonably accurate and that the design sensor spacings given by eq. 4.22 are quite a good choice for the vehicles examined. (The main exception is for off-road tyres.) It should be noted, however, that an average frequency of 3 Hz is likely to be more appropriate for US vehicles than the 2.5 Hz recommended in Chapter 4.

The conclusion that an installation with three or more sensors is superior to a 2-sensor array, because of the improved 'robustness' to speed and frequency variations, holds true for the experimental data. Indeed, the design spacing for the 3-sensor systems in Figs 5.12 - 5.47 is almost always within the 'plateau region' of the ρ - Δ curves, despite the fact that $\bar{f}$ was chosen to be slightly too low. This is in contrast with the ρ - Δ curves for $n = 2$, where the design spacing is *never* at the bottom of the ρ - Δ troughs!

Conclusions

(i) The capacitative strip sensors were found to have baseline random errors of approximately 4% RMS for a 26 kN steering tyre load.

(ii) The capacitative strip sensors were found to give large systematic errors, with a coefficient of variation of approximately 16%, when traversed by tyres with an off-road tread pattern.

This effect is expected to occur for *any* type of WIM sensor that is narrower than the tyre contact length when traversed by such tyres. *It is a fundamental limitation of strip WIM sensor technology.* The effect will depend on the details of the tyre tread pattern. It is not a serious source of errors for the majority of tyres with conventional highway tread profiles.

(iii) The experimental results were found to agree quite closely with the theoretical predictions of WIM system performance in Chapter 4. The main discrepancy was due to the higher natural frequencies in the experimental tyre forces than generated by the theoretical vehicle model.

(iv) The WIM array design equation (4.22) was found to yield a good choice for the sensor spacing in a multiple-sensor WIM system.

(v) The average 'sprung mass' frequency $\bar{f}$ of the 6 vehicles tested in this study is approximately 3 Hz. This would probably be an appropriate frequency to use in eq. 4.22 for US vehicles.

(vi) The experimental results verify the conclusion that arrays with 3 or more sensors are likely to have better performance than 2-sensor arrays, because of their robustness to speed and frequency variations.

Table 5.1 Natural Frequencies Deduced From Experimental ρ-Δ curves (Figs. 5.12 - 5.47)

Figure Number	Speed (m/s)	Vehicle Code	Axle Number	Frequency (Hz)
5.13a	4.2	S1	1	2.6
5.14a	9.0	S1	1	2.8
5.16a	16.9	S1	1	2.8
5.15a	13.1	S1	1	3.3
5.15b	13.1	S1	3	4.1
5.19a	4.7	S2	1	3.0
5.19b	4.7	S2	3	3.0
5.20b	9.4	S2	3	3.0
5.23b	23.1	S2	3	3.0
5.21b	14.0	S2	3	4.3
5.19c	4.7	S2	5	3.0
5.20c	9.4	S2	5	3.0
5.23c	23.1	S2	5	3.0
5.26a	9.2	S3	1	2.9
5.29a	21.7	S3	1	3.2
5.28a	17.2	S3	1	3.4
5.27a	13.1	S3	1	3.9
5.26b	9.2	S3	3	2.9
5.29b	21.7	S3	3	3.2
5.28a	17.2	S3	3	3.4
5.33a	14.2	S4	1	2.4
5.34a	18.6	S4	1	2.6
5.35a	23.6	S4	1	2.6
5.34c	18.6	S4	5	3.9
5.35c	23.6	S4	5	3.9
5.33c	14.2	S4	5	4.4
5.38b	9.6	S5	3	3.0
5.41b	23.1	S5	3	3.2
5.39b	13.6	S5	3	3.4
5.41c	23.1	S5	5	3.7
5.39c	13.6	S5	5	4.3
5.46a	17.2	S6	1	2.7
5.44a	9.2	S6	1	2.9
5.45b	13.1	S6	3	4.1
5.46b	17.2	S6	3	4.3
5.47c	21.9	S6	5	3.7
5.45c	13.1	S6	5	4.1
5.46c	17.2	S6	5	4.3

Table 5.2 Frequencies in ρ - Δ curves for pivoted-spring suspension on vehicle S3.

Figure	Speed V (m/s)	Measured Freq^1 f_m (Hz)	Nyquist Freq^2 f_c (Hz)	Possible Aliased Frequencies^3 $f_{aliased}$ (Hz)			Mat Crossing^4 Freq (Hz)
5.24c	2.4	1.7	2.9	4.2, 7.6	10.1, **13.5**	15.9, 19.3	2.0
5.25c	3.5	4.4	4.4	4.4, **13.2**	**13.2**, 22.0		2.9
5.26c	9.1	?	11.4	?			7.6
5.27c	13.0	10.8	16.3	Not aliased			**10.8**
5.28c	17.1	14.3	21.4	Not aliased			**14.3**
5.29c	21.8	**13.6**	27.2	Not aliased			18.2

Notes:

1 Frequency measured from figures using eq. 5.1, $f_m = V/\Delta_1$

2. $f_c = V/2L$, $L = 0.4$ m (eq. 5.10)

3. $f_{aliased} = 2f_c \pm f_m$, $4f_c \pm f_m$, $6f_c \pm f_m$ (eq. 5.11)

4. $f_{mat\text{-}crossing} = V/1.2$ (eq. 5.12)

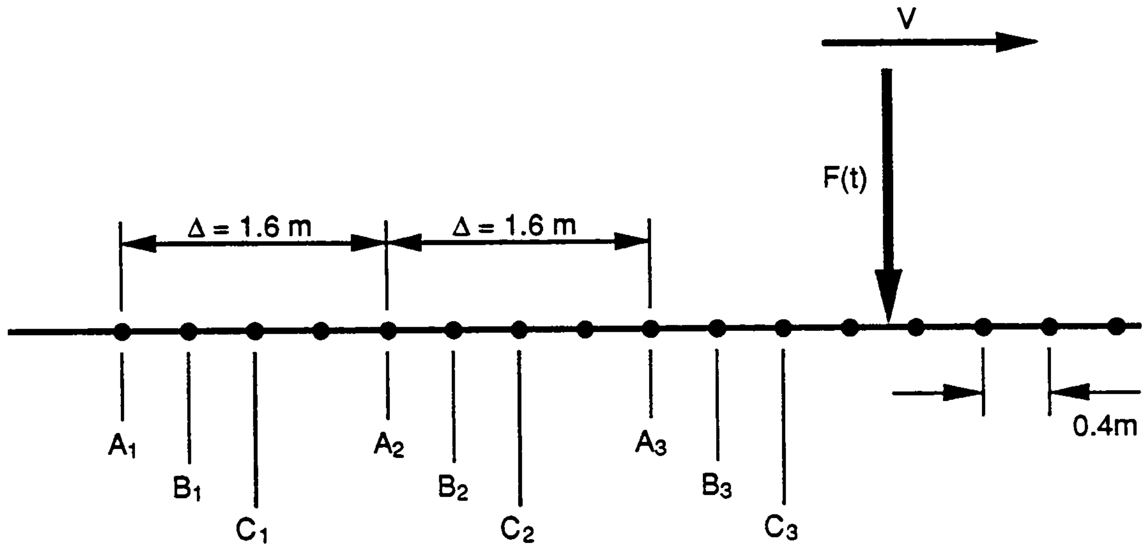

$$\bar{F}_A = \frac{F_{A_1} + F_{A_2} + F_{A_3}}{3} = \frac{1}{n}\sum_{i=1}^{n} F_{A_i}, \qquad \bar{F}_B = \frac{1}{n}\sum_{i=1}^{n} F_{B_i}, \qquad \bar{F}_C = \frac{1}{n}\sum_{i=1}^{n} F_{C_i}$$

Fig. 5.1 Showing the calculation of 3-sensor WIM averages at a spacing of $\Delta = 4 \times 0.4 = 1.6$ m.

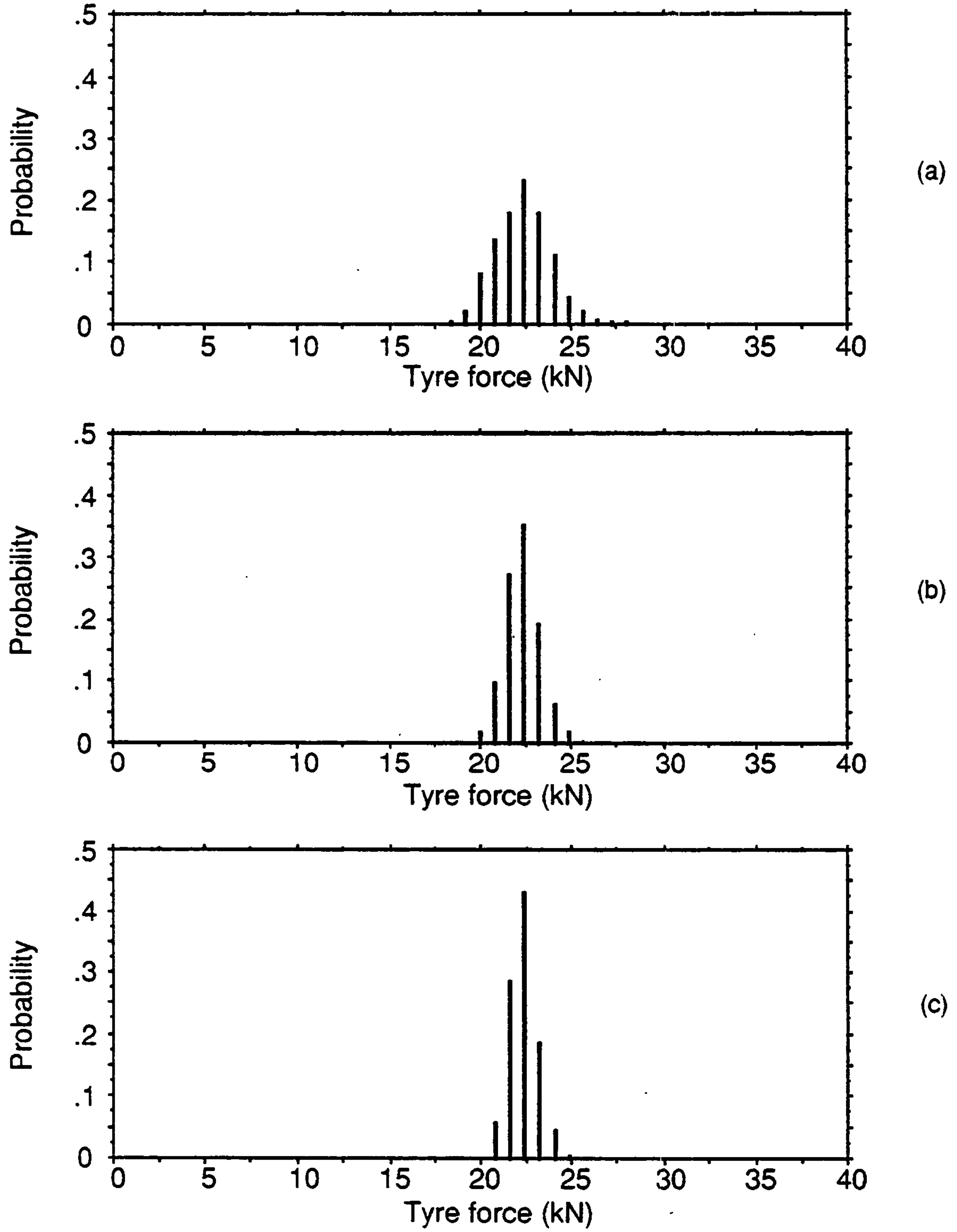

Fig. 5.2 Histograms of WIM average force,
Vehicle S1, Steering axle, Speed = 9 m/s (32 km/h).
(a) single sensor (b) 3 sensors, Δ = 1.6 m (c) 6 sensors, Δ = 0.8 m.

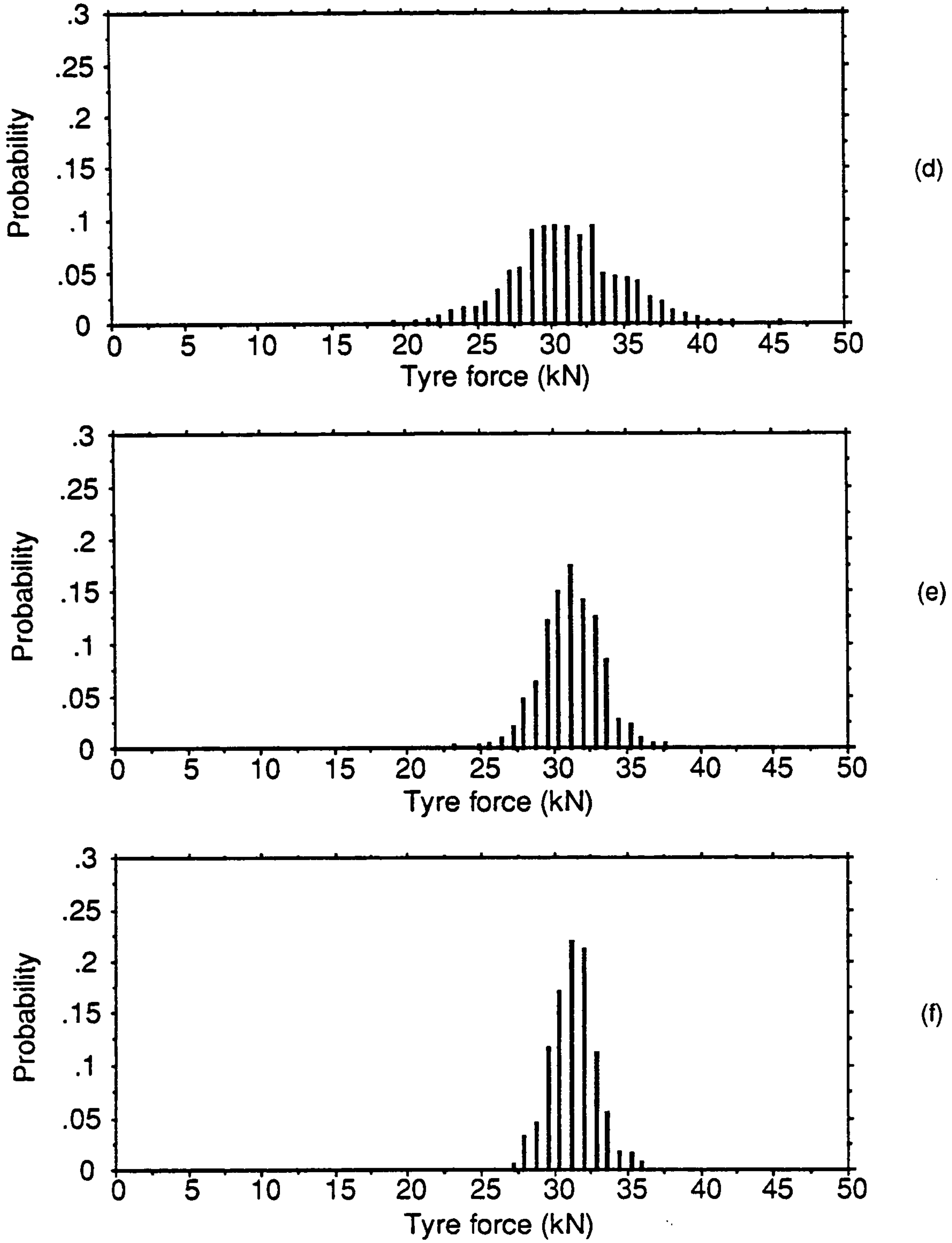

Fig. 5.2 Histograms of WIM average force,
Vehicle S4, Axle 5, Speed = 23.7 m/s (85 km/h).
(d) single sensor (e) 3 sensors, Δ = 4.0 m (f) 6 sensors, Δ = 2.4 m.

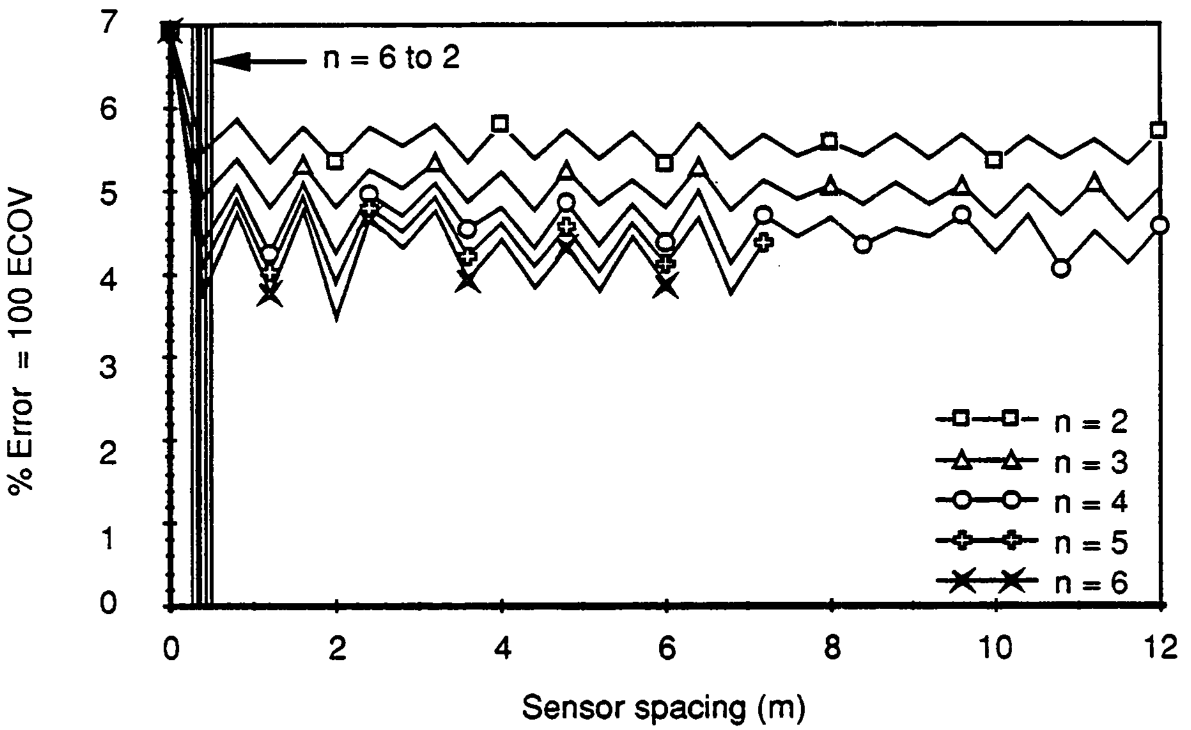

Fig. 5.5 Experimental WIM array Error Coefficient of Variation ρ vs sensor spacing Δ, vehicle S1, speed 9 km/h, steer axle.
Vertical lines denote design spacings according to eq. 4.22.

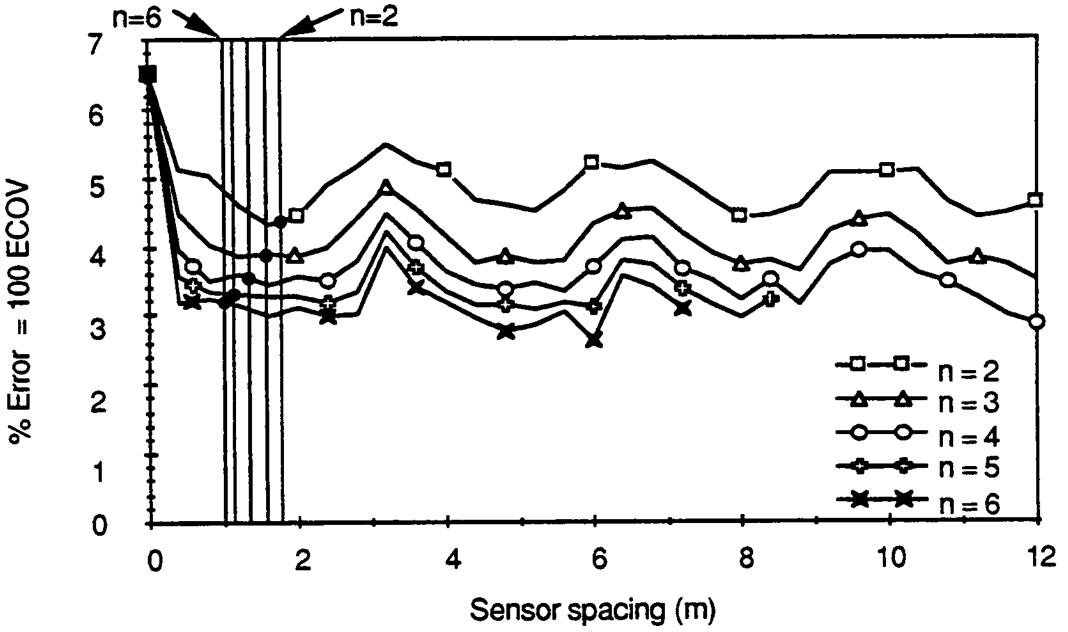

Fig. 5.3 Experimental WIM array Error Coefficient of Variation ρ vs sensor spacing Δ, Vehicle S1, speed 32 km/h, steer axle. Vertical lines denote design spacings according to eq 4.22.

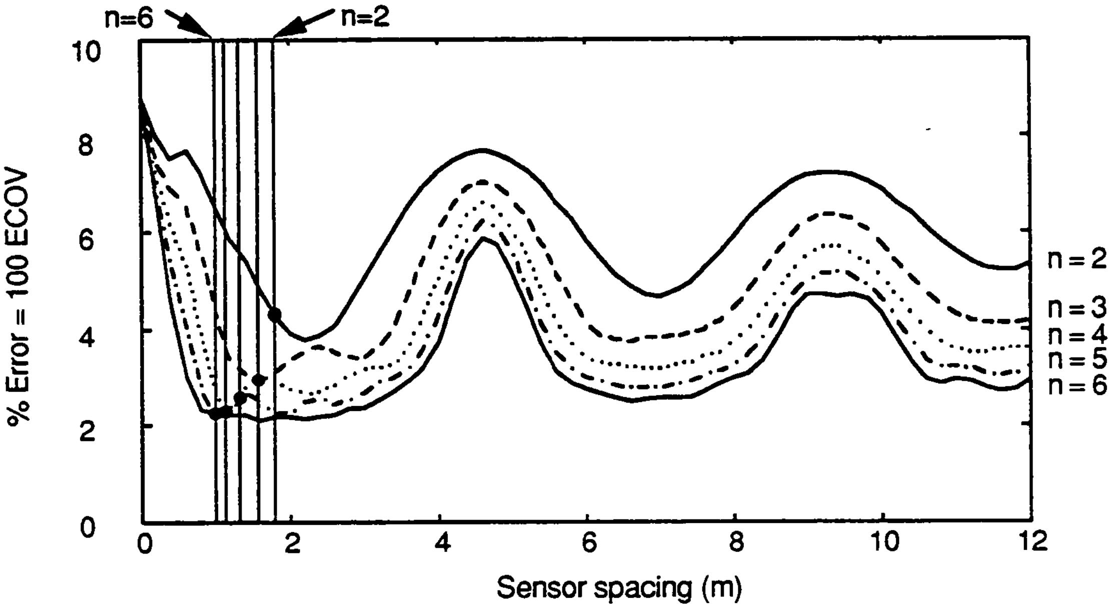

Fig. 5.4 Theoretical WIM array Error Coefficient of Variation ρ vs sensor spacing Δ '1/4-car' model (natural frequency = 1.9 Hz), speed = 32 km/h. Vertical lines denote design spacings according to eq 4.22.

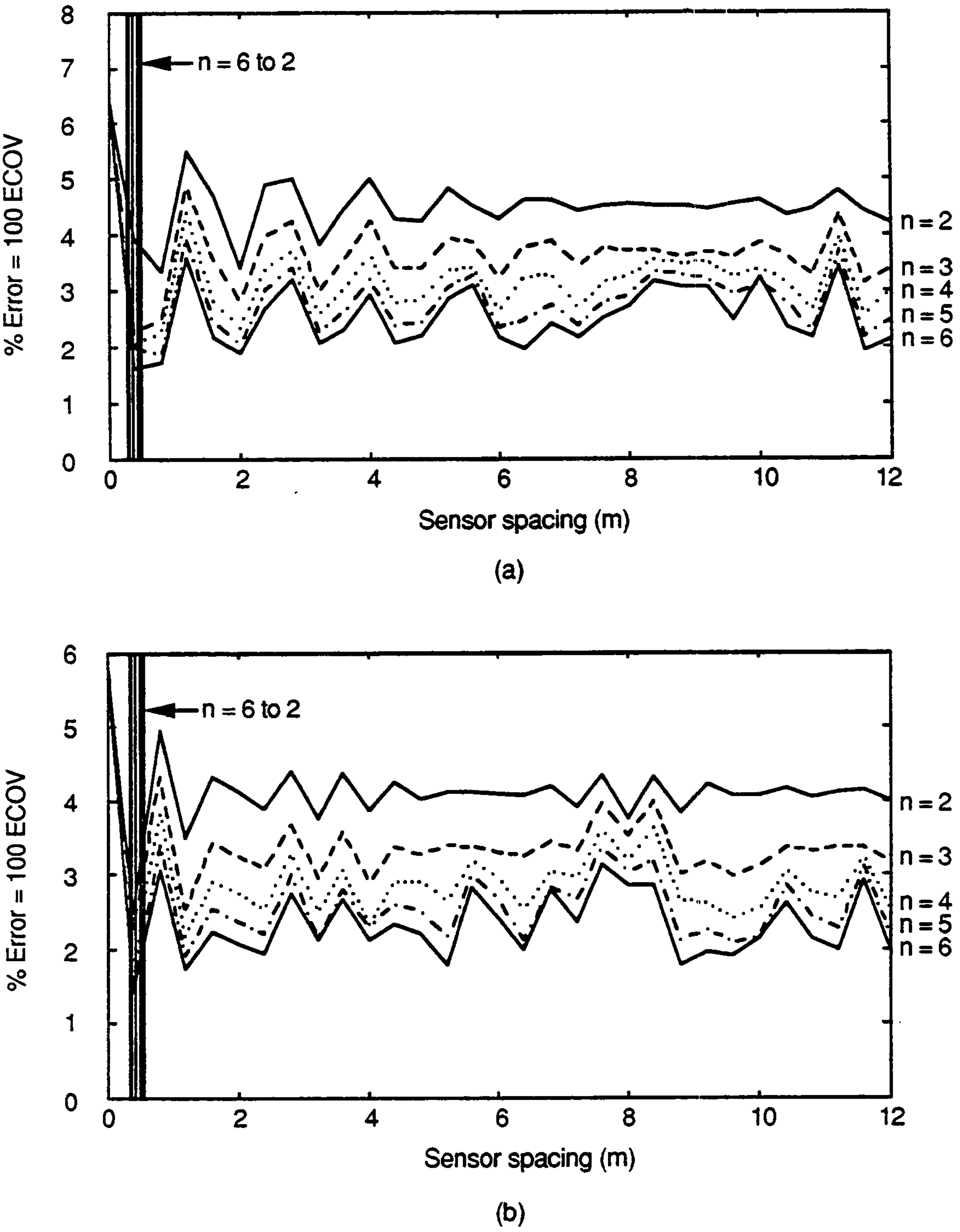

Fig. 5.6 Theoretical WIM array Error Coefficient of Variation ρ vs sensor spacing Δ
'1/4-car' model (natural frequency = 1.9 Hz.)
Vertical lines denote design spacings according to eq 4.22.
(a) speed = 9 km/h (b) speed = 6.1 km/h.

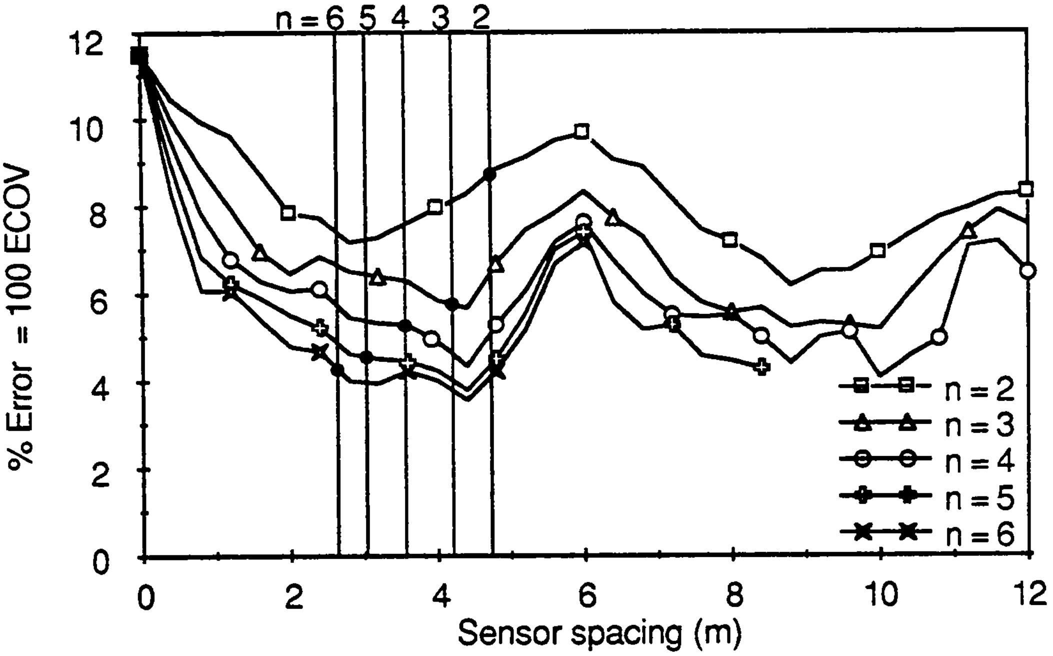

Fig. 5.7 Experimental WIM Error Coefficient of Variation ρ vs sensor spacing Δ, vehicle S4, speed 85 km/h, axle 5 (on trailer). Vertical lines denote design spacings according to eq 4.22.

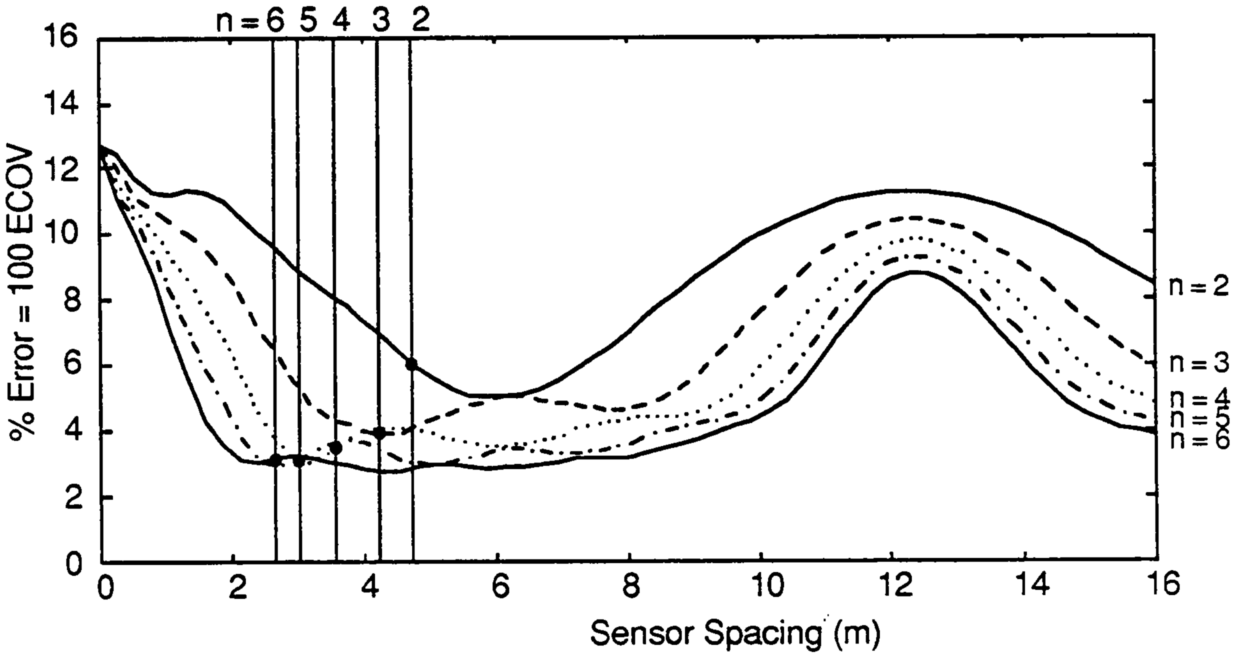

Fig. 5.8 Theoretical WIM array Error Coefficient of Variation ρ vs sensor spacing Δ, 1/4-car model, speed = 85 km/h. Vertical lines denote design spacings according to eq 4.22.

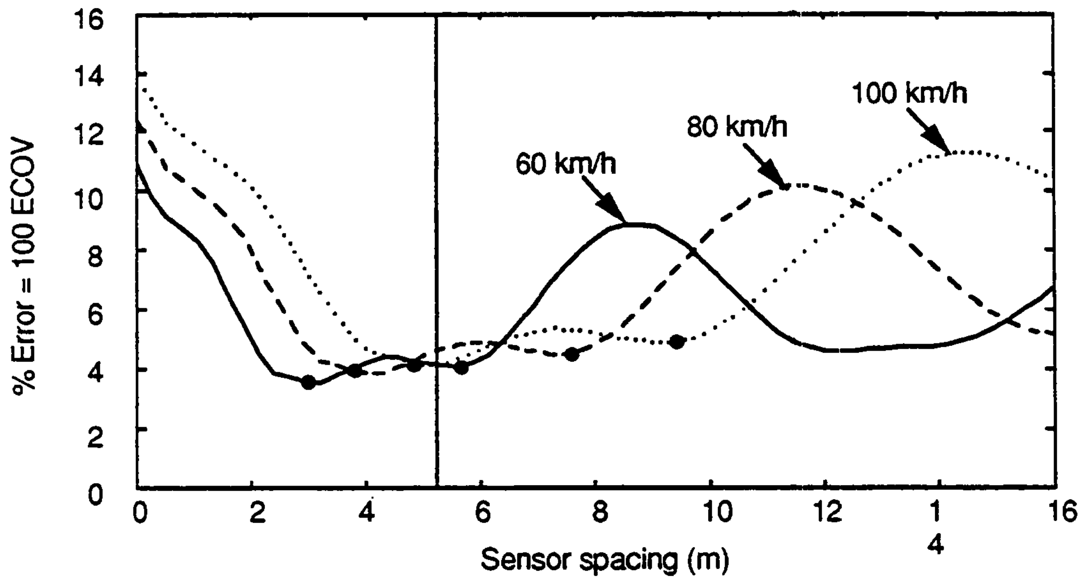

Fig. 5.9 Theoretical graph of ρ vs Δ, for n = 3 and speeds of 60, 80 and 100 km/h. The design spacing was calculated using an average speed of 80 km/h and an average frequency of 1.9 Hz.

The 'solid' circles on each curve correspond to δ = 1/3 and δ = 2/3.

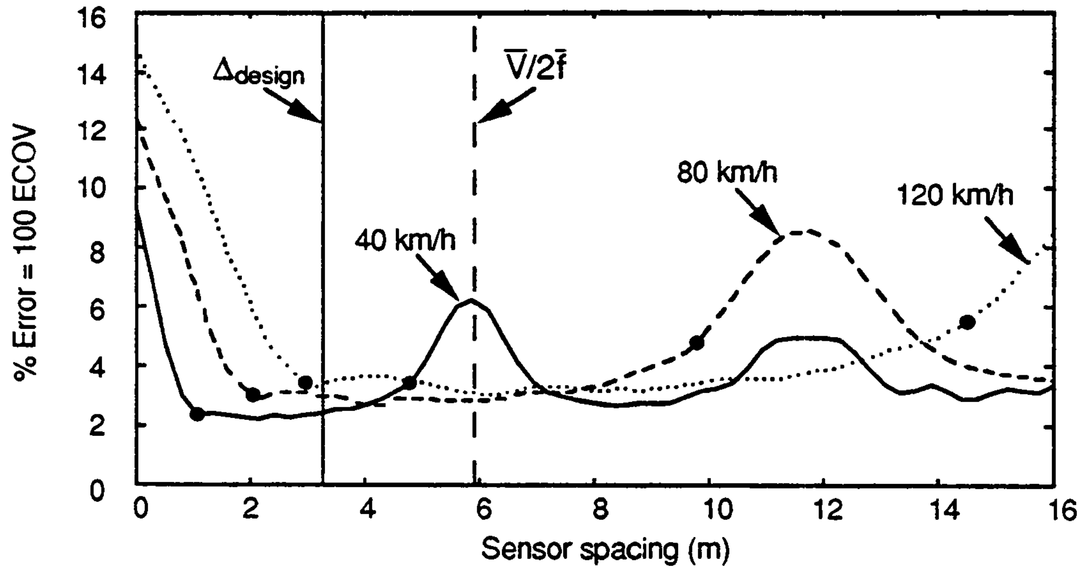

Fig. 5.10 Theoretical graph of ρ vs Δ, for n = 6 and speeds of 40, 80 and 120 km/h. The design spacing was calculated using an average speed of 80 km/h and an average frequency of 1.9 Hz.

The 'solid' circles on each curve correspond to δ = 1/6 and δ = 5/6.

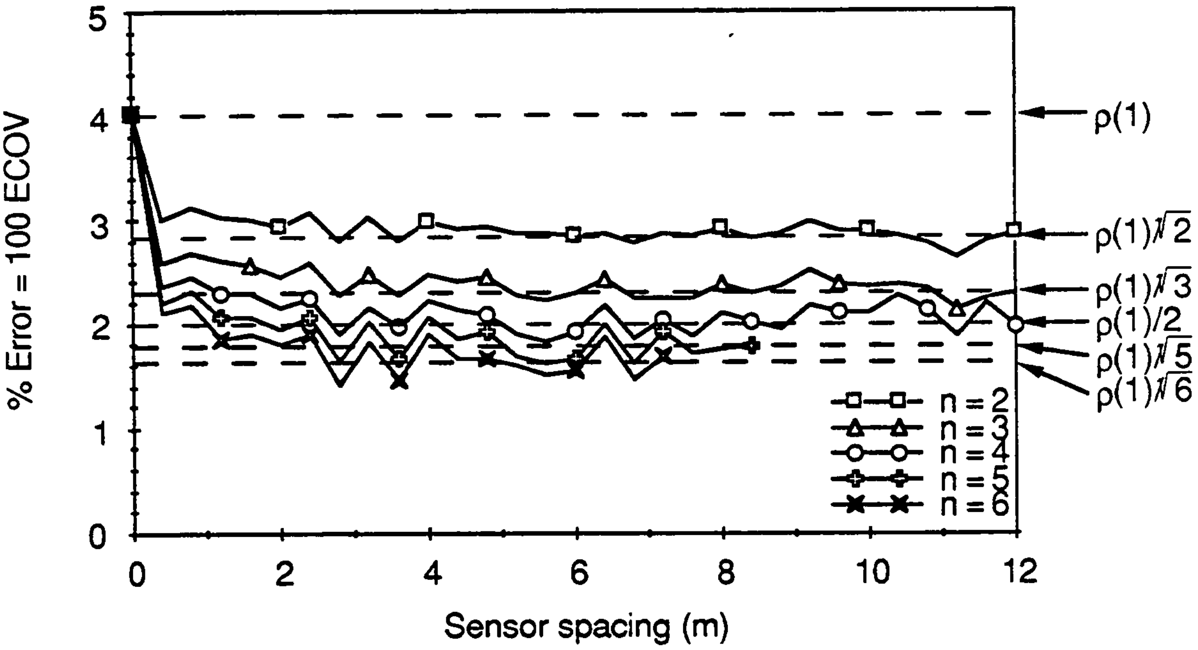

Fig 5.11 Experimental graphs of ρ vs Δ for the steering axle of vehicle S4, travelling in the 'Forward' direction at 11 km/h. The horizontal dashed lines show the values expected if the sensor errors were due to uncorrelated random noise with ECOV = ρ(1) only, with no contribution from dynamic loads.

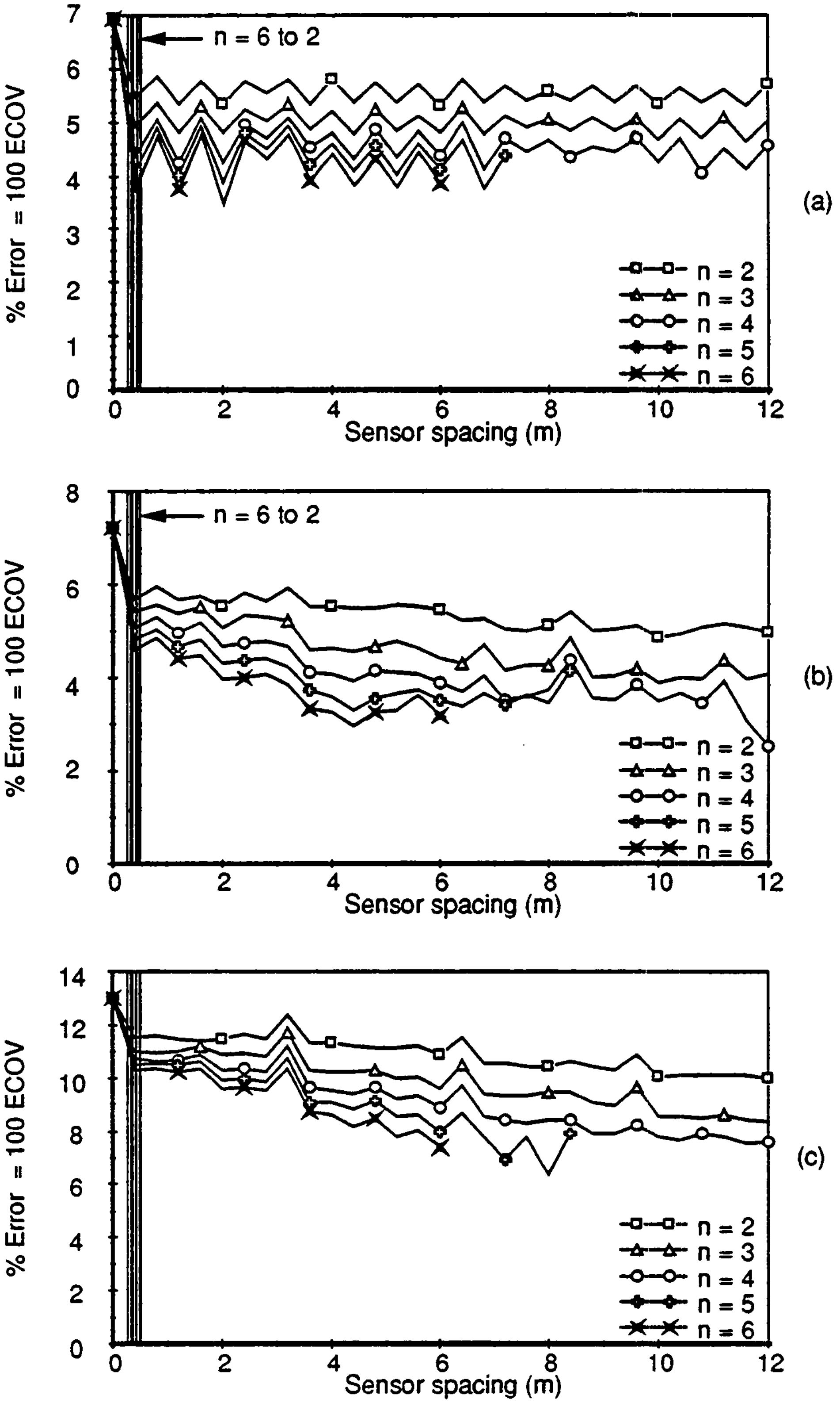

Fig. 5.12 WIM array error vs sensor spacing Vehicle S1,
Speed = 2.5 m/s (9 km/h) (a) Axle 1 (b) Axle 3 (c) Axle 5

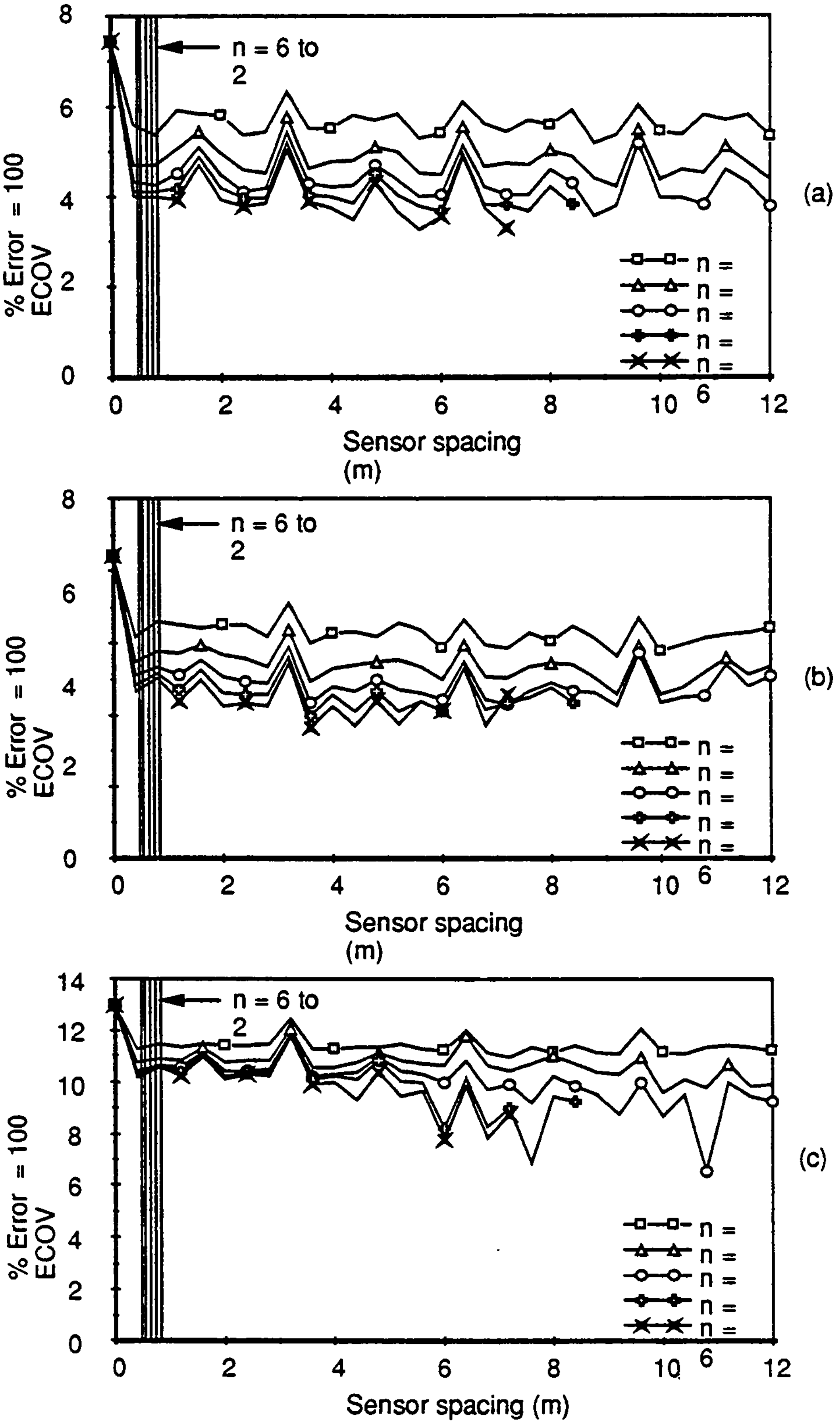

Fig. 5.13 WIM array error vs sensor spacing Vehicle S1,
Speed = 4.1 m/s (15 km/h) (a) Axle 1 (b) Axle 3 (c) Axle 5

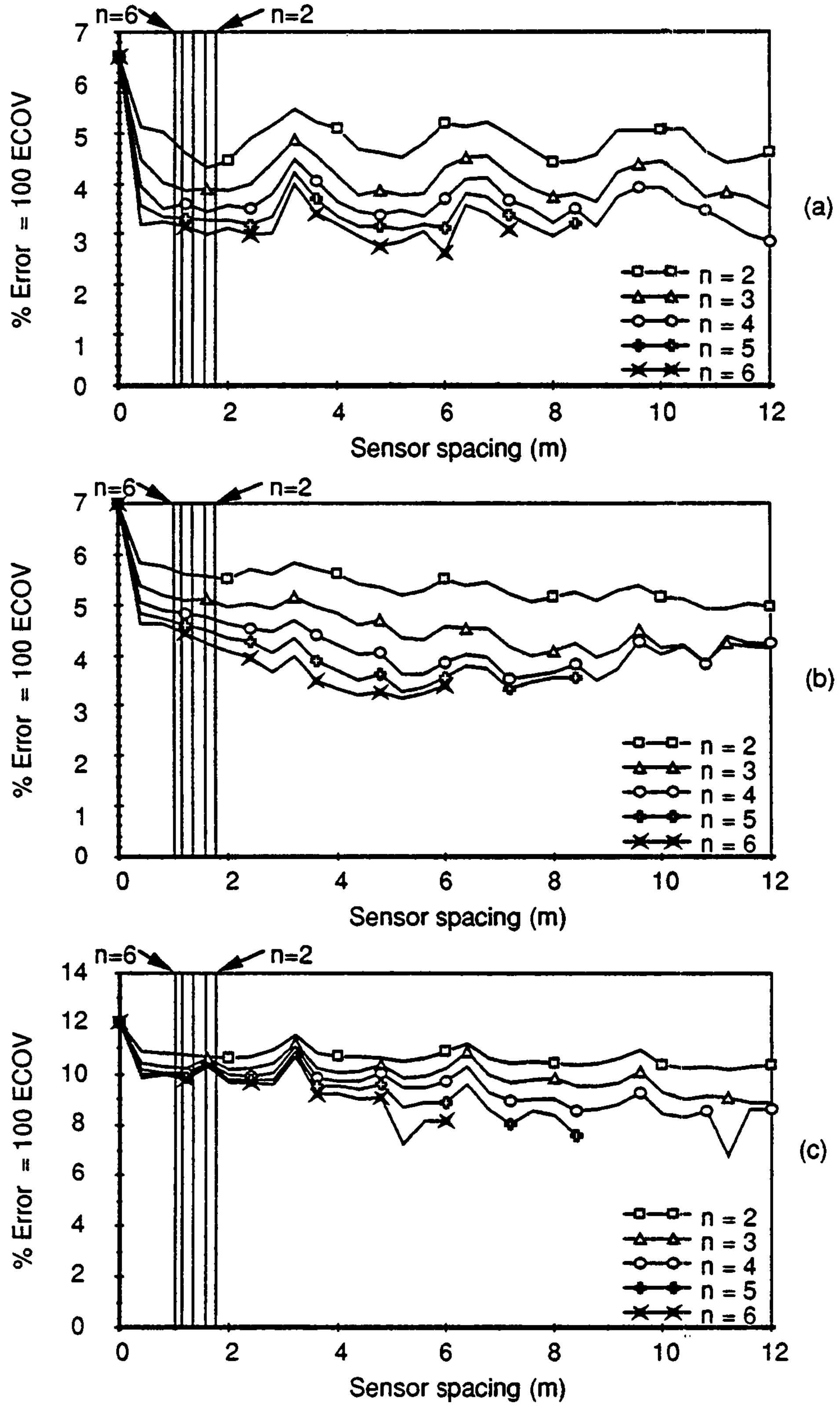

Fig. 5.14 WIM array error vs sensor spacing Vehicle S1,
Speed = 8.9 m/s (32 km/h) (a) Axle 1 (b) Axle 3 (c) Axle 5

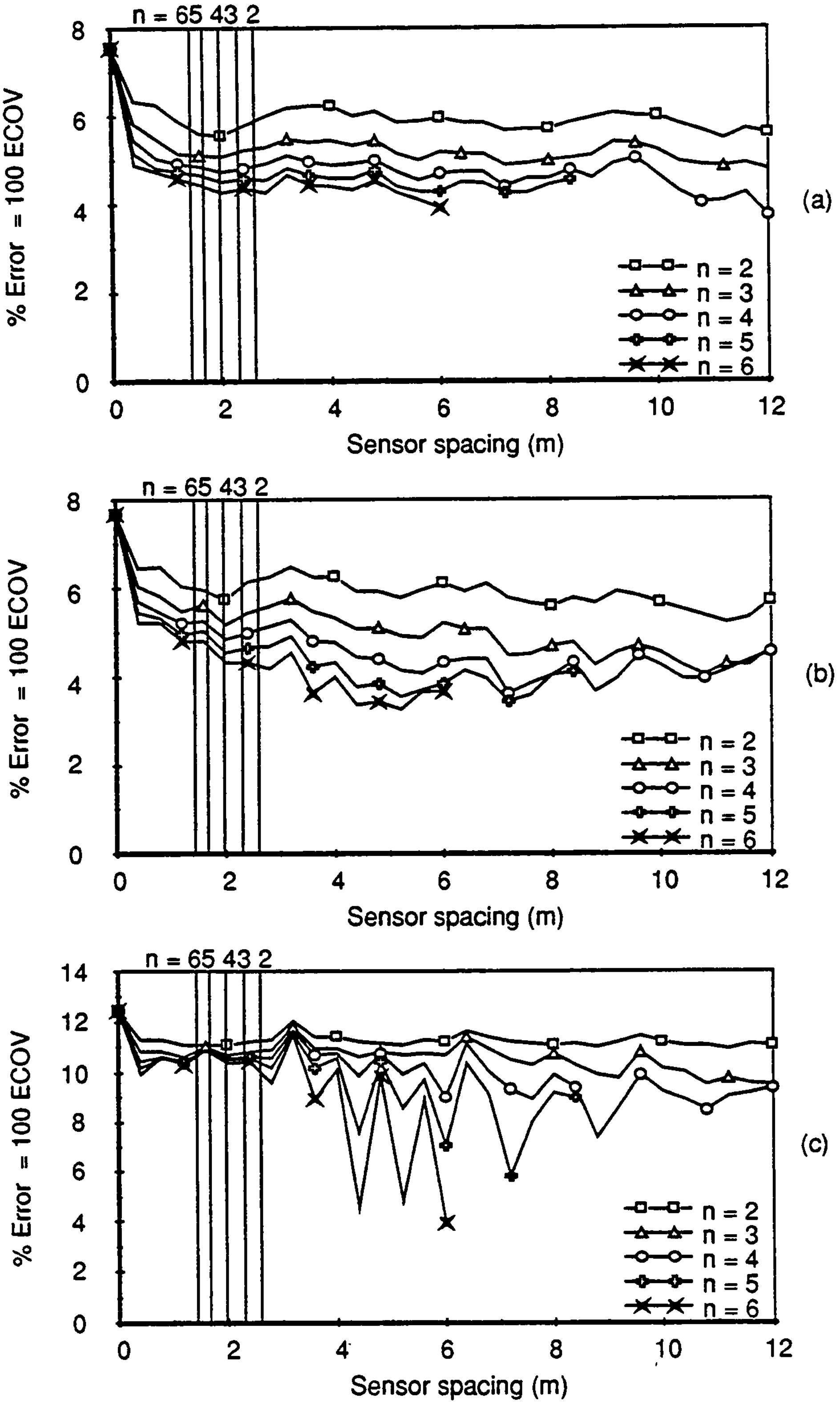

Fig. 5.15 WIM array error vs sensor spacing Vehicle S1,
Speed = 13.0 m/s (47 km/h) (a) Axle 1 (b) Axle 3 (c) Axle 5

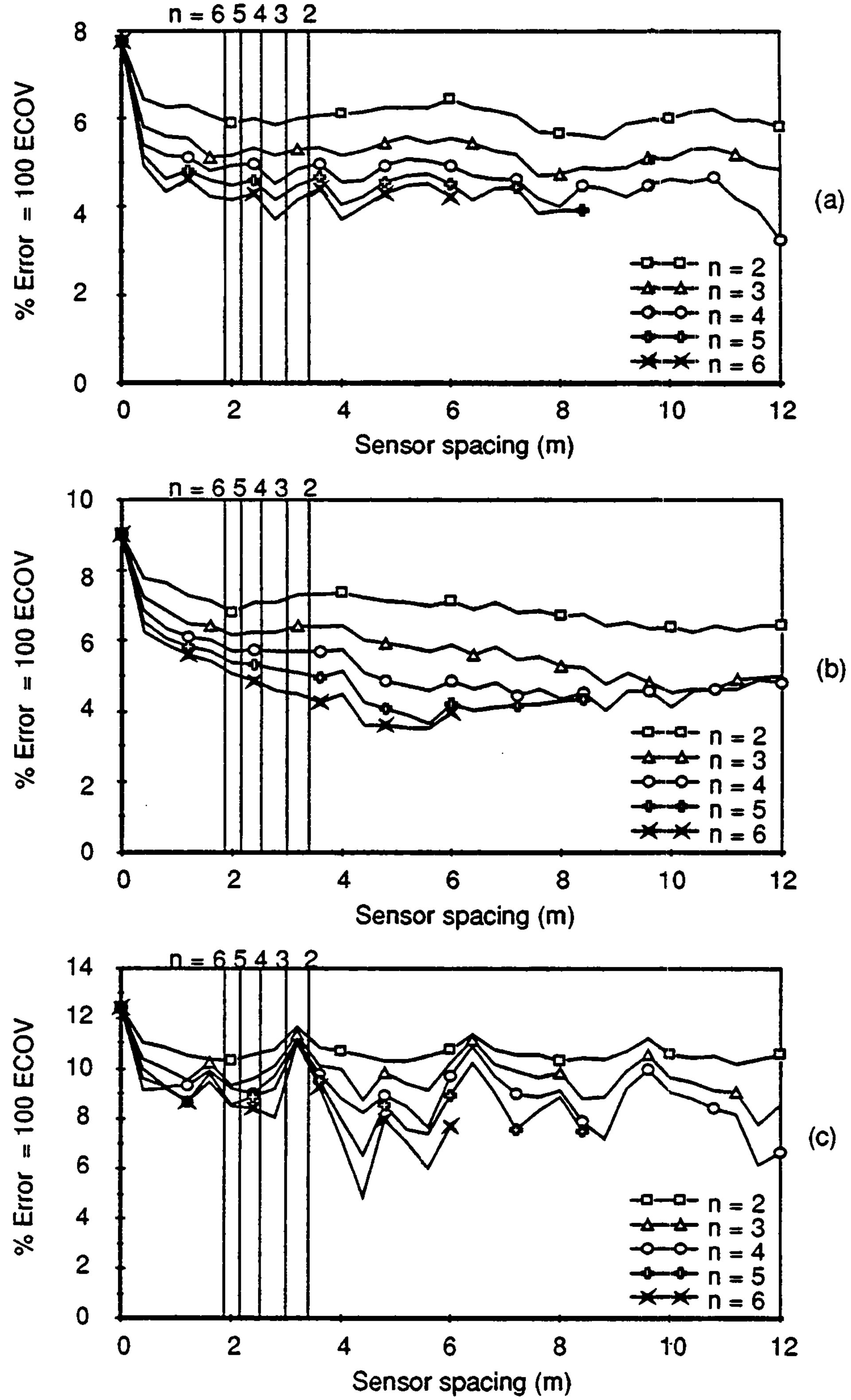

Fig. 5.16 WIM array error vs sensor spacing Vehicle S1,
Speed = 16.9 m/s (61 km/h) (a) Axle 1 (b) Axle 3 (c) Axle 5

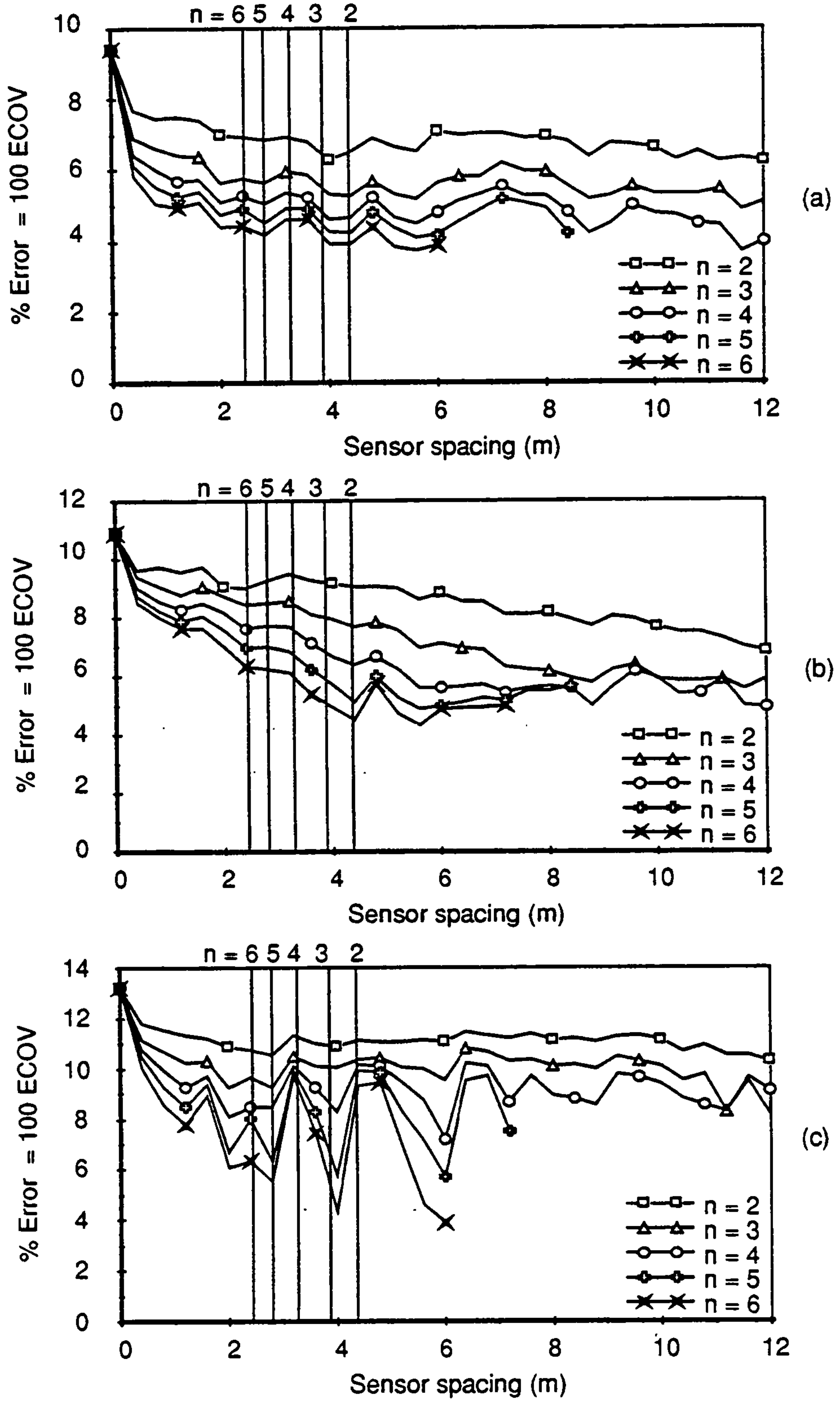

Fig. 5.17 WIM array error vs sensor spacing Vehicle S1,
Speed = 21.8 m/s (79 km/h) (a) Axle 1 (b) Axle 3 (c) Axle 5

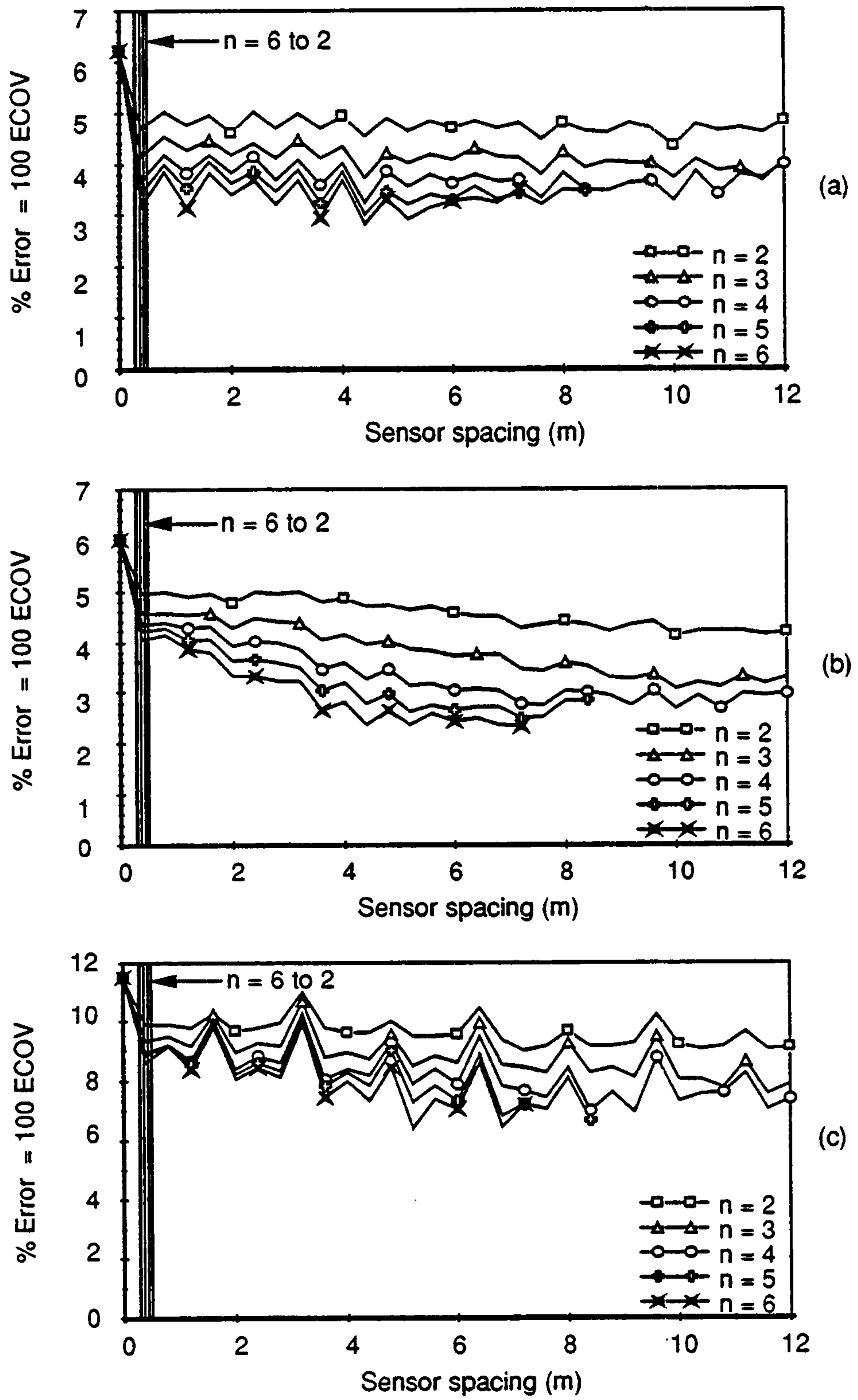

Fig. 5.18 WIM array error vs sensor spacing Vehicle S2,
Speed = 2.4 m/s (8.7 km/h) (a) Axle 1 (b) Axle 3 (c) Axle 5

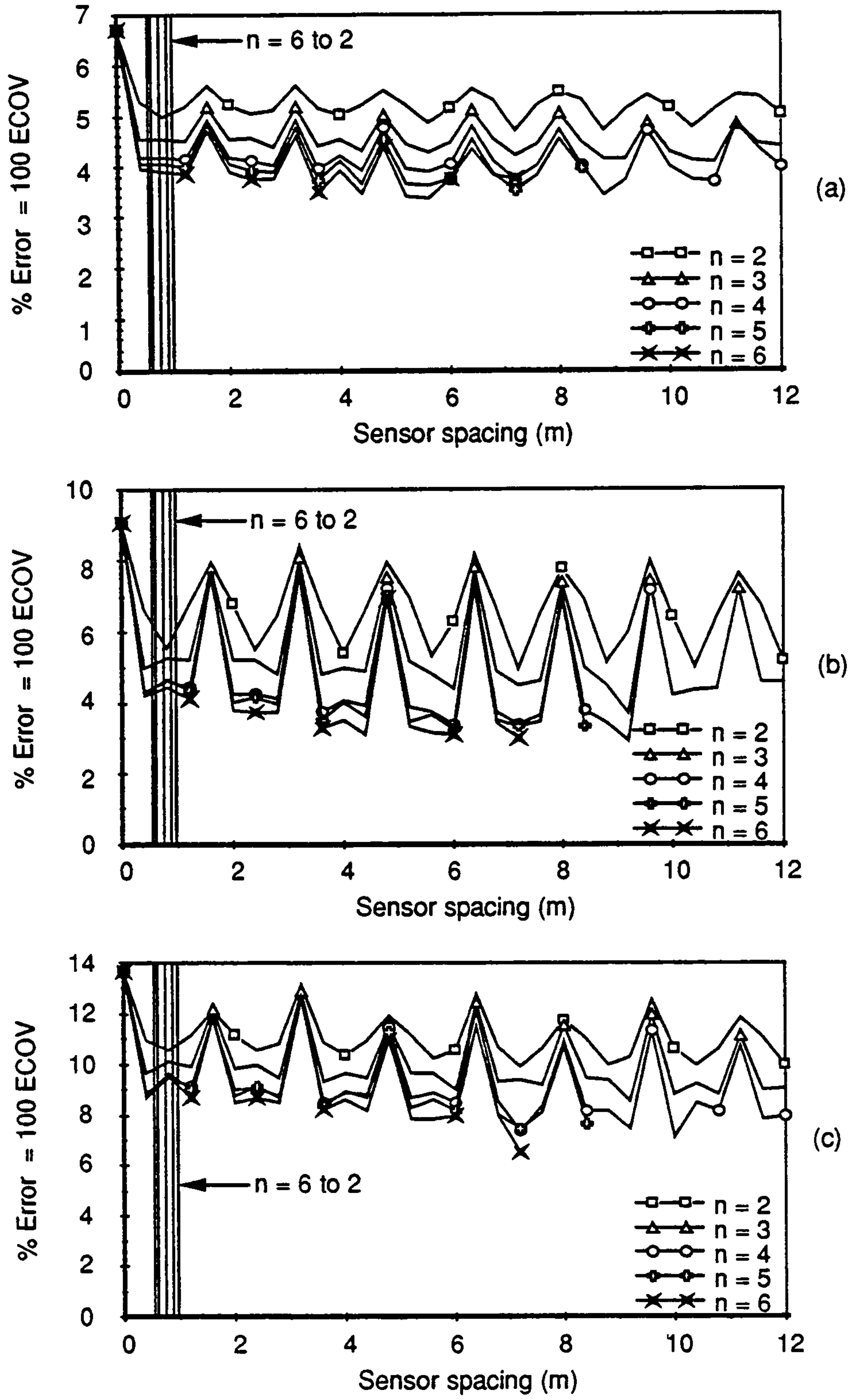

Fig. 5.19 WIM array error vs sensor spacing Vehicle S2,
Speed = 4.8 m/s (17 km/h) (a) Axle 1 (b) Axle 3 (c) Axle 5

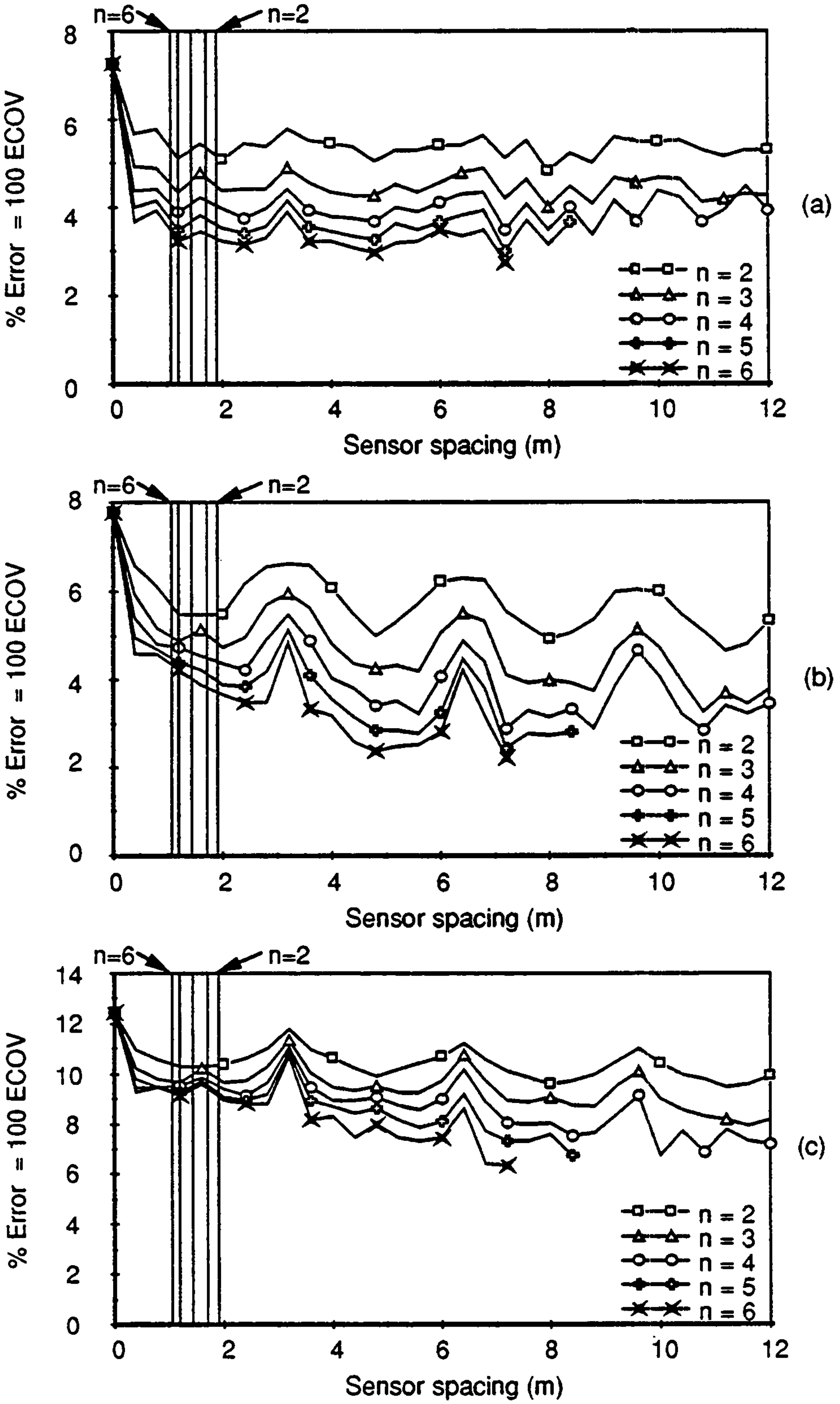

Fig. 5.20 WIM array error vs sensor spacing Vehicle S2,
Speed = 9.5 m/s (34 km/h) (a) Axle 1 (b) Axle 3 (c) Axle 5

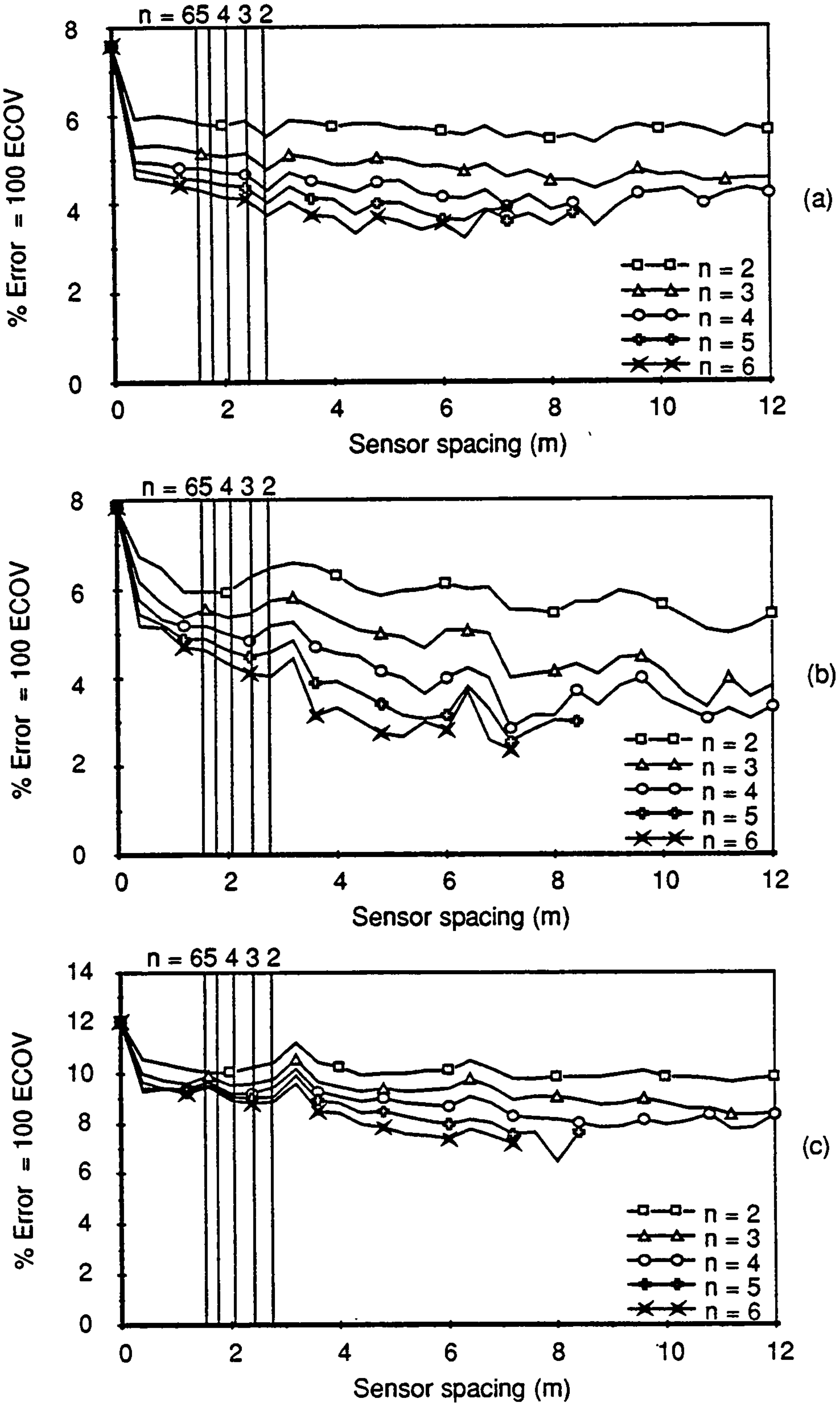

Fig. 5.21 WIM array error vs sensor spacing Vehicle S2,
Speed = 13.8 m/s (50 km/h) (a) Axle 1 (b) Axle 3 (c) Axle 5

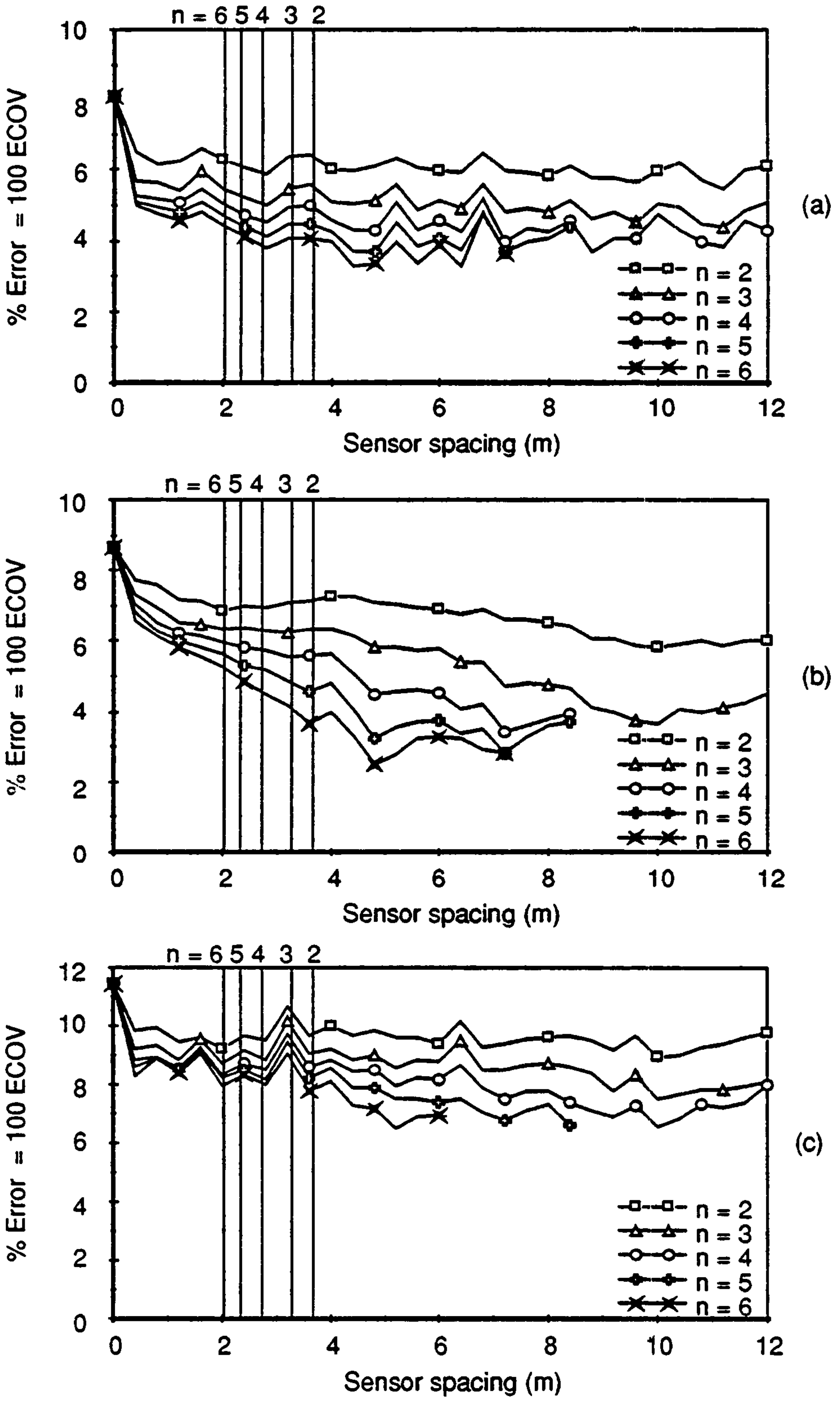

Fig. 5.22 WIM array error vs sensor spacing Vehicle S2,
Speed = 18.3 m/s (66 km/h) (a) Axle 1 (b) Axle 3 (c) Axle 5

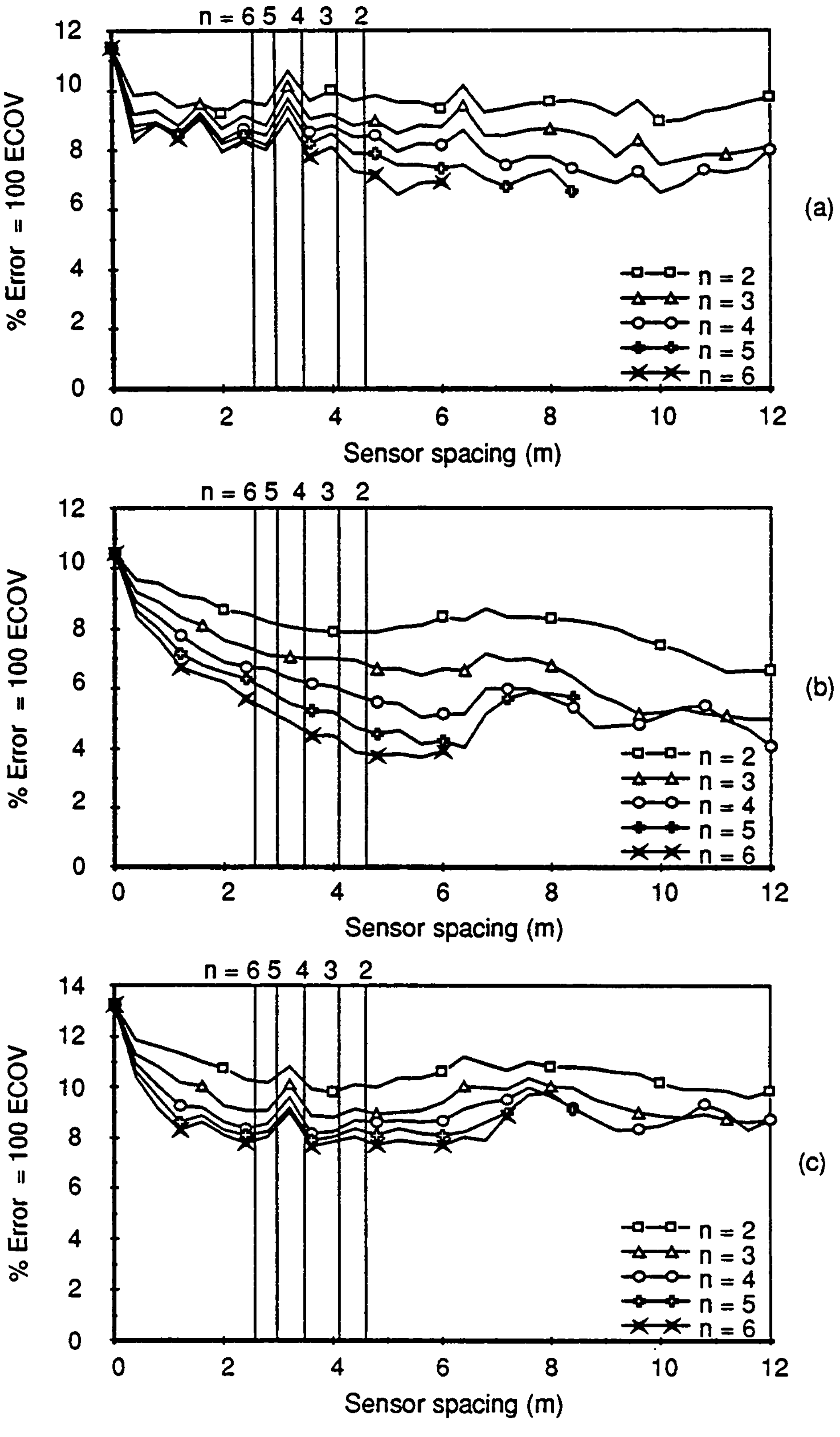

Fig. 5.23 WIM array error vs sensor spacing Vehicle S2,
Speed = 23.0 m/s (83 km/h) (a) Axle 1 (b) Axle 3 (c) Axle 5

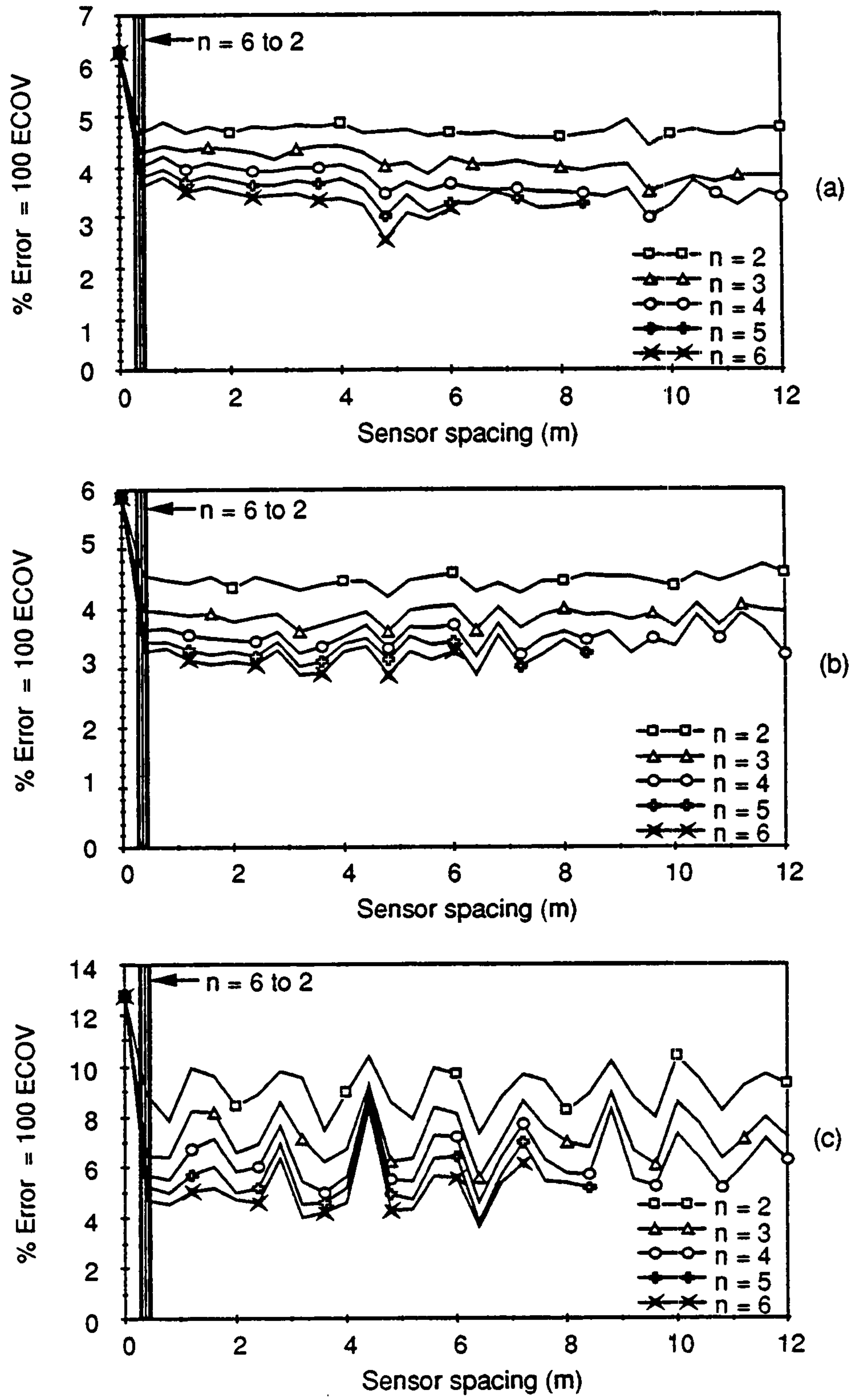

Fig. 5.24 WIM array error vs sensor spacing Vehicle S3,
Speed = 2.4 m/s (8.5 km/h) (a) Axle 1 (b) Axle 3 (c) Axle 5

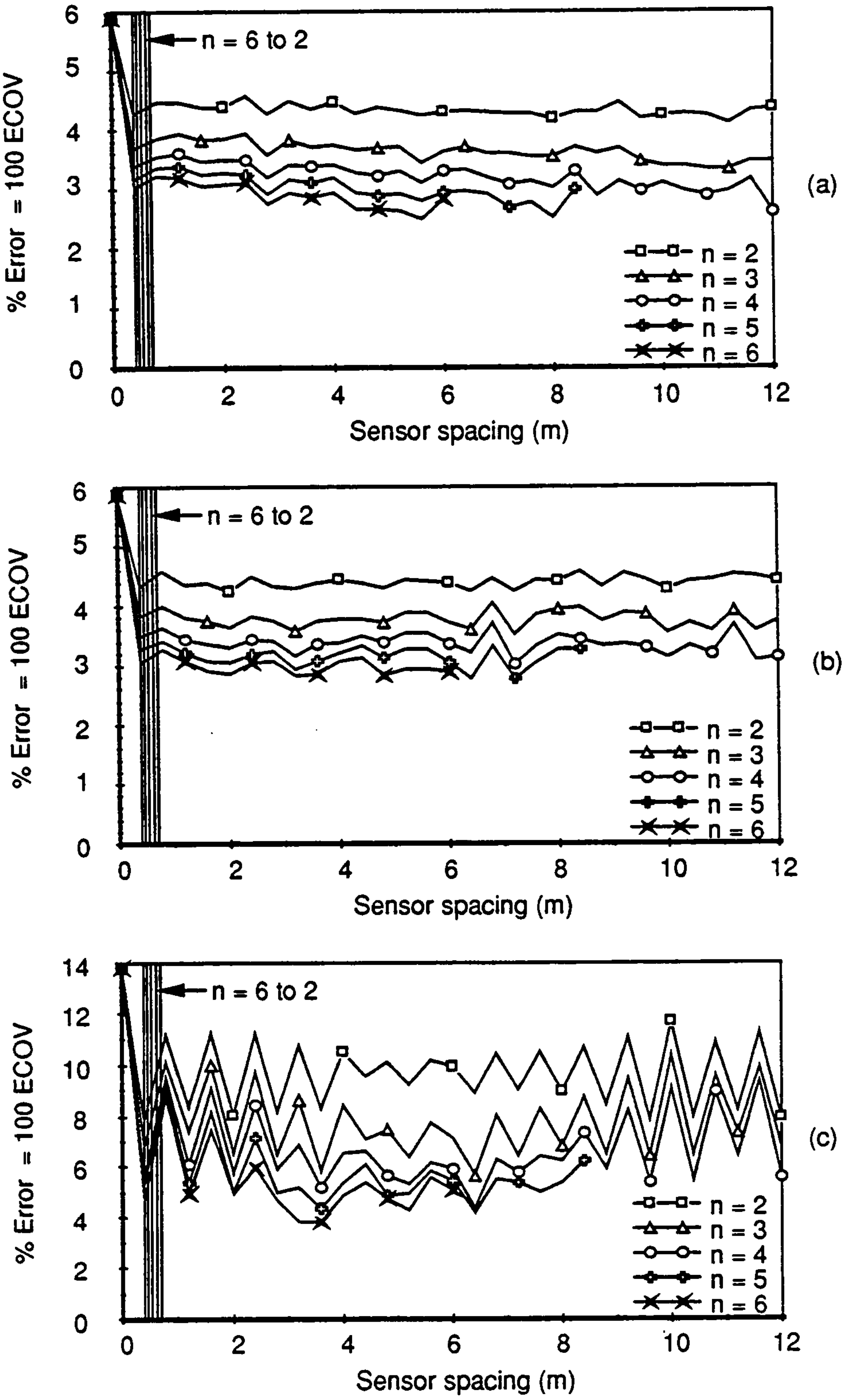

Fig. 5.25 WIM array error vs sensor spacing Vehicle S3,
Speed = 3.5 m/s (13 km/h) (a) Axle 1 (b) Axle 3 (c) Axle 5

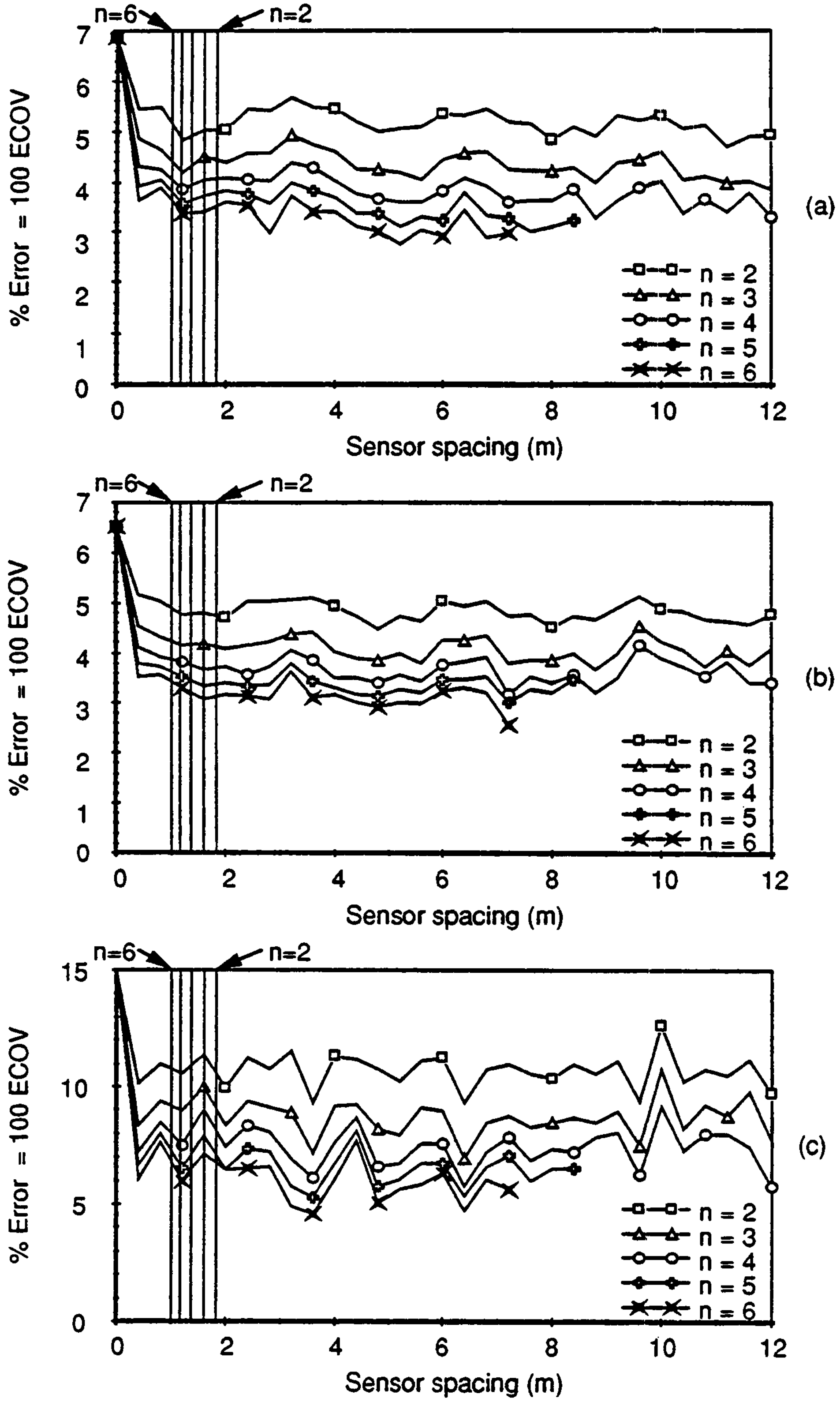

Fig. 5.26 WIM array error vs sensor spacing Vehicle S3,
Speed = 9.1 m/s (33 km/h) (a) Axle 1 (b) Axle 3 (c) Axle 5

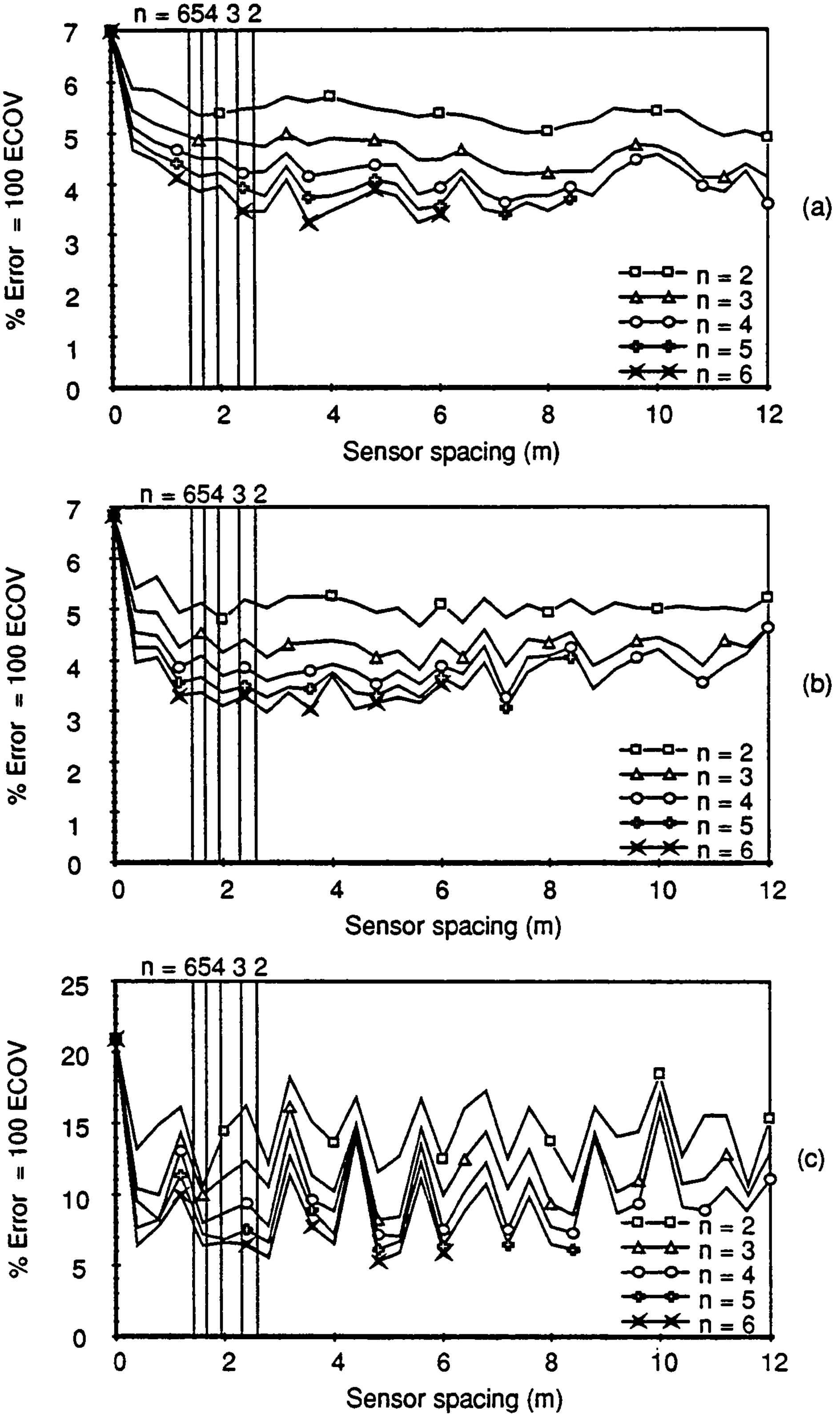

Fig. 5.27 WIM array error vs sensor spacing Vehicle S3,
Speed = 13.0 m/s (47 km/h) (a) Axle 1 (b) Axle 3 (c) Axle 5

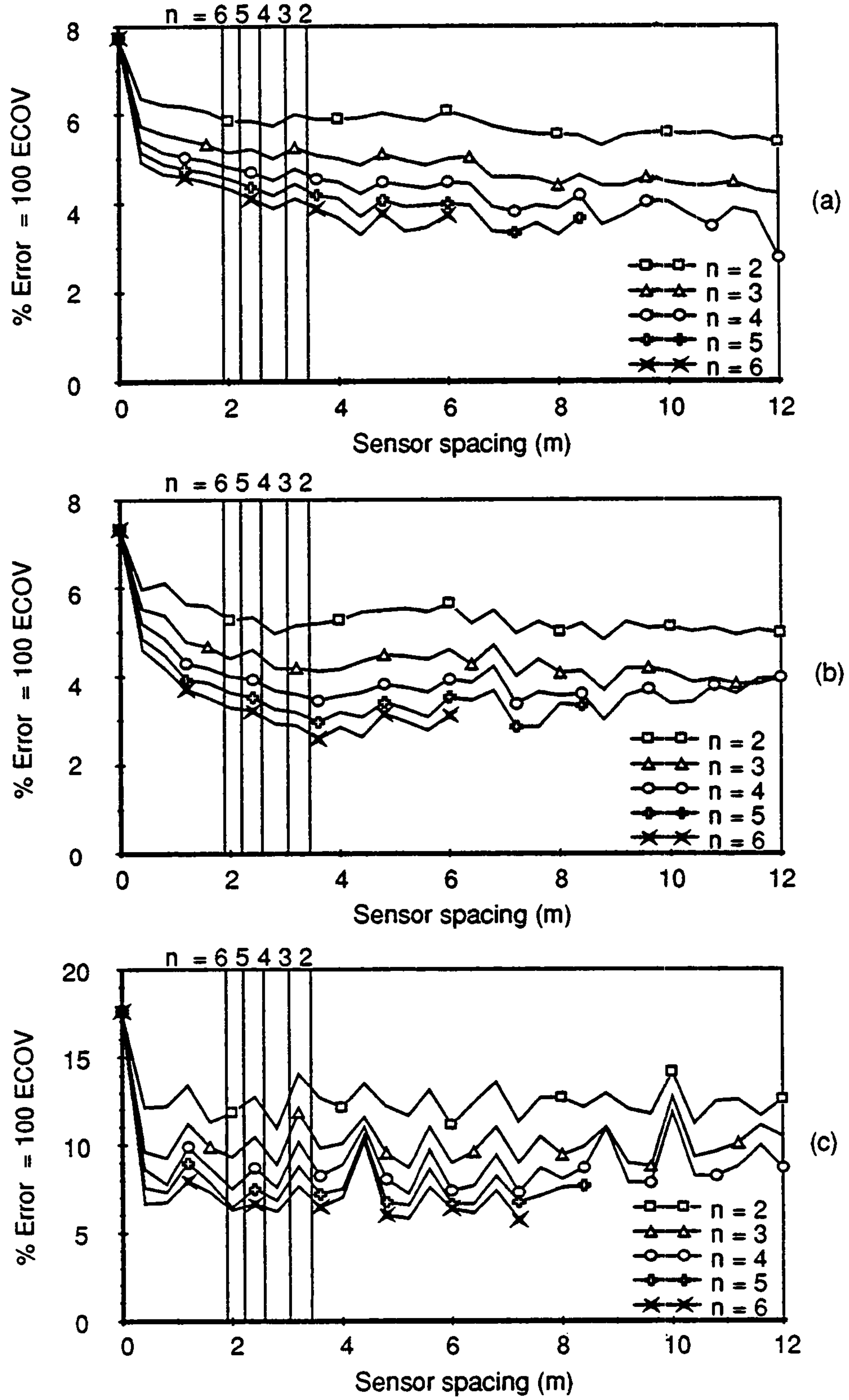

Fig. 5.28 WIM array error vs sensor spacing Vehicle S3,
Speed = 17.1 m/s (62 km/h) (a) Axle 1 (b) Axle 3 (c) Axle 5

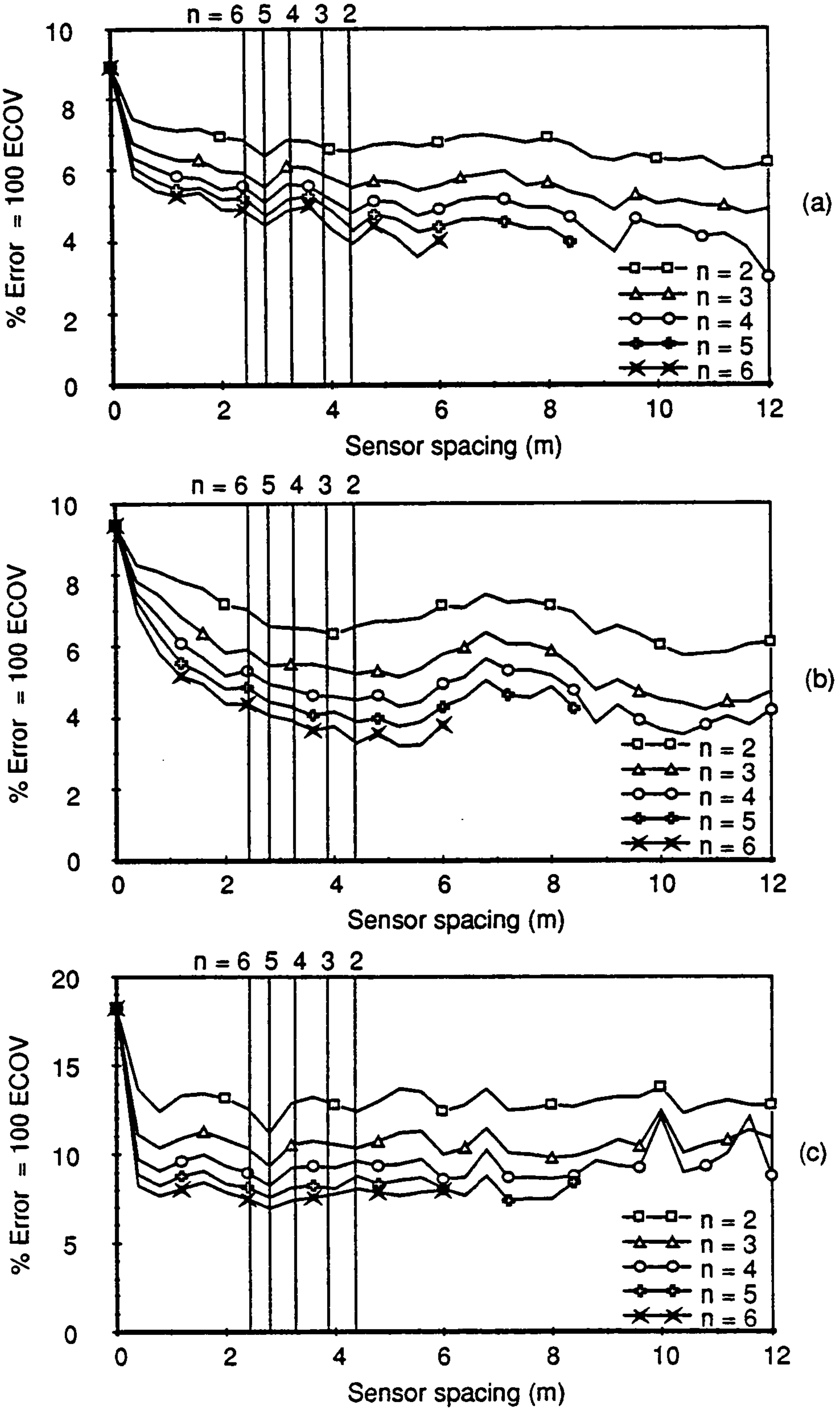

Fig. 5.29 WIM array error vs sensor spacing Vehicle S3,
Speed = 21.8 m/s (78 km/h) (a) Axle 1 (b) Axle 3 (c) Axle 5

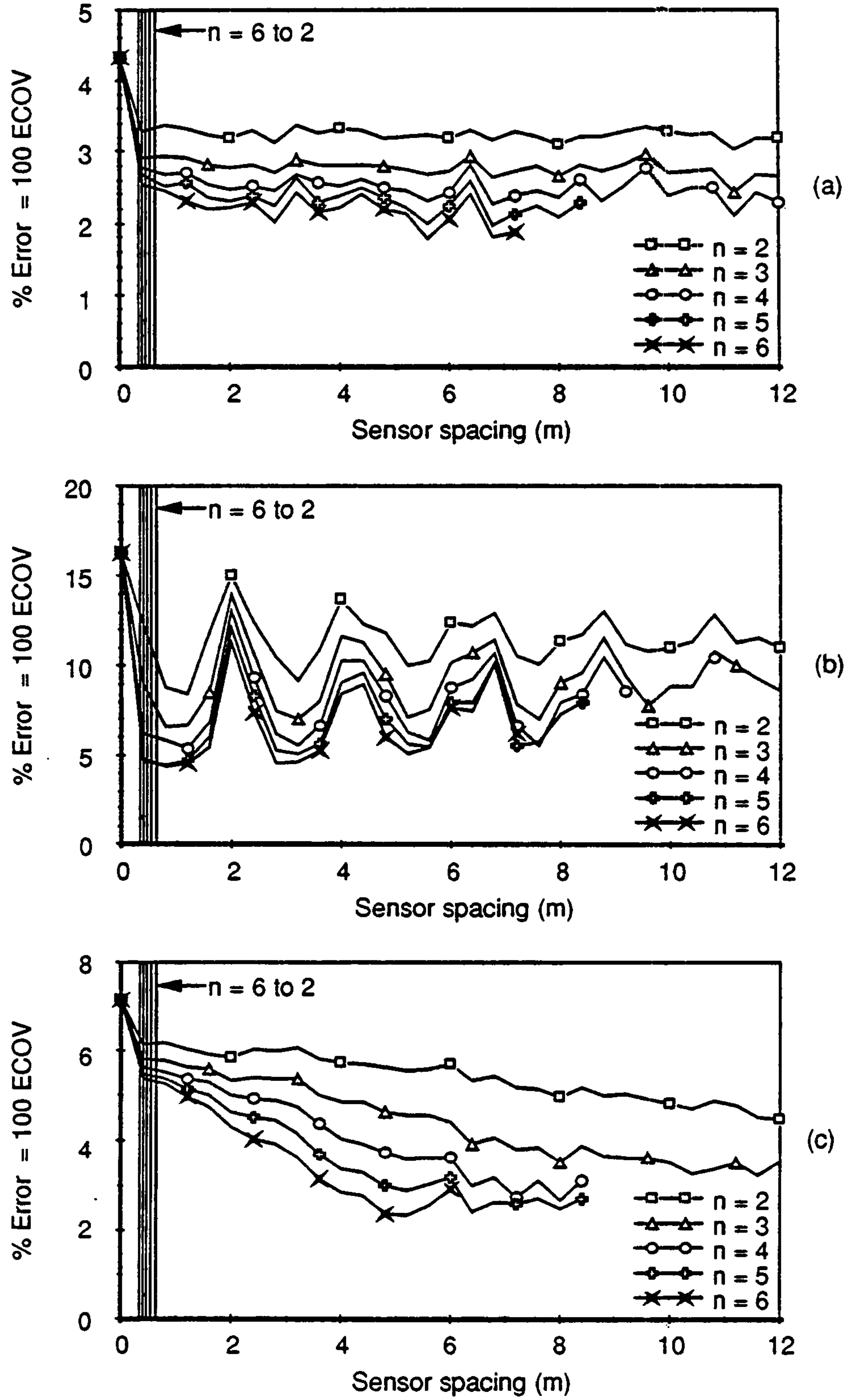

Fig. 5.30 WIM array error vs sensor spacing Vehicle S4,
Speed = 3.1 m/s (11 km/h) (a) Axle 1 (b) Axle 3 (c) Axle 5

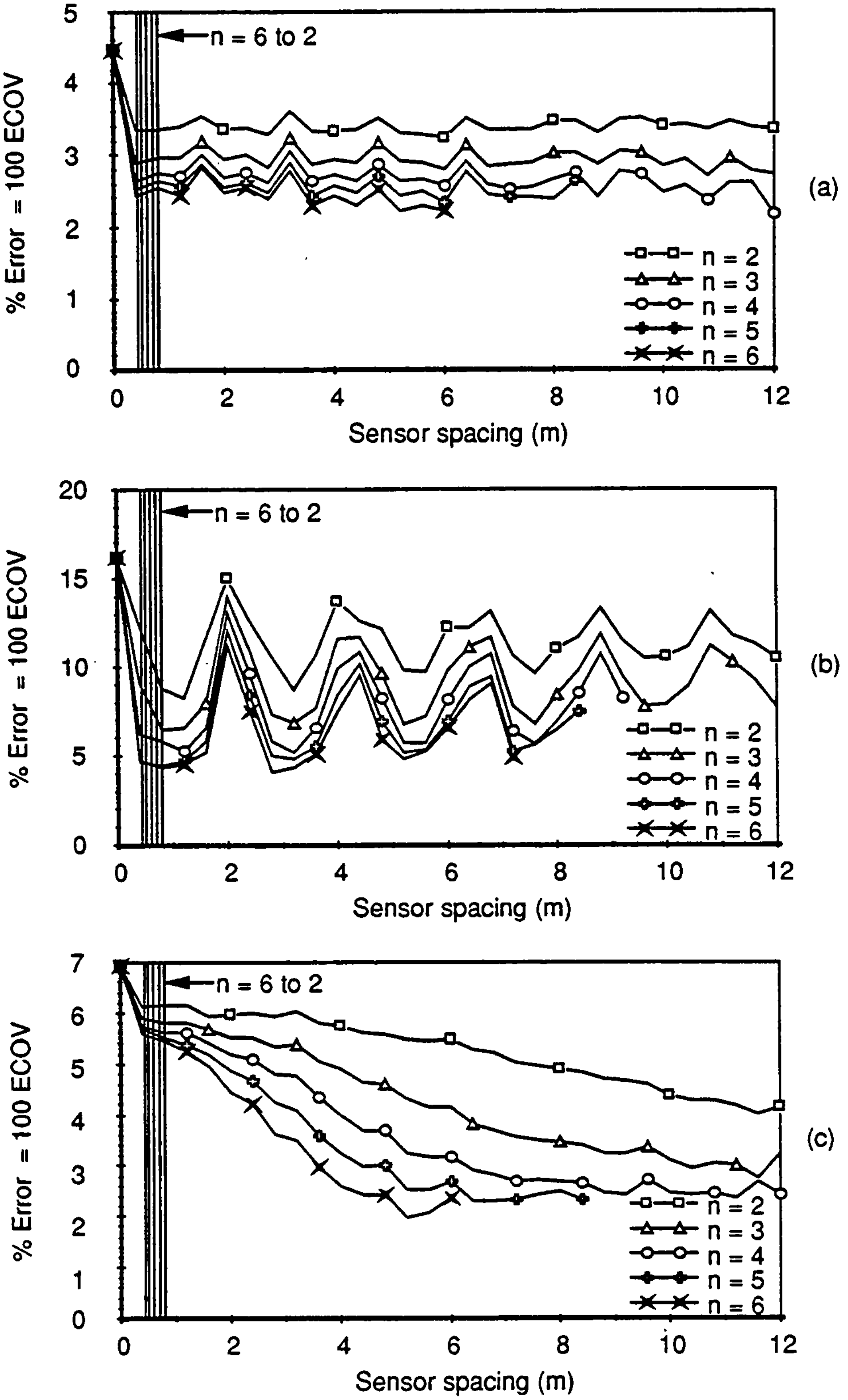

Fig. 5.31 WIM array error vs sensor spacing Vehicle S4,
Speed = 4.0 m/s (14 km/h) (a) Axle 1 (b) Axle 3 (c) Axle 5

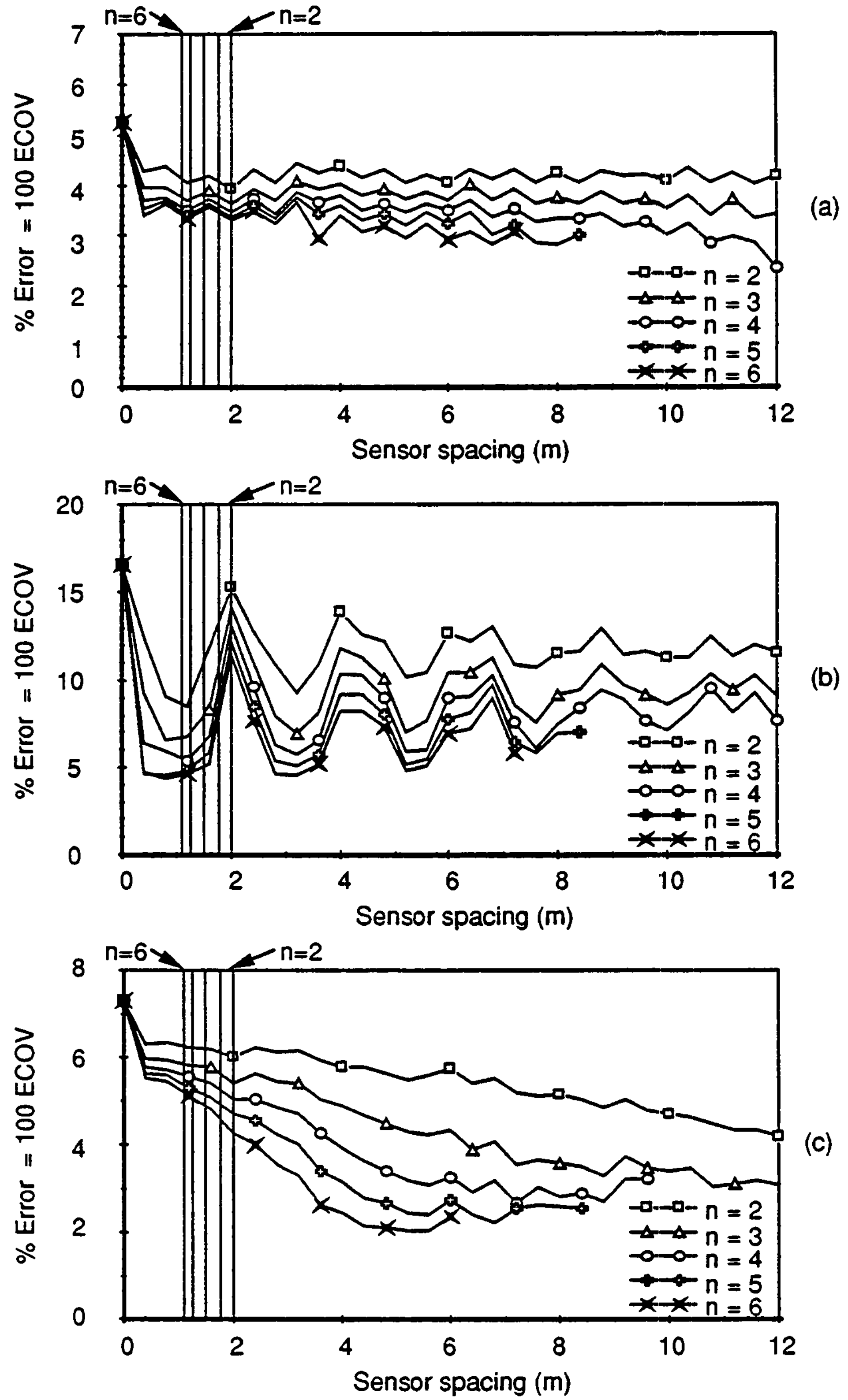

Fig. 5.32 WIM array error vs sensor spacing Vehicle S4,
Speed = 9.9 m/s (36 km/h) (a) Axle 1 (b) Axle 3 (c) Axle 5

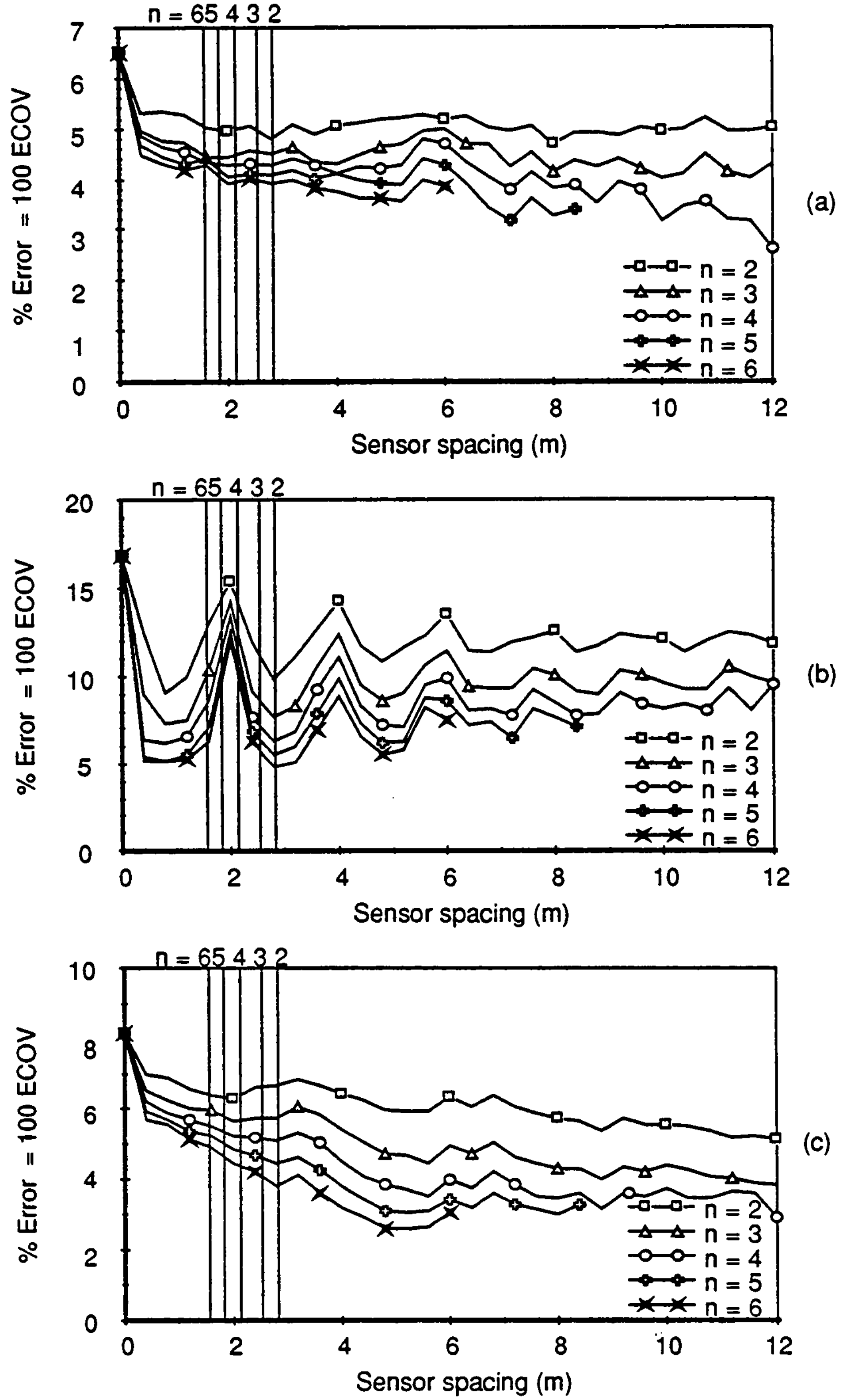

Fig. 5.33 WIM array error vs sensor spacing Vehicle S4,
Speed = 14.2 m/s (51 km/h) (a) Axle 1 (b) Axle 3 (c) Axle 5

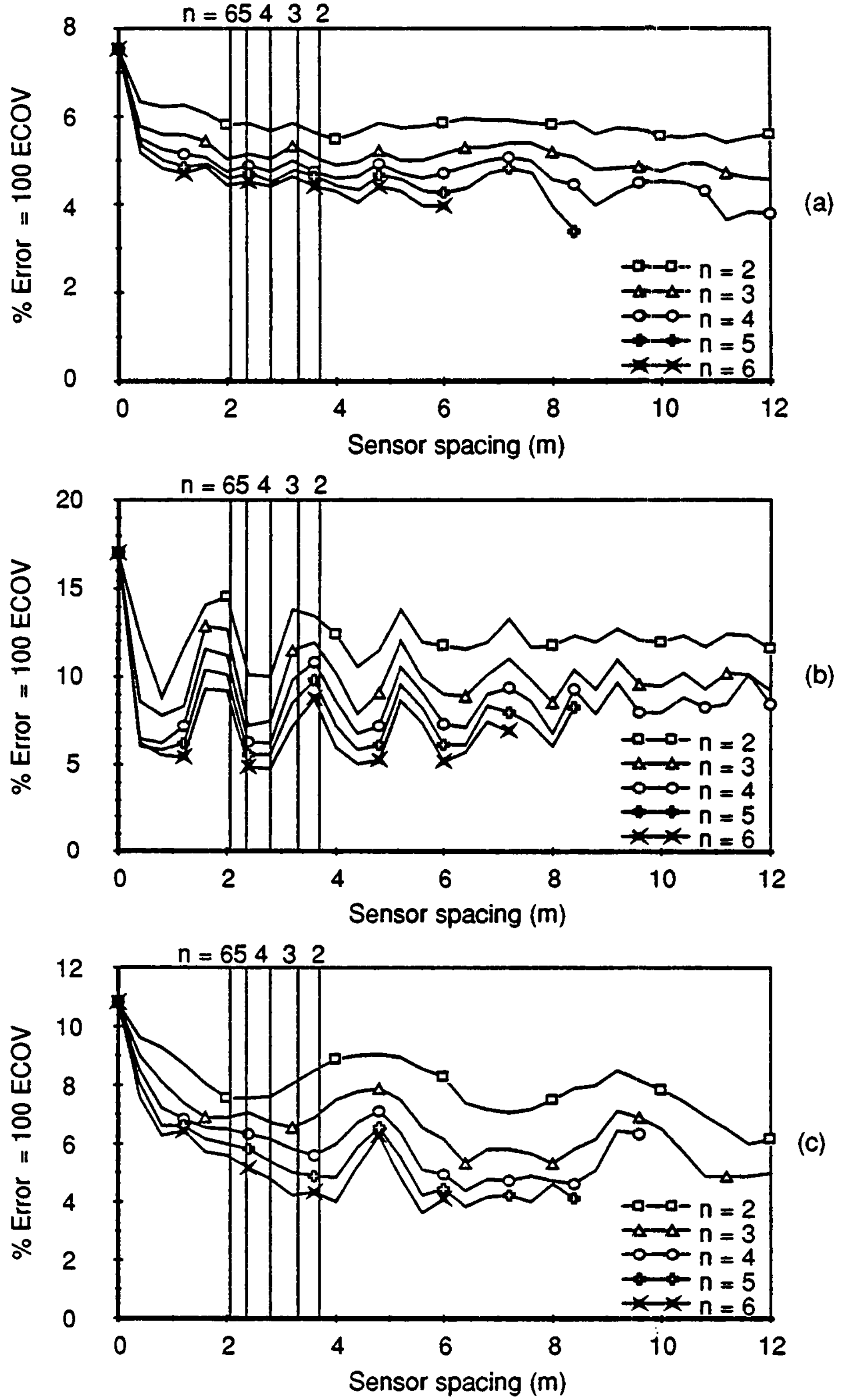

Fig. 5.34 WIM array error vs sensor spacing Vehicle S4,
Speed = 18.6 m/s (67 km/h) (a) Axle 1 (b) Axle 3 (c) Axle 5

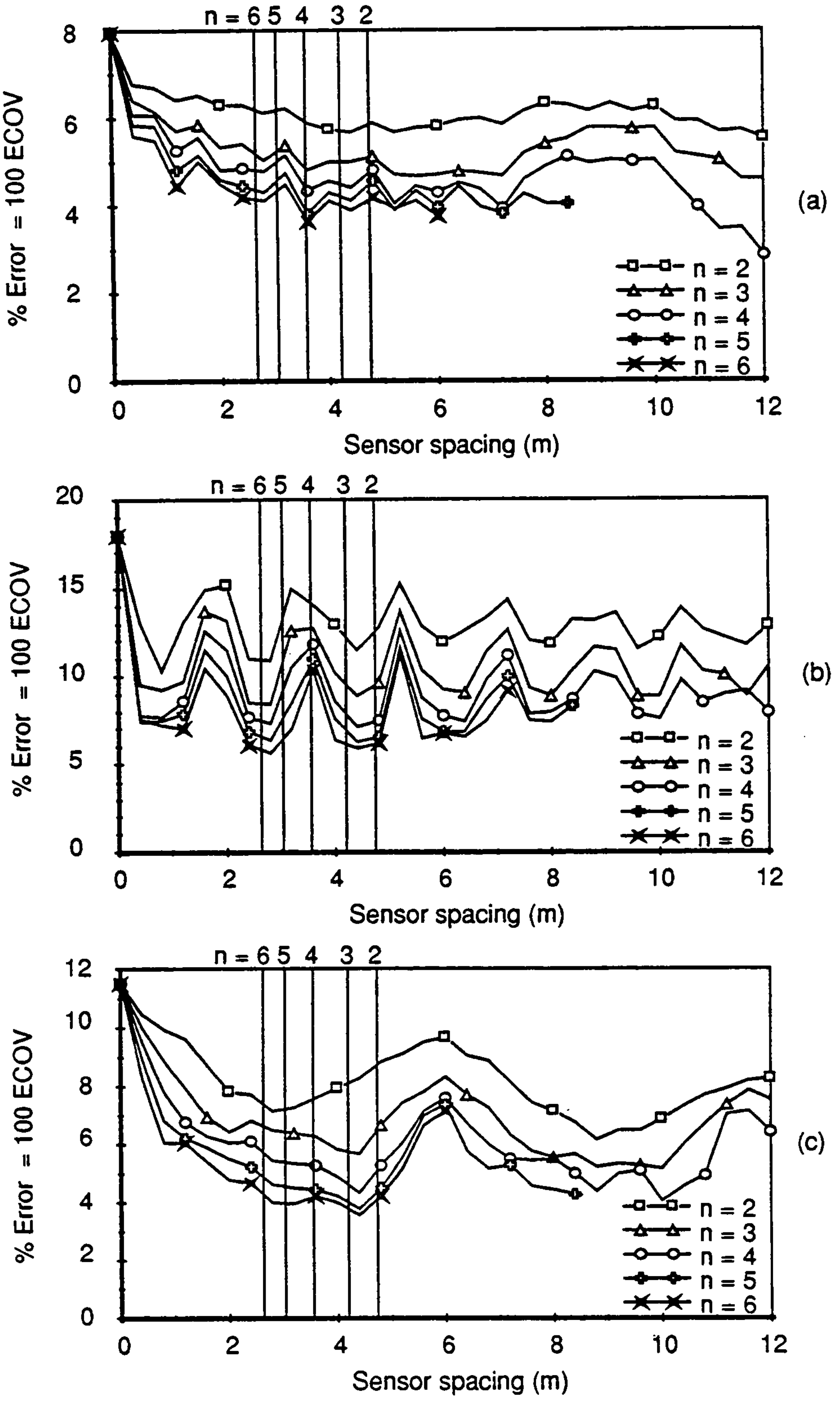

Fig. 5.35 WIM array error vs sensor spacing Vehicle S4,
Speed = 23.7 m/s (85 km/h) (a) Axle 1 (b) Axle 3 (c) Axle 5

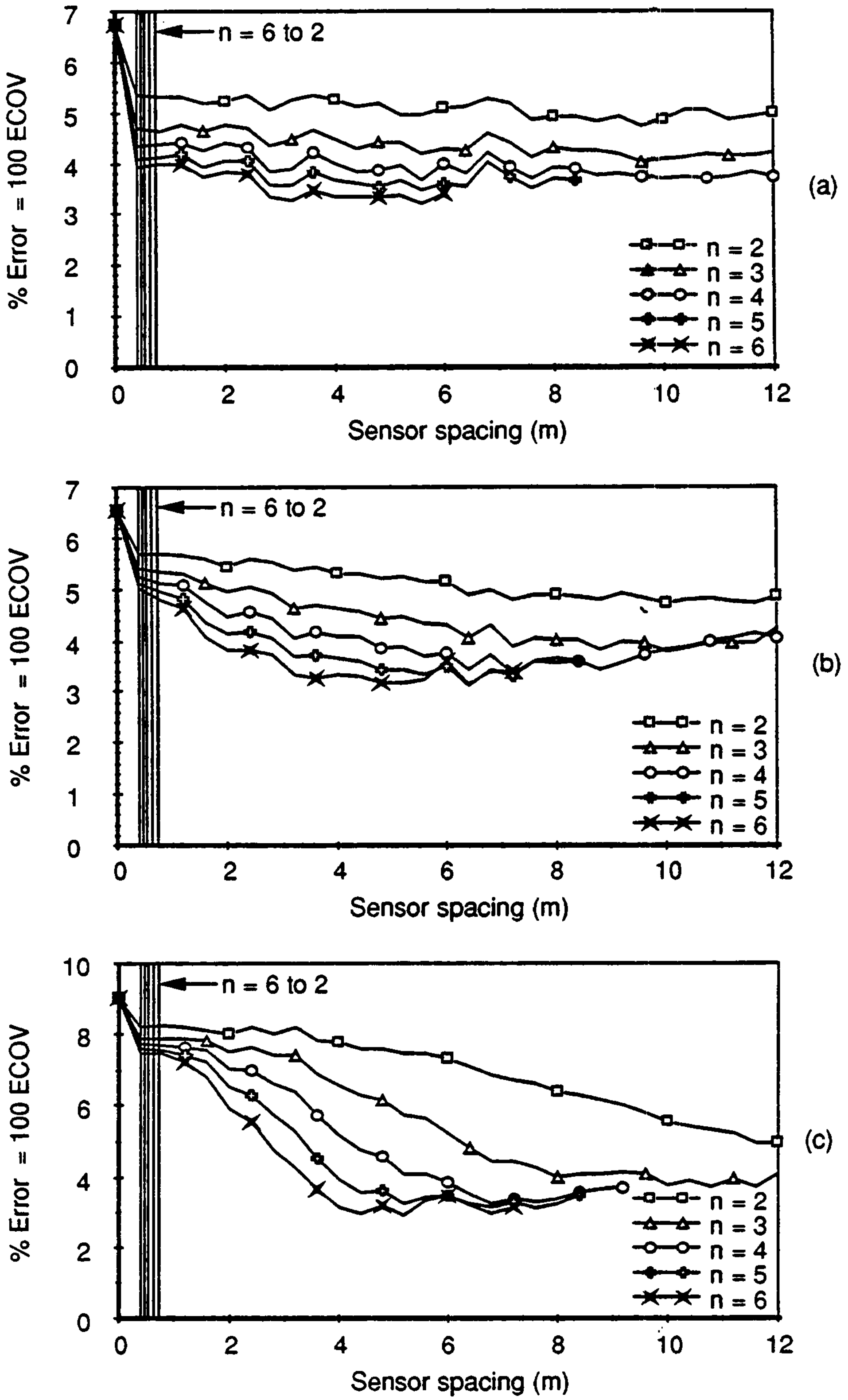

Fig. 5.36 WIM array error vs sensor spacing Vehicle S5,
Speed = 3.6 m/s (13 km/h) (a) Axle 1 (b) Axle 3 (c) Axle 5

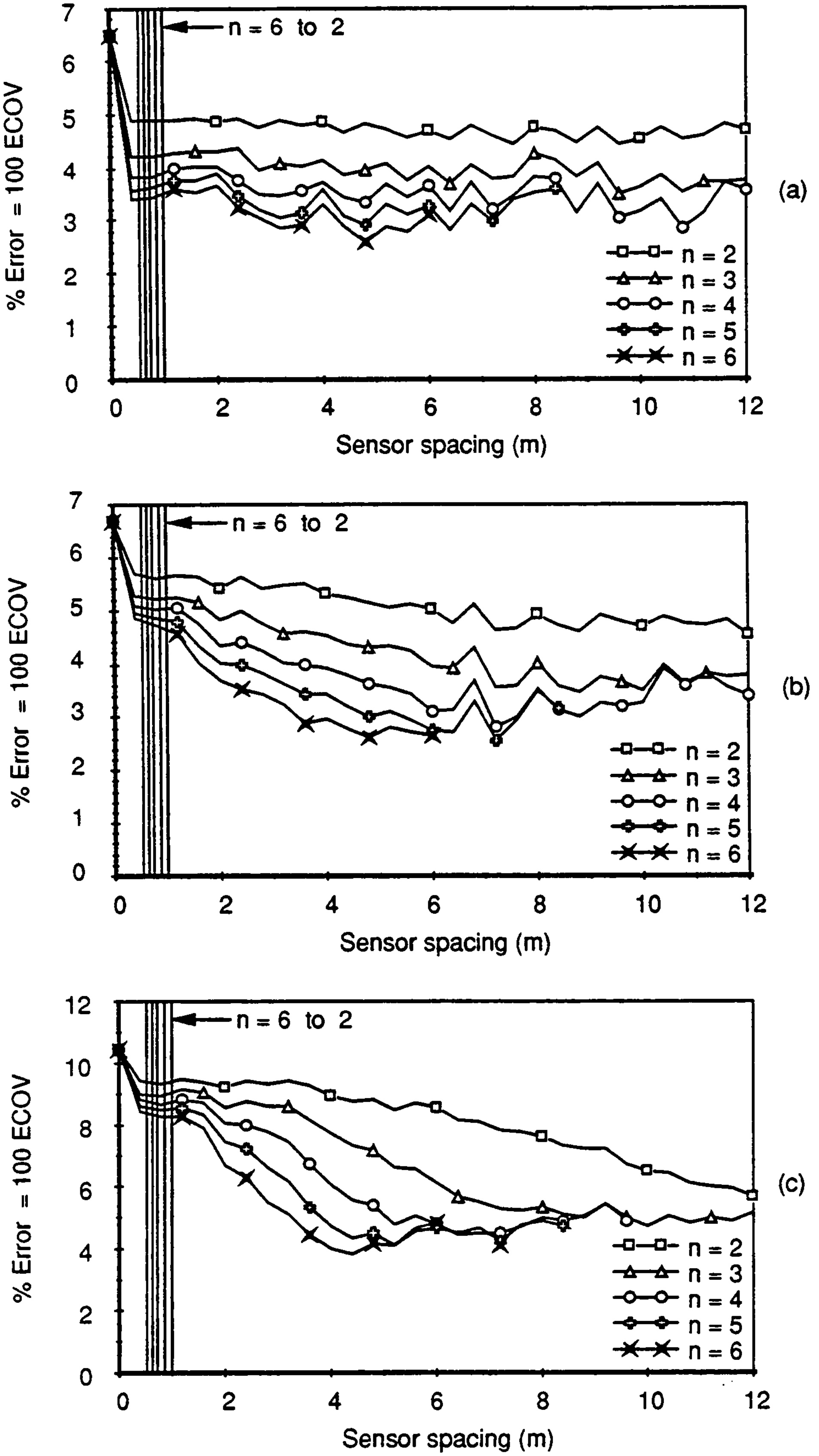

Fig. 5.37 WIM array error vs sensor spacing
Vehicle S5, Speed = 4.9 m/s (18 km/h)
(a) Axle 1 (b) Axle 3 (c) Axle 5

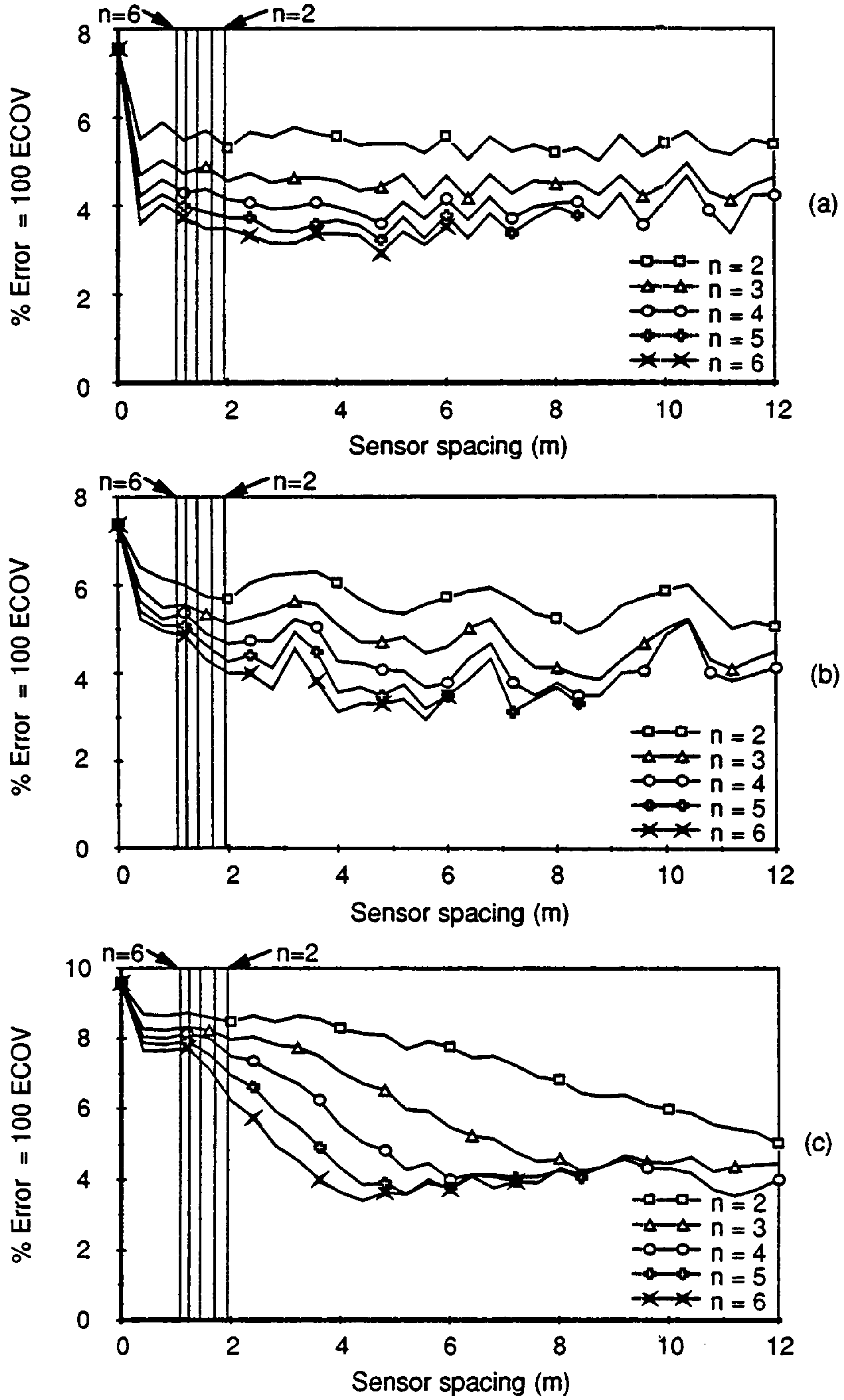

Fig. 5.38 WIM array error vs sensor spacing Vehicle S5,
Speed = 9.6 m/s (35 km/h) (a) Axle 1 (b) Axle 3 (c) Axle 5

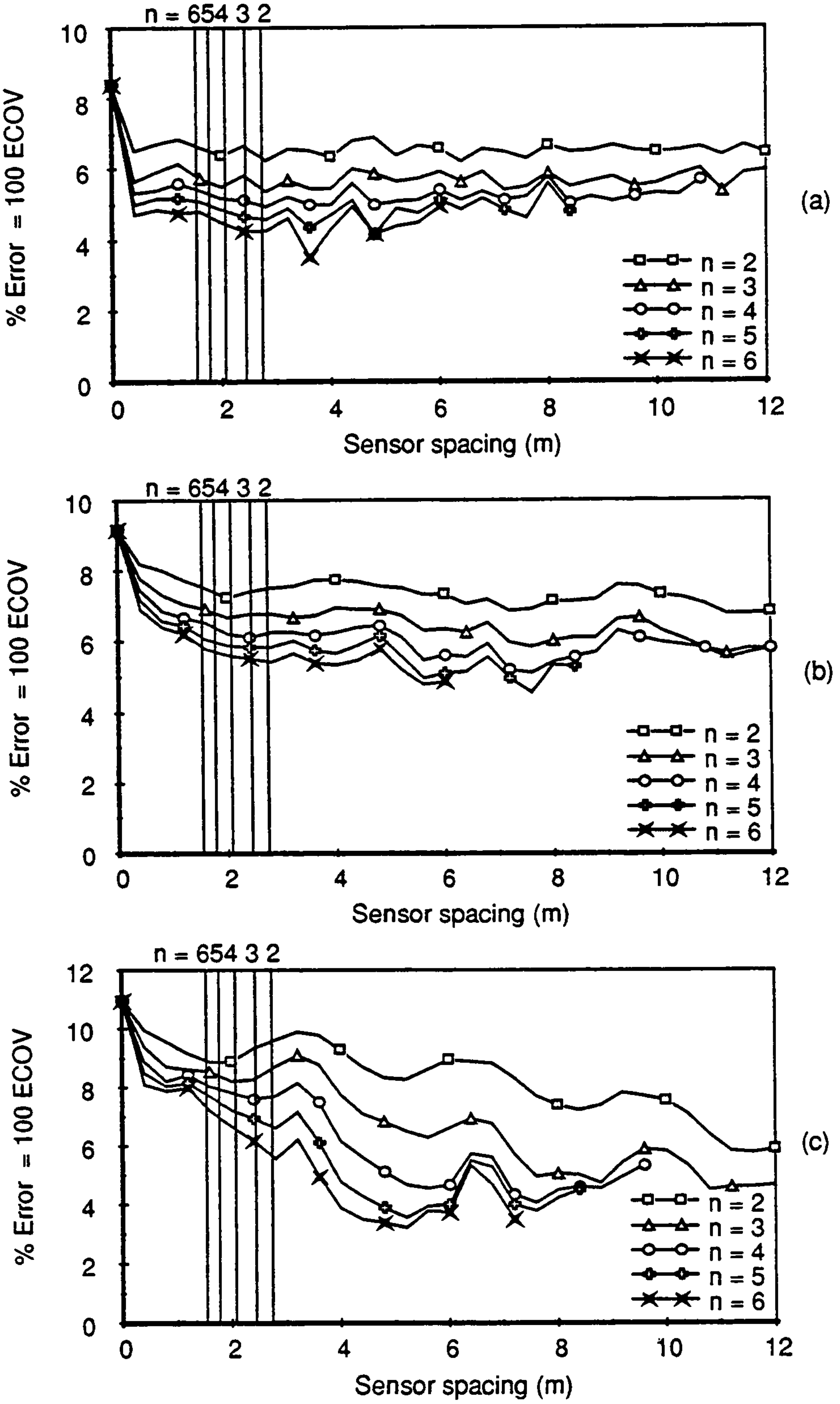

Fig. 5.39 WIM array error vs sensor spacing Vehicle S5,
Speed = 13.7 m/s (49 km/h) (a) Axle 1 (b) Axle 3 (c) Axle 5

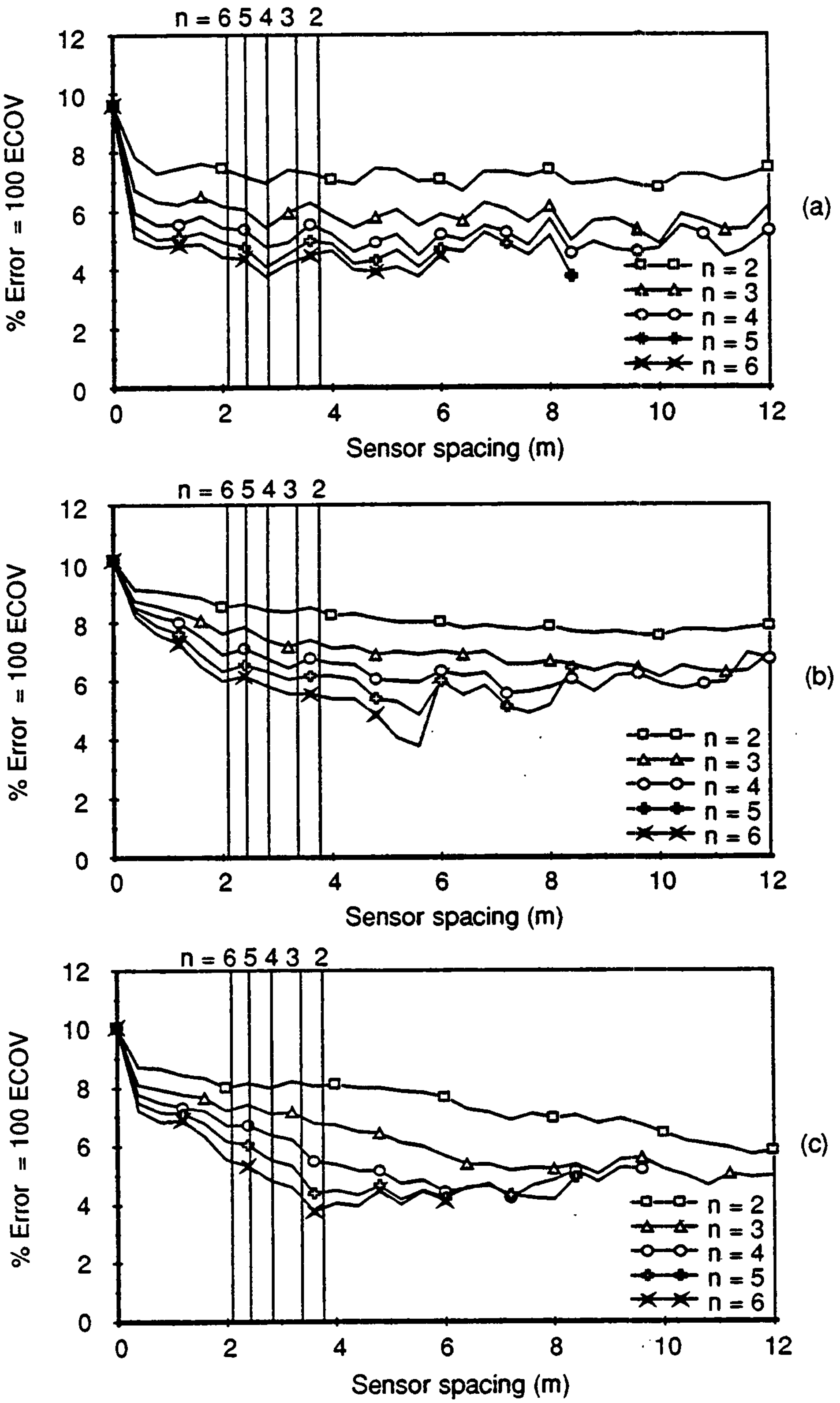

Fig. 5.40 WIM array error vs sensor spacing Vehicle S5,
Speed = 18.9 m/s (68 km/h) (a) Axle 1 (b) Axle 3 (c) Axle 5

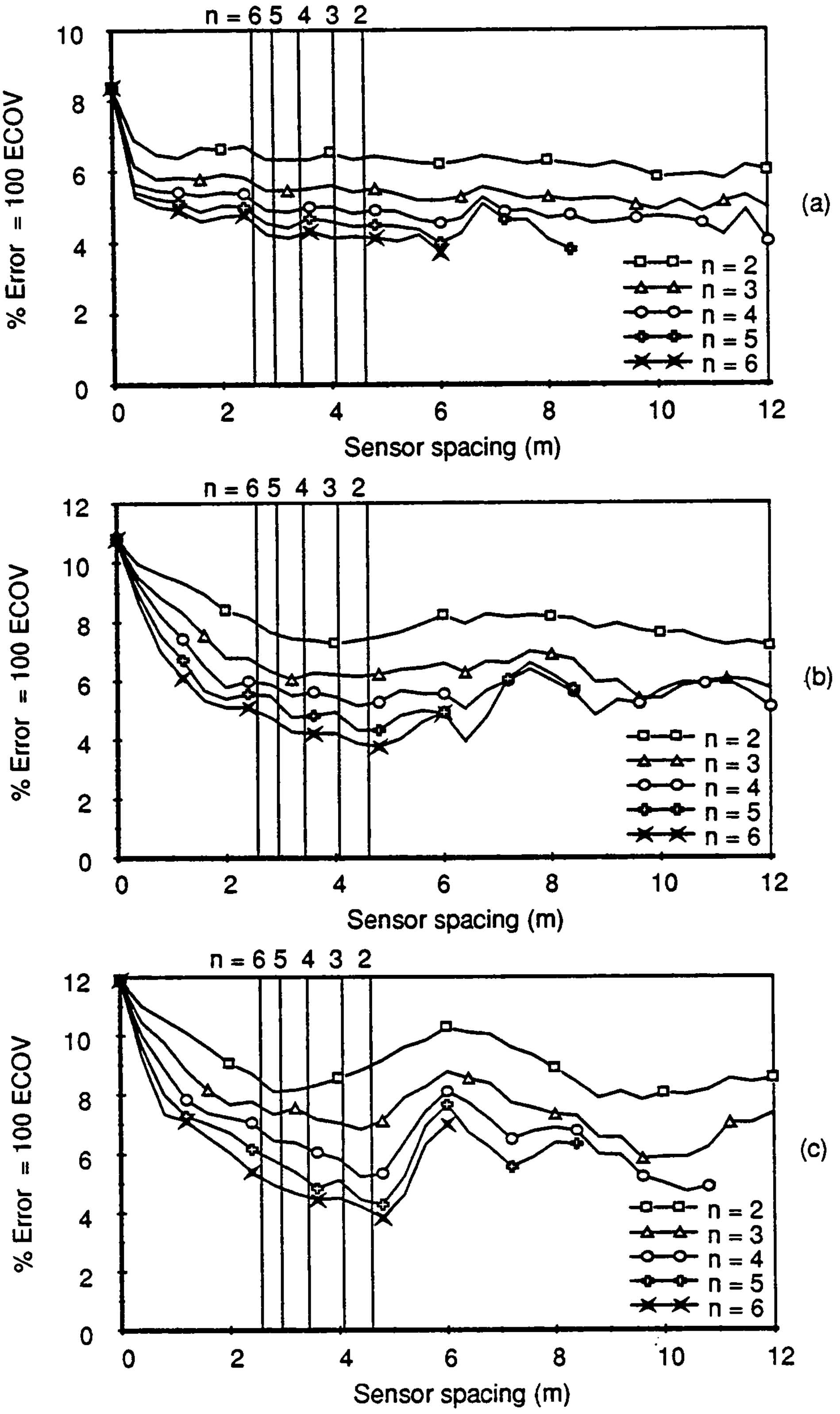

Fig. 5.41 WIM array error vs sensor spacing Vehicle S5,
Speed = 23.0 m/s (83 km/h) (a) Axle 1 (b) Axle 3 (c) Axle 5

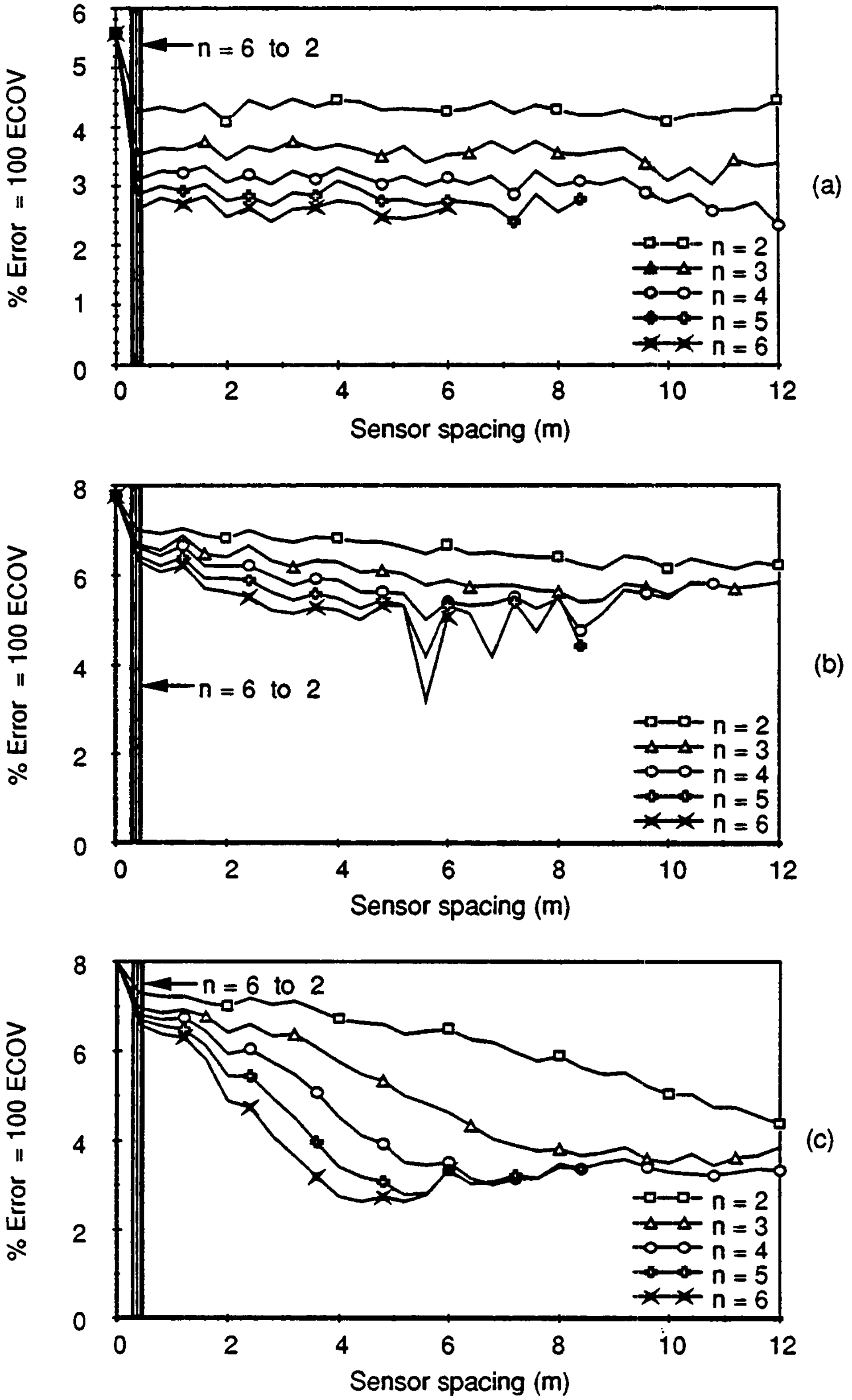

Fig. 5.42 WIM array error vs sensor spacing Vehicle S6,
Speed = 2.4 m/s (8.6 km/h) (a) Axle 1 (b) Axle 3 (c) Axle 5

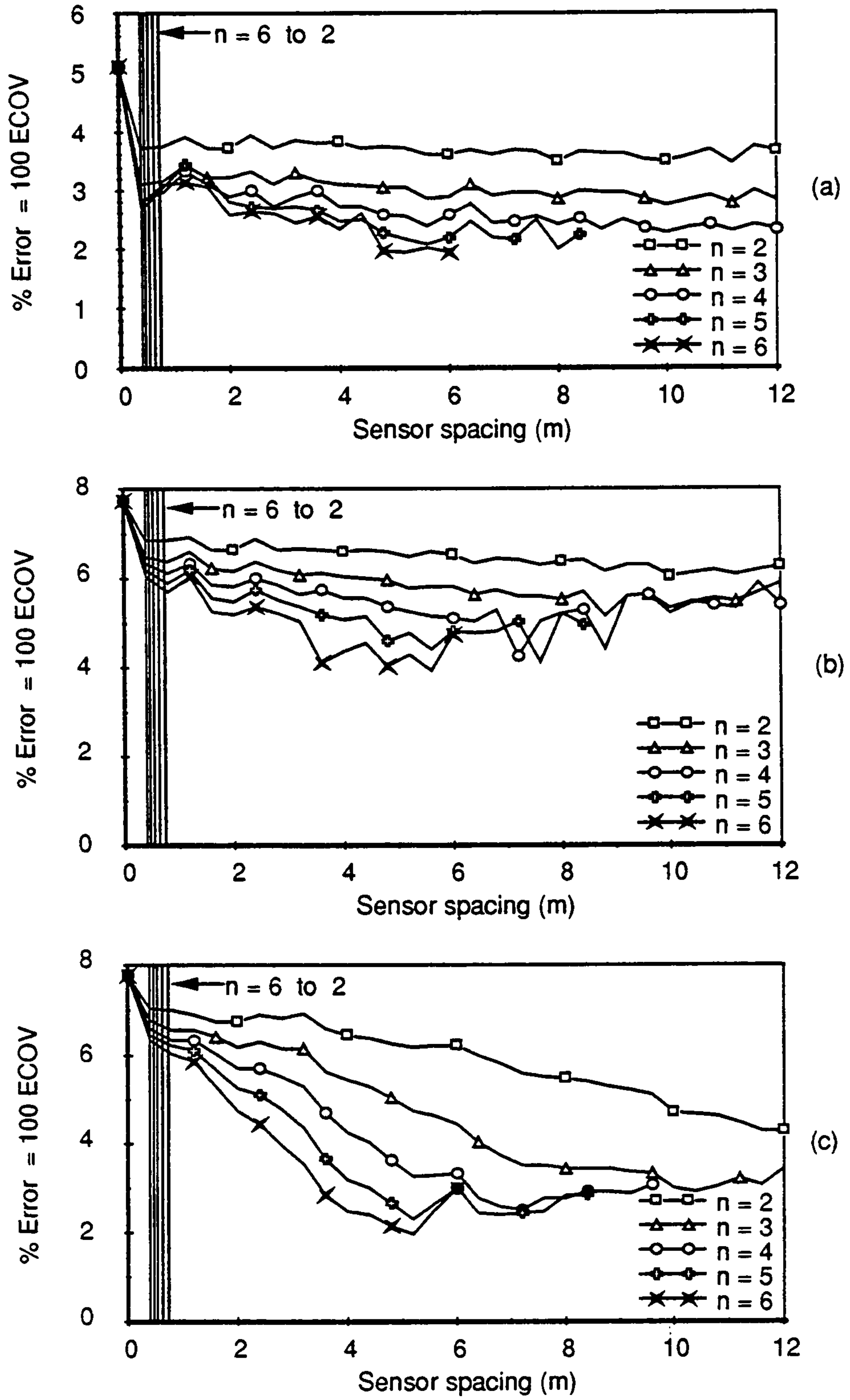

Fig. 5.43 WIM array error vs sensor spacing Vehicle S6,
Speed = 3.6 m/s (13 km/h) (a) Axle 1 (b) Axle 3 (c) Axle 5

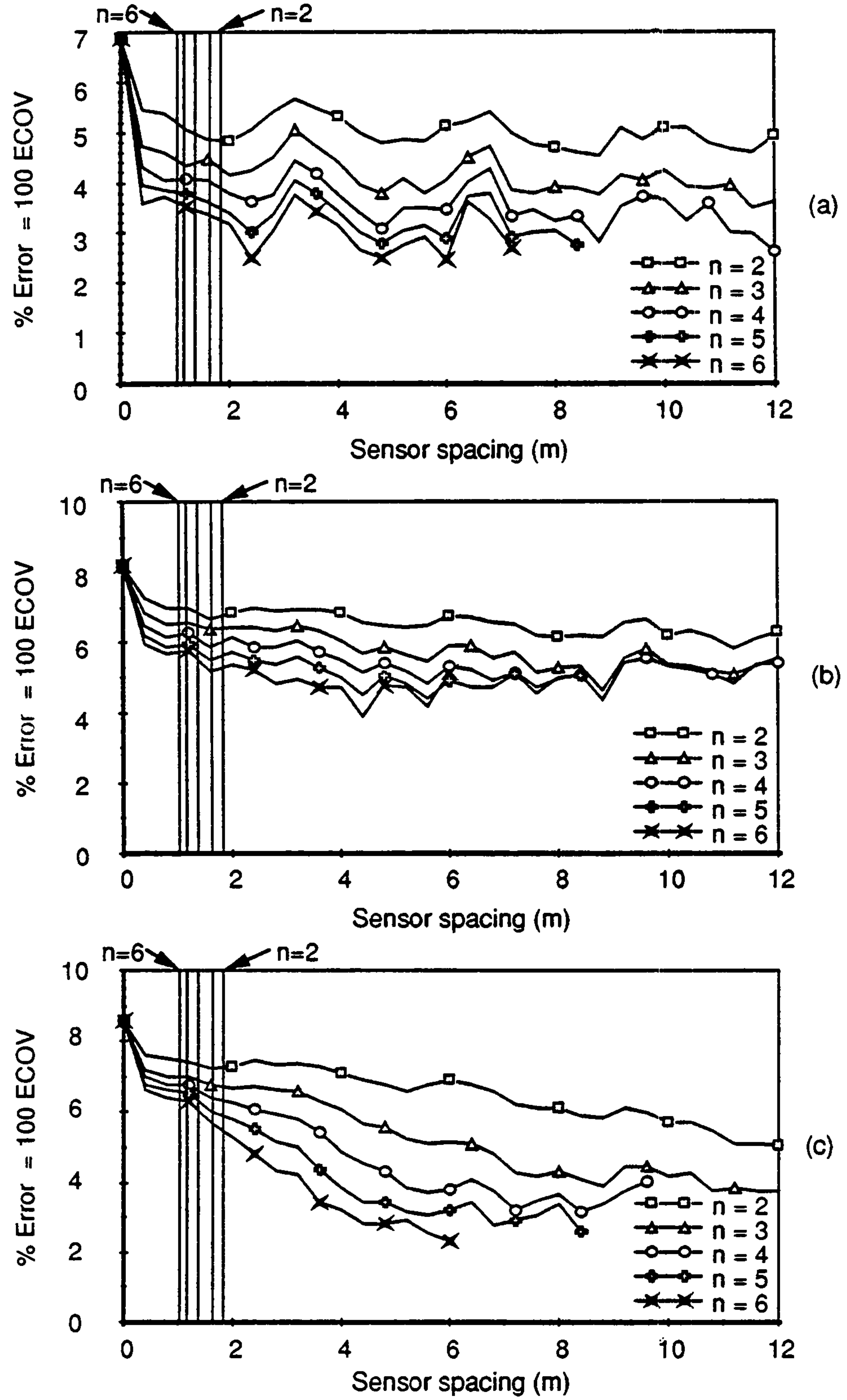

Fig. 5.44 WIM array error vs sensor spacing Vehicle S6,
Speed = 9.1 m/s (33 km/h) (a) Axle 1 (b) Axle 3 (c) Axle 5

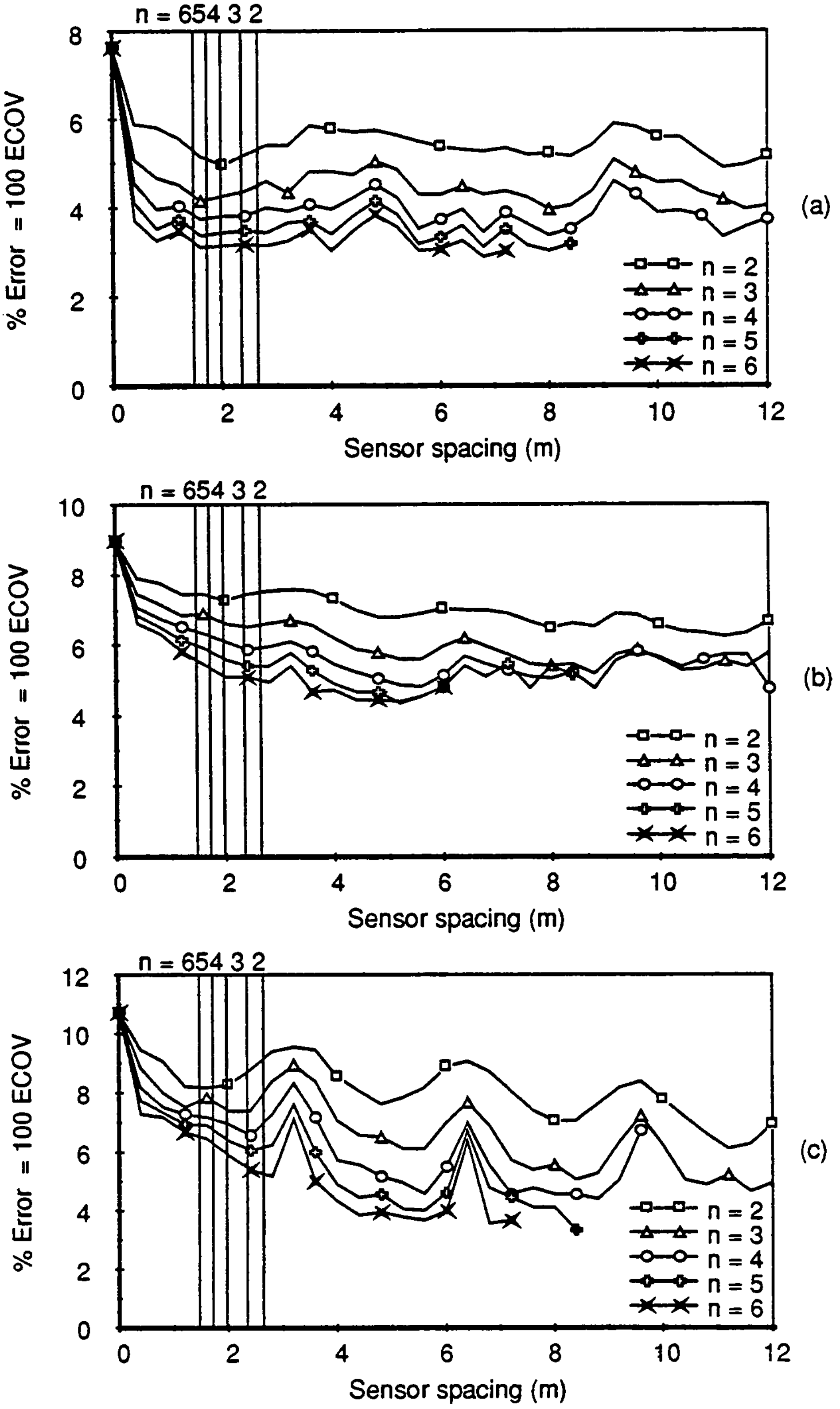

Fig. 5.45 WIM array error vs sensor spacing Vehicle S6,
Speed = 13.2 m/s (47 km/h) (a) Axle 1 (b) Axle 3 (c) Axle 5

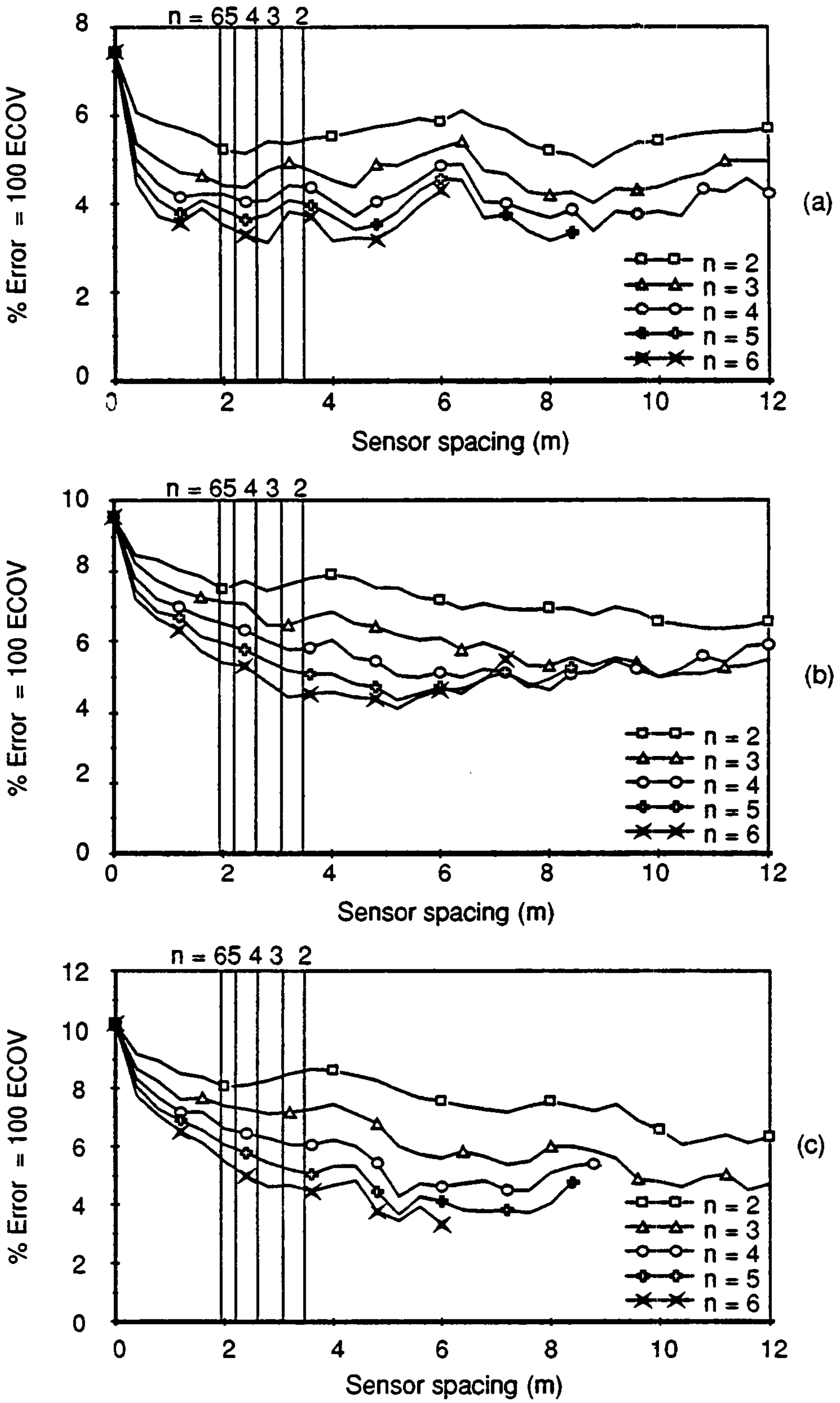

Fig. 5.46 WIM array error vs sensor spacing Vehicle S6,
Speed = 17.3 m/s (62 km/h) (a) Axle 1 (b) Axle 3 (c) Axle 5

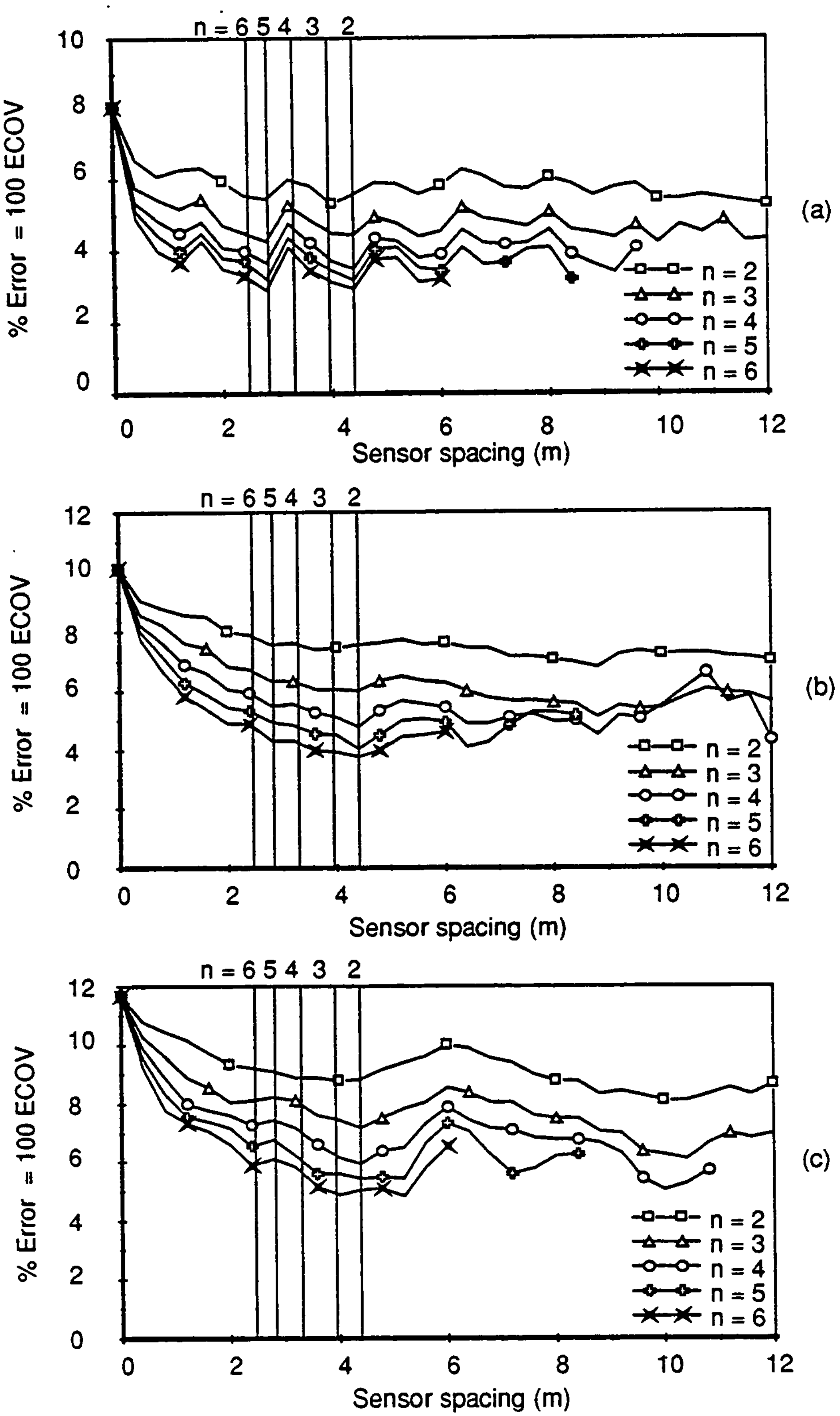

Fig. 5.47 WIM array error vs sensor spacing Vehicle S6,
Speed = 22 m/s (79 km/h) (a) Axle 1 (b) Axle 3 (c) Axle 5

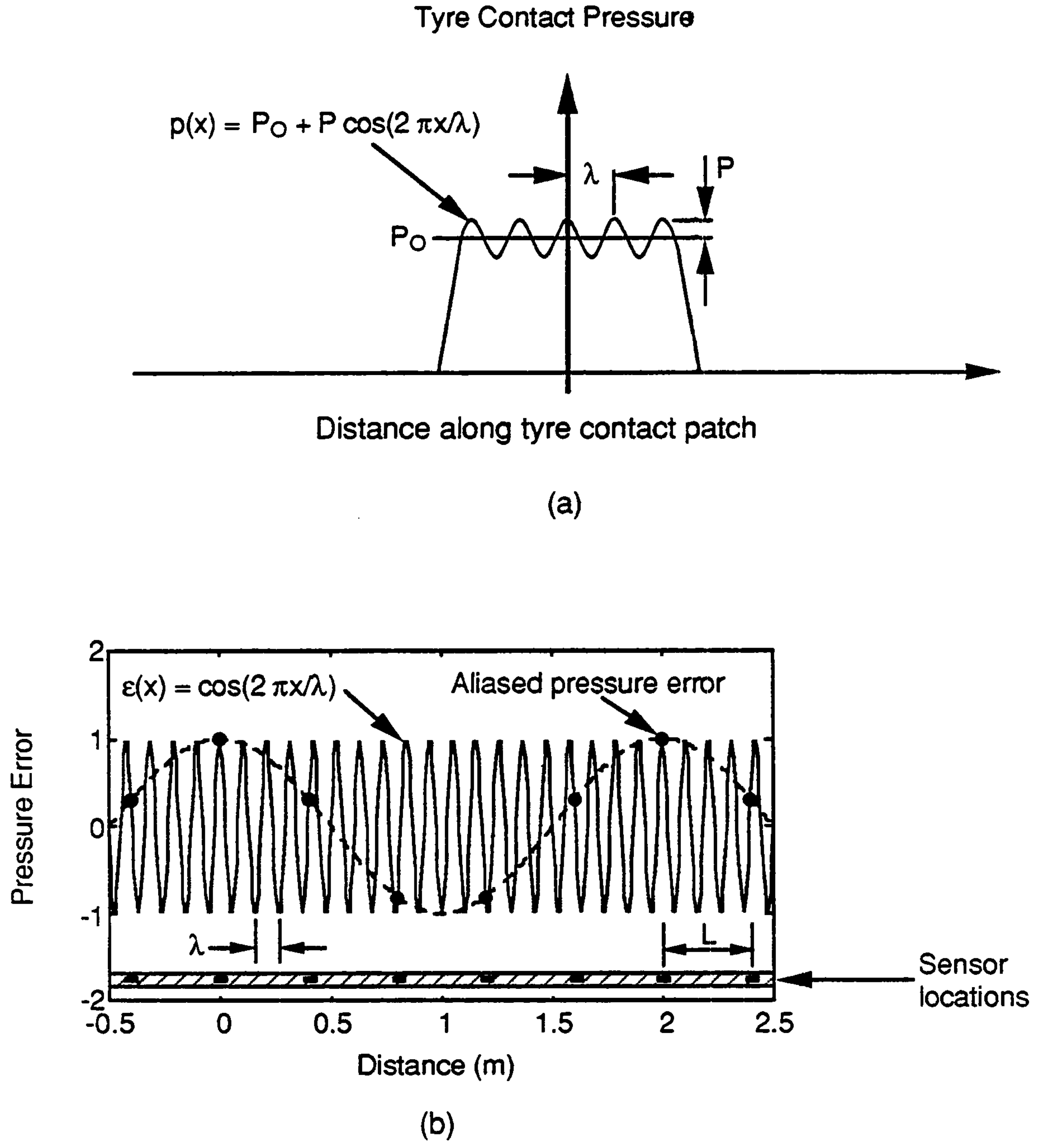

Fig 5.48 Illustrating the effect of undersampling (aliasing) the approximate pressure distribution under an off-road tyre.
(a) Sketch of contact pressure variation along the contact patch
(b) Sketch of peak pressure errors observed at various points along the mat surface as an off-road tyre rolls over, (eq. 5.8).

6

Overall Conclusions

Sensor Performance

(i) The calibration of the capacitative strip sensors in the load measuring mat was found to be independent of: (a) vehicle speed in the range 8-85 km/h, (b) mat surface temperature in the range 15-40 ^{o}C.

(ii) The sensor baseline random errors due to noise and calibration errors were found to be 4% RMS for a 26 kN steering tyre load.

(iii) The sensors were found to be inaccurate for tyres with an off-road tread pattern. This effect is a fundamental limitation of strip WIM sensor technology and is expected for any tyre of strip transducer.

(iv) Approximately 2.5% of all data was lost out of 612 test runs over the 96 sensors. Almost half of the lost data (1%) was due to a single sensor which failed. The remainder was due to false triggers of the data loggers. This level of data loss was considered to be satisfactory.

Vehicle Factors

(i) No evidence was found of fore-aft static load transfer due to vehicle speed.

(ii) Two of the test trailers were unevenly loaded, causing substantial differences between the static loads on the nearside and offside axles.

(iii) The static weighbridge measurements were inaccurate for individual axles of tandem groups with 4-spring suspensions.

Design of Multiple-Sensor WIM systems

(i) A good choice for the spacing between adjacent sensors in a multiple-sensor WIM system is given by

$$\Delta_{design} = \frac{2\,(n-1)\,\overline{V}}{\overline{f}\,n^2} \qquad (m) \qquad (4.22)$$

where

$\overline{V}$ = average traffic speed (m/s)
$\overline{f}$ = average frequency of dynamic wheel loads = 3 Hz for US vehicles
n = number of sensors in the array.

This result was derived from theoretical considerations and verified by the experiments.

(ii) The experimental results were found to agree quite closely with the theoretical models of multiple-sensor WIM system performance developed in this project.

(iii) Arrays with 3 or more evenly-spaced sensors will be more robust to speed and frequency variations than 2-sensor systems.

(iv) A good design choice is to use 3-sensor arrays which are likely to give RMS errors of 30-50% of the errors for single-sensor systems. In the near future it should be possible to measure routinely the static axle loads of vehicles travelling at highway speeds with RMS errors of approximately 5-8%. This is a considerable improvement over 12% to 20% for existing single-sensor WIM systems.

7

References

1. Trott JJ, Grainger JW. 'Design of a dynamic weighbridge for recording vehicle wheel loads.' TRRL Report LR219, 1968, TRRL, Crowthorne.
2. Prudhoe J. 'Slow speed dynamic axle weighers: effects of surface irregularities.' TRRL Research Report 134, 1988, TRRL, Crowthorne.
3. Salter DR, Davies P. 'Development and testing of a portable microprocessor-based weigh-in-motion system.' Transp. Res. Rec. 997, 1984, TRB, pp61-70.
4. Stewart PM. 'Low cost weigh-in-motion: Piezo-electric axle load sensors.' Proc. Seminar on Road Traffic Data Collection using Weigh-in-Motion, 1987, ARRB, Melbourne, Australia.
5. Moore RC et al. 'Piezo-electric axle load sensors.' Int. Conf. on Road Traffic Traffic Data Collection, 5-7 December, 1984, IEE Conference Publication No 242, pp40-46, IEE, London.
6. Cole DJ, Cebon D. 'A capacitative strip sensor for measuring dynamic tyre forces.' Proc. 2nd Int. Conf. on Road Traffic Monitoring. IEE, London, February 1989.
7. Cole DJ, Cebon D. 'Simulation and measurement of dynamic tyre forces.' Proc. 2nd Int. Conf. on Heavy Vehicle Weights and Dimensions, Kelowna, British Columbia, June, 1989.
8. Cole DJ. 'Report on the performance of the force measuring mat.' Unpublished, Cambridge University Engineering Department, 6 July 1989.
9. Sweatman PF. 'A study of dynamic wheel forces in axle group suspensions of heavy vehicles.' Australian Road Research Board Special Report SR27, 1983, 56 p.
10. Ervin RD, Nisonger RL, Sayers M, Gillespie TD, Fancher PS. 'Influence of truck size and weight variables on the stability and control properties of heavy trucks.' University of Michigan Report No. UMTRI-83-10/2, April 1983.

11. Mitchell CGB, Gyenes L. 'Dynamic pavement loads measured for a variety of truck suspensions.' Proc. 2nd Int. Conf. on Heavy Vehicle Weights and Dimensions, Kelowna, British Columbia, June 1989.

12. Woodrooffe JHF, LeBlanc PA, LePiane KR. 'Effects of suspension variations on the dynamic wheel loads of a heavy articulated highway vehicle.' Vehicle Weights and Dimensions Study, Vol. 11, Canroad Transportation Research Corporation, Canada, 1986.

13. Cebon D. 'Heavy vehicle vibration - a case study.' Proc. 9th IAVSD Symposium on the Dynamics of Vehicles on Roads and on Tracks, Linkoping, Sweden, 1985.

14. Heath A, Good MC. 'Heavy vehicle design parameters and dynamic pavement loading.' Australian Road Research 15(4), 1985, pp 249-263.

15. Morris JR. 'Effects of heavy vehicle characteristics on pavement response - phase 1.' Prepared for NCHRP project 1-25, TRB, December 1987.

16. Izadmehr B, Lee CE. 'Accuracy and tolerances of weigh-in-motion systems.' Transp. Res. Rec. 1123, TRB, 1987, pp127-135.

17. Glover MH. 'Weighing axles in motion with a multiple sensor system.' TRRL working paper WP VED/88/50, 1988. Crowthorne.

18. Newland DE. 'Random vibration and spectral analysis.' 2nd Edition, Longman, 1987.

19. Robson JD. 'Road surface description and vehicle response.' Int. J. of Vehicle Design, Vol. 1, No. 1, 1979.

20. Newland DE. 'General linear theory of vehicle response to random road roughness.' In: 'Random vibration - status and recent developments' Ed. Elishakoff I, Lyon RH, pp 303-326,Elsevier, 1986.

21. Cebon D. 'Theoretical road damage due to dynamic tyre forces of heavy vehicles: Part I - Dynamics of vehicles and road surfaces, Part II - Simulated damage caused by a tandem axle vehicle.' Proc. I. Mech. E., Vol. 202, No. C2, 1988.

22. Anon. 'Proposals for generalised road inputs to vehicles.' ISO/TC/108/WG9 draft 3e, May 1972.

23. Cebon D. 'Examination of the road damage caused by three articulated vehicles.' Proc. 10th IAVSD Symposium on the Dynamics of Vehicles on Roads and Tracks, Prague, August 1987.

24. Sayers, M, Gillespie, TD. 'The effect of suspension system nonlinearities on heavy truck vibration.' Proc. 7th IAVSD Symposium on the Dynamics of Vehicles on Roads and on Tracks, Cambridge, UK, 1981, pp 154-166.

25. Bendat, JS, Piersol, AG. 'Random data: Analysis and measurement procedures.' Wiley, 1971.

Appendix A

A Capacitative Strip Sensor for Measuring Dynamic Tyre Forces

by: DJ Cole and D Cebon

Reprinted from: Proc 2nd Int. Conf. on Road Traffic Monitoring. IEE, London, February 1989.

A CAPACITATIVE STRIP SENSOR FOR MEASURING DYNAMIC TYRE FORCES

D.J. Cole and D. Cebon

Cambridge University Engineering Department, UK.

SUMMARY

A novel capacitative strip sensor for measuring moving dynamic wheel forces has been designed, developed, and tested. The principle features of the sensor are linear response, insensitivity to loading width and pressure, and static calibration. The design of the sensor and the operation of the signal processing are described. The theoretical performance of the sensor is considered, and the results of full-scale tests using an instrumented lorry are presented.

1 INTRODUCTION

The work described in this paper arose out of research in Cambridge into the relationships between heavy vehicle design and road damage (for example see Cebon (1)). A vehicle travelling along a road surface will generate dynamic wheel forces which fluctuate around the static wheel force. Under highway conditions, these dynamic wheel forces typically have RMS amplitudes of approximately 30-40% of the static wheel forces, and are believed to be a significant cause of road damage. Previous investigators trying to relate road damage to dynamic forces have considered only average wheel force statistics (such as RMS values) of individual axles. Cebon (1) showed that it is necessary to measure the wheel forces generated by all axles of a vehicle and to relate them to particular locations along the road surface. It is difficult to perform a matrix of such measurements on a large number of vehicles using conventional vehicle mounted instrumentation, and therefore a system of measuring wheel forces using 'weigh-in-motion' (WIM) equipment placed on the road surface was developed.

The equipment consists of a tough polymer mat, made up from tiles 1.2m square and 13mm thick, each containing three novel force sensors laid transverse to the wheel path at a longitudinal separation of 0.4m. The tiles are laid end to end to give the required length of mat (typically 50-100m). The primary advantage of the wheel force measuring mat is that many uninstrumented vehicles can be tested rapidly. This allows a large parametric study of vehicle design variables to be performed cheaply. The design and performance of the force sensors and their signal conditioning are described in this paper.

Most existing WIM installations are intended to determine static axle weights, but because of the vehicle dynamics the forces measured are not the true static forces, except at very low speeds. The equipment described in this paper is intended to measure the true wheel forces (static+dynamic) as accurately as possible. In applications where the static forces are needed, it will be necessary to provide several sensors and suitable data processing to determine the static forces from several measurements of the true wheel forces.

2 REVIEW OF EXISTING WEIGH-IN-MOTION TECHNOLOGY

The principle design requirement of the mat was to measure wheel forces accurately at 0.4m intervals along the road for a distance of 50-100m. It was also necessary for the mat to be portable, so that vehicles could be tested on a variety of road surfaces.

The design work began with a feasibility study, including a review of existing WIM technology. The WIM systems evaluated included: weighbeams (Trott and Grainger (2), Prudhoe (3)), piezo-electric cables (Stewart (4), Moore (5)), piezo-electric film (PVdF) (Davies and Somerville (6), Cole and Hardy (7)), and capacitative pads (Salter and Davies (8)). The systems were assessed in terms of their linearity, dynamic response, sensitivity to contact area and pressure, temperature sensitivity, uniformity, and ease of installation and calibration. Where data was not available, laboratory tests were performed on material samples.

The feasibility study concluded that none of the existing systems satisfied the accuracy and installation requirements. The study did, however, point the way to the development of a novel capacitative strip sensor which is described in detail in the next section. The concept of the capacitative strip is to monitor the capacitance between two narrow electrodes (approximately 30mm wide and 1.0-1.5m long), which deflect elastically under load. Providing the electrodes are supported by a stable, linear elastic, and uniform material (such as an engineering metal), of constant cross-section, it is possible to obtain an output which is directly proportional to the local tyre contact pressure.

3 CAPACITATIVE STRIP SENSOR

3.1 Design

The main component of the sensor is a hollow high strength aluminium extrusion with cross-sectional dimensions approximately 10mm x 30mm. The top surface of the extrusion deflects when a tyre rolls over the strip, causing a change of capacitance within the strip. The wheel force is determined by measuring the magnitude and duration of the capacitance change. A schematic cross-section of the sensor is shown in figure 1. The shape of the extrusion was designed with the aid of finite element analysis to achieve a suitable compromise between sensitivity and strength. Tests to determine tyre contact pressures were performed on a strain gauged prototype extrusion using a laden vehicle. The tests also confirmed that the influence of a tyre on the sensor away from the contact area is very small; this means that the sensitivity to tyre width is low.

The extrusion contains an inner copper electrode which acts as one plate of the capacitor, the other plate being the extrusion. The air gap between the electrode and the extrusion is maintained to close tolerance, thus ensuring minimum sensitivity variation along the length of the sensor.

The primary signal conditioning circuit for the sensor is contained within one end of the extrusion. This is made possible by the use of small 'surface-mount' components. End caps are fitted to each end of the extrusion to provide an environmental seal and prevent excessive deformation of the ends, which are inherently weaker than the rest of the extrusion.

The longitudinal flexibility of the extrusion is such that the sensor will conform to road camber, but not to deep ruts. The sensor can be of any reasonable length; current applications require lengths of 1.2m or 1.5m for measurement of tyre forces along one wheel path.

Tests in the laboratory showed the sensor to have low sensitivity to temperature changes and to lengthwise bending, and to have sensitivity variation along the length typically less than ±2%.

3.2 Signal Processing

The output signal of the sensor is fed into a local data-logging box. Each box can deal with up to twelve sensors. The box contains secondary signal conditioning, and a microprocessor to perform data processing. The measured wheel force values are stored in the microprocessor's memory, and can be transferred to a portable computer by a serial link (RS232). When more than twelve sensors are used, data logging boxes can be 'daisy-chained' together.

In common with all narrow strip sensors the output must be integrated throughout the duration of the tyre contact, and the vehicle speed must be measured, in order to determine the total wheel force. The integration is performed within the data-logging boxes. When two or more sensors are being used, spaced along the road, the vehicle speed can be determined from the arrival times of an axle at each sensor. If only one sensor is present, and the axle separation or vehicle speed is not known, additional instrumentation must be used to allow the speed to be measured.

The calibration factor is determined by measuring the output of the sensor when a known pressure is applied to a known length of the strip. This operation can be performed statically; it is not necessary to apply an impulse or a moving wheel force. A calibrator has been developed which allows pressure from a hand operated hydraulic pump to be applied to any 200mm length section of a sensor. It is possible to measure the variation in sensitivity along the length, and to give each sensor a calibration factor during manufacture.

A second type of calibrator allows encapsulated sensors to be calibrated. The calibrator is placed on the mat directly above a sensor, and a large mass (such as the front wheel of a lorry) is placed (or driven) on top to react the force from the hydraulic pressure, which is again provided by a hand pump (figure 2).

3.3 Theoretical Performance

The theoretical performance of the sensor has been investigated extensively, and the known quantifiable sources of inaccuracy are described in the next sections. There are of course additional small random errors associated with calibration, data processing, and environmental effects.

<u>3.3.1 Bit error.</u> The passage of a wheel over the sensor results in a digital output which is proportional to (wheel force/vehicle speed). For example, a wheel force of 40kN travelling at 20m/s causes an output of approximately 250. A one bit error in the output results in a 0.4% error of the measured force. The error is proportional to (vehicle speed/wheel force), and thus the greatest errors occur for small wheel forces travelling at high speed.

<u>3.3.2 Smoothing error.</u> Strip sensors cannot measure wheel forces instantaneously, because the entire tyre contact patch must move over the sensor before the force can be calculated. If the wheel force varies significantly during contact with the sensor, the measured force will be an average of the instantaneous forces of the wheel (figure 3a). Figure 3b shows the measurement error, due to smoothing, of a wheel force consisting of a static component and a sinusoidal dynamic component. The two groups of lines are for a 3Hz and a 15Hz dynamic component (representing vehicle sprung mass bounce and axle hop respectively). The lines in each group represent different ratios (α) of dynamic to static force amplitude. The error shown is calculated for the case when the dynamic component of the wheel force is at its minimum, as in figure 3a (the worst case). The smoothing effect is greatest for low vehicle speeds, high frequency force components, and large ratios of dynamic to static force. These conditions do not usually occur simultaneously because the higher frequency (wheel hop) modes of vehicle suspensions are only excited significantly at high speeds on normal roads (Cole and Cebon (9)). This error, which occurs for <u>all</u> strip sensors, is expected to be approximately 1.5% in typical WIM applications at highway speeds.

<u>3.3.3 Random error.</u> The sensor is not perfectly noise free, and therefore some random noise is present on the output. The error can be quantified by measuring the standard deviation (RMS) of the no-load output. At the present stage of development the RMS error caused by the electrical noise is about 2%; it is hoped that this can be improved.

<u>3.3.4 Contact pressure and width.</u> If the tyre contact pressure acted over the entire length of the strip then the sensor output would theoretically be linear. In practice, the wheel force affects only a proportion of the total capacitance because the tyre contact width is less than the total length of the sensor, and because some of the total capacitance is due to the space below the inner electrode. The constant component of the total capacitance is known as the 'dead capacitance'. The presence of the dead capacitance causes a slight nonlinearity in the sensor, and because the amount of dead capacitance depends on the loaded width, there is a slight sensitivity to tyre contact width. The effects can be calculated, and for the expected range of contact pressures and widths, the error introduced is less than 1.0%.

4 EXPERIMENTAL PERFORMANCE

4.1 Description of the Prototype Tile

A prototype tile containing three sensors (numbered 1 to 3) was tested on a test track using an instrumented lorry. Unfortunately the prototype sensor extrusions had a slightly incorrect internal shape, because of an error by the die maker. This error prevented reliable location of the internal components and therefore changes in sensitivity with use were possible. The die has now been corrected.

4.2 Description of the Test Vehicle

The test vehicle was a two axle rigid lorry, fully laden to a gross weight of 16 tonnes. The front axle was fitted with single tyres, and the rear axle with dual tyres. Strain gauges and accelerometers were fitted to both axles in order to measure the dynamic component of wheel force; the static force was measured statically with weigh plates. The position of the lorry relative to the mat was determined by means of an infra-red transceiver mounted on the front axle of the lorry. The transceiver detected a reflective strip on the road surface, so that an event pulse occurred when the rear wheel was directly above the middle sensor. The outputs from the instruments on the vehicle were recorded using an FM tape recorder.

4.3 Description of the Tests

The mat was placed on the nearside wheel path of a long straight section of the test track. The only attachment of the mat to the road was a strip of bituminous tape laid over the leading edge of the mat; there were no lead-in or lead-out ramps. The nearside wheels of the lorry were driven over the mat twenty times, at speeds from 8km/h to 65km/h.

4.4 Data Processing - Lorry

The data recorded from the lorry was digitised using a data logger, and then transferred onto a mainframe computer for processing. The wheel force time history was calculated as the sum of the static weight, the strain gauge force, and the linear and angular inertia corrections for the mass outboard of the strain gauge (see (9) for details).

4.5 Data Processing - Sensors

The vehicle speed was calculated from the wheelbase and the arrival times of the front and rear axles at each sensor.

There was close agreement between the calibration factors measured before and after the tests for sensors 1 and 3, and the variation in sensitivity along each strip was less than ±0.8%. However, the calibrations of sensor 2 before and after the tests differed by about 10%, and the sensitivity varied along the length by up to ±10%. This was probably due to the incorrect extrusion shape (section 4.1). For this reason the results from sensor 2 were excluded from the analysis.

TABLE 1 - Results for sensors 1 and 3

Sensor	Std. Deviation of Error / %	Calibration Error / %
1	9.1	10.8
3	8.7	14.7
1&3	9.0	12.7

4.6 Analysis of Results

Figure 4 compares the forces measured by sensor 1 and by the lorry, and figure 5 shows the frequency distribution of the errors. The standard deviations and calibration errors for sensors 1 and 3 are given in table 1. The error is defined as:
((sensor force - lorry force)/lorry force)100 .

The lorry instrumentation and the sensor both contribute to the error. Unfortunately it has not been possible to estimate the error caused by the lorry instrumentation alone, because the two dynamic force components are different for every measurement. The effect of systematic error will therefore be different for every measurement, and appear to be a random error. Conventional error bars cannot be drawn because this would ignore the systematic nature of the error. It is clear that the calibration errors cannot be accounted for totally by the lorry measurement. Work has since taken place to improve the accuracy of the calibration procedure.

Part of the random error is caused by the oscillator noise (approximately 2% RMS). Another source of random error in the measurement by the sensor is thought to be variation in tread pattern around the circumference of the tyre. If this is the case, the output of the sensor would depend on the alignment of the tread pattern to the sensor. This effect is currently being studied further. At the time of writing the first 10m of a 50m mat are being installed. The initial tests on this mat will further quantify the accuracy of the sensor alone.

6 CONCLUSIONS

i) A novel capacitative strip force sensor for measuring moving dynamic wheel forces has been designed, developed, and tested.

ii) The principle features of the sensor are:
   - Insensitive to loading width and position
   - Linear response with low sensitivity to temperature and forcing frequency
   - Can be calibrated statically, both in the factory and in the field
   - Suitable for temporary or permanent (buried) installation

iii) In the first testing programme the standard deviation of the combined error of the lorry and prototype mat measurements was about 9%, and the calibration error was up to 14.7%.

iv) A number of further tests are planned to quantify the accuracy of the sensor alone.

REFERENCES

1. Cebon,D., 1988, "Theoretical road damage due to dynamic tyre forces of heavy vehicles. Part 1: dynamic analysis of vehicles and road surfaces. Part 2: simulated damage caused by a tandem-axle vehicle", Proc. Instn. Mech. Engrs., 202, 103-117.

2. Trott,J.J. and Grainger,J.W., 1968, "Design of a dynamic weighbridge for recording vehicle wheel loads", TRRL Report LR219, TRRL, Crowthorne.

3. Prudhoe,J., 1988, "Slow speed dynamic axle weighers: effects of surface irregularities", TRRL Research Report 134, TRRL, Crowthorne.

4. Stewart,P.M., 1987, "Low cost weigh-in-motion: Piezoelectric cable systems - current practice and research directions", Proc. Seminar on Road Traffic Data Collection Using Weigh-in-Motion, ARRB, Melbourne, Victoria.

5. Moore,R.C. et al, 1984, "Piezo-electric axle load sensors", International Conference on Road Traffic Data Collection, 5-7 December 1984, IEE Conference Publication No.242, p40-46, IEE, London.

6. Davies,P. and Somerville,F.K., 1986, "Low cost axle load determination", 13th ARRB - 5th REAAA Combined Conference, 25-29 August 1986, Volume 13 - Proceedings - Part 6, p142-149, ARRB, Victoria.

7. Cole,D.J. and Hardy,M.S.A., 1987, "A feasibility study into a wheel force sensing mat", Department of Engineering, University of Cambridge.

8. Salter,D.R. and Davies,P., 1984, "Development and testing of a portable microprocessor-based capacitative weigh-in-motion system", Transportation Research Record 997, Transportation Research Board, 61-70.

9. Cole,D.J. and Cebon,D., 1988, "Simulation and measurement of vehicle response to road roughness", Proc. Inst. of Acoustics, 10, 477-484.

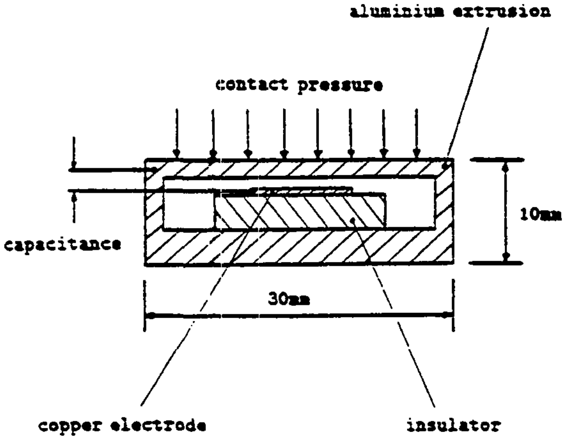

Figure 1. Schematic cross-section of force sensor

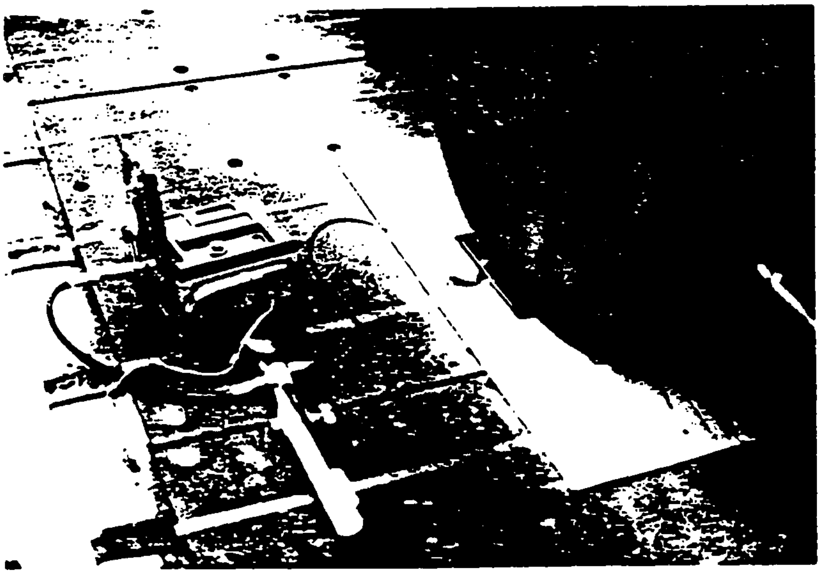

Figure 2. The calibrating equipment placed on the wheel force measuring mat

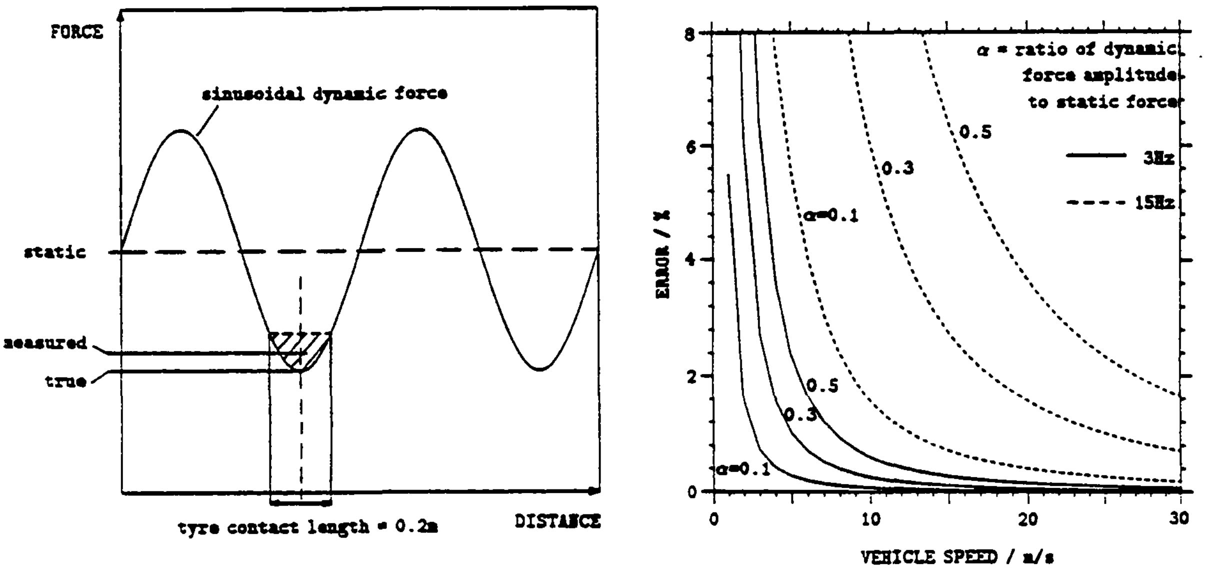

(a)

(b)

Figure 3. Smoothing error

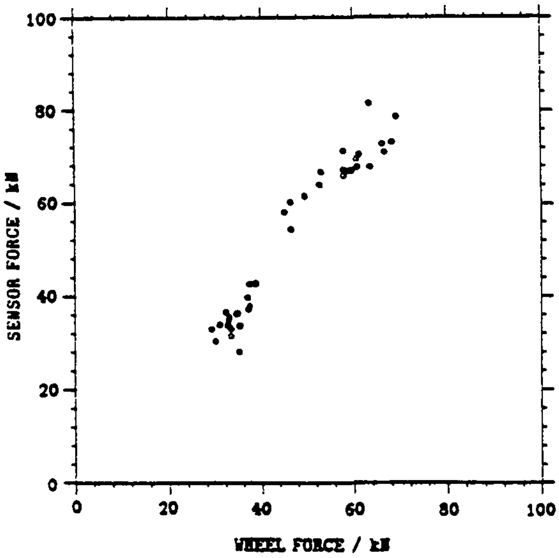

Figure 4. Force measured by sensor 1 against force measured by lorry

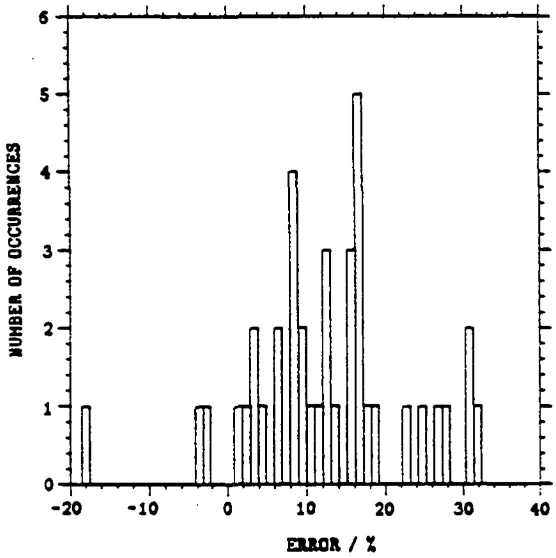

Figure 5. Distribution of errors for sensor 1

Appendix B

Vehicle Data Sheets

Vehicle	**S1**
Tractor Description	**Navistar cab over, 6x4 (CO 9670), 4-spring drive suspension**
Trailer Description	**Fruehauf Van (Navistar #44), 4-spring suspension**
GVW	**321.93 kN (72 360 lbs)**
Test Date	**29 Sept 1989**

Axle Data

Axle No	*Suspension type*	*Static load (kN)(1)*	*Spacing from Preceding Axle (m)*	*Tyre type(2)*	*Tyre pressure (psi) (4)*
1	3-leaf shocks	44.80	0	Single 275/80R24.5	107 OS 100 NS
2	4-spring tandem Multileaf, no shocks	72.65	3.38	Dual 275/80R24.5	102 OS 96 NS
3	4-spring tandem Multileaf, no shocks	66.38	1.31	Dual 275/80R24.5	74 OS 96 NS
4	4-spring tandem Multileaf, no shocks	63.22	8.32	Dual(3) 10R20	
5	4-spring tandem Multileaf, no shocks	74.88	1.25	Dual 10R20	

Notes:

1. Total axle load
2. Tyres had highway tread pattern unless otherwise noted
3. Trailer tyres had bad flat spots due to previous braking tests
4. OS = Off side (Drivers side) NS = Near side (Passenger side)

Vehicle	**S2**
Tractor Description	**Freightliner cab over, 6x4 (Navistar #E-817)** **4-spring drive suspension**
Trailer Description	**Fruehauf Van (Navistar #44), 4-spring suspension**
GVW	**327.53 kN (73 620 lbs)**
Test Date	**6 Oct 1989**

Axle Data

Axle No	*Suspension type*	*Static load (kN)*	*Spacing from Preceding Axle (m)*	*Tyre type*	*Tyre pressure (psi)*
1	3-leaf shocks	43.56	0	Single 11R24.5	80 OS 85 NS
2	4-spring tandem 4-leaves, no shocks	72.56	3.70	Dual 11R24.5	82 OS 85 NS
3	4-spring tandem 4-leaves, no shocks	72.03	1.33	Dual 11R24.5	80 OS 85 NS
4	4-spring tandem Multileaf, no shocks	65.58	8.43	Dual(1) 10R20	
5	4-spring tandem Multileaf, no shocks	73.81	1.25	Dual 10R20	

Notes:

1. Trailer tyres had bad flat spots

Vehicle	**S3**
Tractor Description	**Navistar cab over, 6x4 (CO9670), 4-spring drive suspension**
Trailer Description	**Flat bed, (Navistar #46) 'single-point' pivotted spring**
GVW	**295.32 kN (66 380 lbs)**
Test Date	**12 Oct 1989**

Axle Data

Axle No	*Suspension type*	*Static load (kN)*	*Spacing from Preceding Axle (m)*	*Tyre type*	*Tyre pressure (psi)*
1	3-leaf shocks	46.58	0	Single 275/80R24.5	107 OS 100 NS
2	4-spring tandem Multileaf, no shocks	79.68	3.38	Dual 275/80R24.5	102 OS 96 NS
3	4-spring tandem Multileaf, no shocks	76.30	1.31	Dual 275/80R24.5	74 OS 96 NS
4	Pivotted multileaf tandem, no shocks	46.67	8.14	Dual 11.00-20 Cross ply	74 OS 72 NS
5	Pivotted multileaf tandem, no shocks	46.09	1.31	Dual 11.00-20 Cross ply	82 OS 74 NS

Vehicle	**S4**
Tractor Description	**Navistar cab over, 6x4 (CO9700), Air drive suspension**
Trailer Description	**Fruehauf Van (Navistar #25), 4-spring suspension**
GVW	**323.0 kN (72 600 lbs)**
Test Date	**12 Oct 1989**

Axle Data

Axle No	*Suspension type*	*Static load (kN)*	*Spacing from Preceding Axle (m)*	*Tyre type*	*Tyre pressure (psi)*
1	3-leaf shocks	51.12	0	Single 11R22.5	94 OS 94 NS
2	Air tandem (trailing arm) with shocks	76.17	2.94	Dual 11R22.5 Lug tread	96 OS 94 NS
3	Air tandem (trailing arm) with shocks	74.43	1.31	Dual 11R22.5 Lug tread	92 OS 94 NS
4	4-spring tandem 3-leaves, no shocks	64.73	8.46	Dual 285/75R24.5	106 OS 100 NS
5	4-spring tandem 3-leaves, no shocks	56.55	1.24	Dual 285/75R24.5	92 OS 104 NS

Vehicle	**S5**
Tractor Description	**Freightliner cab over, 6x4 (Navistar #E-817)** **4-spring drive suspension**
Trailer Description	**Fruehauf Van (Navistar #25), 4-spring suspension**
GVW	**323.17 kN (72 640 lbs)**
Test Date	**13 Oct 1989**

Axle Data

Axle No	*Suspension type*	*Static load (kN)*	*Spacing from Preceding Axle (m)*	*Tyre type*	*Tyre pressure (psi)*
1	3-leaf shocks	43.16	0	Single 11R24.5	80 OS 85 NS
2	4-spring tandem 4-leaves, no shocks	79.41	3.70	Dual 11R24.5	82 OS 85 NS
3	4-spring tandem 4-leaves, no shocks	79.50	1.33	Dual 11R24.5	80 OS 85 NS
4	4-spring tandem 3-leaves, no shocks	54.50(1)	8.43	Dual 285/75R24.5	106 OS 100 NS
5	4-spring tandem 3-leaves, no shocks	66.60	1.21	Dual 285/75R24.5	92 OS 104 NS

Notes:

1. Weighbridge measurements for axles 4 and 5 showed inconsistencies: static loads may be unreliable.

Vehicle	**S6**
Tractor Description	**Navistar cab over, 6x4 (CO9670), 4-spring drive suspension**
Trailer Description	**Fruehauf Van (Navistar #25), 4-spring suspension**
GVW	**316.95 kN (71 240 lbs)**
Test Date	**13 Oct 1989**

Axle Data

Axle No	*Suspension type*	*Static load (kN)*	*Spacing from Preceding Axle (m)*	*Tyre type*	*Tyre pressure (psi)*
1	3-leaf shocks	45.87	0	Single 275/80R24.5	107 OS 100 NS
2	4-spring tandem Multileaf, no shocks	76.30	3.38	Dual 275/80R24.5	102 OS 96 NS
3	4-spring tandem Multileaf, no shocks	73.81	1.31	Dual 275/80R24.5	74 OS 96 NS
4	4-spring tandem 3-leaves, no shocks	58.77	8.31	Dual 285/75R24.5	106 OS 100 NS
5	4-spring tandem 3-leaves, no shocks	62.20	1.25	Dual 285/75R24.5	92 OS 104 NS

Appendix C

Matrix of Vehicle Tests

Test Runs - Articulated Vehicles

Vehicle Code	*Direction*	*Speed (mph)*	*No Runs*	*File Names*
S1	R	5	20	S1R0501-S1R0520
S1	R	10	6	S1R1001-S1R1006
S1	R	20	7	S1R2001-S1R2007
S1	R	30	6	S1R3001-S1R3006
S1	R	40	6	S1R4001-S1R4006
S1	R	50	6	S1R5001-S1R5006
S1	F	5	6	S1F0501-S1F0506
S1	F	10	6	S1F1001-S1F1006
S1	F	20	6	S1F2001-S1F2006
S1	F	30	6	S1F3001-S1F3006
S1	F	40	6	S1F4001-S1F4006
S1	F	50	6	S1F5001-S1F5006
S2	R	5	6	S2R0501-S2R0506
S2	R	10	6	S2R1001-S2R1006
S2	R	20	6	S2R2001-S2R2006
S2	R	30	6	S2R3001-S2R3006
S2	R	40	7	S2R4001-S2R4007
S2	R	50	6	S2R5001-S2R5006
S2	F	5	6	S2F0501-S2F0506
S2	F	10	7	S2F1001-S2F1007
S2	F	20	7	S2F2001-S2F2006
S2	F	30	6	S2F3001-S2F3006
S2	F	40	6	S2F4001-S2F4006
S2	F	50	6	S2F5001-S2F5006

Note:

F = 'Forward' direction around the test track (Anti-clockwise), R = 'Reverse' direction.

Test Runs - Articulated Vehicles

Vehicle Code	*Direct-ion*	*Speed (mph)*	*No Runs*	*File Names*
S3	R	5	6	S3R0501-S3R0506
S3	R	10	7	S3R1001-S3R1007
S3	R	20	6	S3R2001-S3R2006
S3	R	30	6	S3R3001-S3R3006
S3	R	40	6	S3R4001-S3R4006
S3	R	50	7	S3R5001-S3R5007
S3	F	5	6	S3F0501-S3F0506
S3	F	10	7	S3F1001-S3F1007
S3	F	20	6	S3F2001-S3F2006
S3	F	30	7	S3F3001-S3F3007
S3	F	40	7	S3F4001-S3F4007
S3	F	50	6	S3F5001-S3F5006
S4	R	5	6	S4R0501-S4R0506
S4	R	10	6	S4R1001-S4R1006
S4	R	20	6	S4R2001-S4R2006
S4	R	30	6	S4R3001-S4R3006
S4	R	40	6	S4R4001-S4R4006
S4	R	50	6	S4R5001-S4R5006
S4	F	5	6	S4F0501-S4F0506
S4	F	10	6	S4F1001-S4F1006
S4	F	20	6	S4F2001-S4F2006
S4	F	30	6	S4F3001-S4F3006
S4	F	40	6	S4F4001-S4F4006
S4	F	50	6	S4F5001-S4F5006

Test Runs - Articulated Vehicles

Vehicle Code	*Direct-ion*	*Speed (mph)*	*No Runs*	*File Names*
S5	R	5	7	S5R0501-S5R0507
S5	R	10	6	S5R1001-S5R1006
S5	R	20	6	S5R2001-S5R2006
S5	R	30	7	S5R3001-S5R3007
S5	R	40	6	S5R4001-S5R4006
S5	R	50	6	S5R5001-S5R5006
S5	F	5	6	S5F0501-S5F0506
S5	F	10	6	S5F1001-S5F1006
S5	F	20	6	S5F2001-S5F2006
S5	F	30	6	S5F3001-S5F3006
S5	F	40	6	S5F4001-S5F4006
S5	F	50	6	S5F5001-S5F5006
S6	R	5	7	S6R0501-S6R0507
S6	R	10	6	S6R1001-S6R1006
S6	R	20	6	S6R2001-S6R2006
S6	R	30	6	S6R3001-S6R3006
S6	R	40	6	S6R4001-S6R4006
S6	R	50	6	S6R5001-S6R5006
S6	F	5	7	S6F0501-S6F0507
S6	F	10	6	S6F1001-S6F1006
S6	F	20	7	S6F2001-S6F2006
S6	F	30	6	S6F3001-S6F3006
S6	F	40	6	S6F4001-S6F4006
S6	F	50	6	S6F5001-S6F5006

Test Runs - Mobile Tyre Tester					
Vehicle Code	*Direct-ion*	*Nominal Load (lbs)*	*Speed (mph)*	*No. Runs*	*File Names*
MSH	F	4000	5	15	MSH40501-MSH40515
MSH	F	4000	20	6	MSH42001-MSH42006
MSH	F	4000	40	6	MSH44001-MSH44006
MSH	F	4000	50	6	MSH45001-MSH45006
MSH	F	8000	5	25	MSH80501-MSH80525
MSH	F	8000	10	6	MSH81001-MSH81006
MSH	F	8000	20	6	MSH82001-MSH82006
MSH	F	8000	30	6	MSH83001-MSH83006
MSH	F	8000	40	7	MSH84001-MSH84007
MSH	F	8000	50	6	MSH85001-MSH85006
MSL	F	8000	5	15	MSL80501-MSL80515
MD	F	5000	5	7	MD50501-MD50507
MD	F	5000	30	6	MD53001-MD53006
MD	F	5000	50	6	MD55001-MD55006
MD	F	8000	5	5	MD80501-MD80505
MD	F	10000	5	6	MD100507-MD100512
MD	F	10000	20	6	MD102007-MD102012
MD	F	10000	40	6	MD104007-MD104012
MD	F	10000	50	6	MD105005-MD105010

Notes:

1. Total Number of runs (all tests) = 612
2. MSH = Mobile, Single tyre, Highway tread pattern
   MSL = Mobile, Single tyre, Lug tread pattern
   MD = Mobile, Dual tyres, (highway tread pattern)

SHRP-IDEA Advisory Committee